Stony Brook University

Stony Brook University

Manipulating Wave Propagation Using Architected Metamaterials

A Dissertation Presented

by

Yanyu Chen

to

The Graduate School

in Partial Fulfillment of the

Requirements

for the Degree of

Doctor of Philosophy

in

Mechanical Engineering

Stony Brook University

May 2017

(include this copyright page only if you are selecting copyright through ProQuest, which is optional)

Stony Brook University

The Graduate School

Yanyu Chen

We, the dissertation committee for the above candidate for the

Doctor of Philosophy degree, hereby recommend

acceptance of this dissertation.

Lifeng Wang – Dissertation Advisor
Assistant Professor, Department of Mechanical Engineering

Toshio Nakamura – Chairperson of Defense
Professor, Department of Mechanical Engineering

Shikui Chen – Committee Member
Assistant Professor, Department of Mechanical Engineering

Jie Yu – Committee Member (outside)
Associate Professor, Department of Civil Engineering
Stony Brook University

This dissertation is accepted by the Graduate School

Charles Taber
Dean of the Graduate School

Abstract of the Dissertation

Manipulating Wave Propagation Using Architected Metamaterials

by

Yanyu Chen

Doctor of Philosophy

in

Mechanical Engineering

Stony Brook University

2017

Architected metamaterials with spatially modulated compositions have demonstrated great capabilities to manipulate mechanical wave propagation due to the existence of complete wave band gaps: frequency ranges where mechanical waves are suppressed. The research objective of this thesis is to control undesired vibration using architected metamaterials by integrative design, computational modeling, 3D printing, and mechanical testing.

The conflict between mechanical performance and wave energy dissipation limits the potential applications of the passive control technique. The first key objective of this thesis is to resolve this conflict using a system of 3D co-continuous architectures. These co-continuous composites exhibit enhanced mechanical properties including stiffness, strength, energy absorption, and fracture toughness, which are due to the mutual constraints between two phases of the co-continuous architectures. In addition, broad phononic band gaps were observed in this co-continuous metamaterial system, which is due to the overlapping of the Bragg scattering and local resonances.

In the complex noise and vibration environmental conditions, it is necessary to selectively control noise and vibration sources over a wide range of frequency. Here, 2D bioinspired architected composites were created by taking inspiration from the inherent architecture of nacreous materials. Broadband and multiple phononic band gaps were reported due to the coexisting of two different physical mechanisms, i.e., Bragg scattering and local resonances. Moreover, the geometric features of the bioinspired nacreous composites including structural hierarchy and heterogeneity were further exploited to achieve prominent vibration mitigation capabilities.

Besides excellent mechanical performance and vibration mitigation capability, lightweight is another criteria that limit the potential deployment of conventional materials. In this regard, lattice materials with different coordinate numbers are more efficient. Here, a group of hierarchical honeycombs was introduced. The introduction of a structural hierarchy into regular honeycombs gives rise to broad and multiple phononic band gaps. Importantly, an inversely proportional relation between relative density and band gap size was observed. As a result, lightweight yet stiff metamaterials can be designed for vibration mitigation. The rest of this thesis will focus on the mechanical tunability of vibration mitigation in a new group of stretchable lattice metamaterials. The proposed lattice metamaterials exhibit broadband vibration mitigation capability, which can be dynamically tuned by an external mechanical stimulus. Experimental studies were also conducted to validate the numerical simulations.

The findings presented here will open new avenues to control noise and vibration using architected metamaterial systems.

Table of Contents

List of Figures

Acknowledgments

First, I would like to express my deep gratitude towards my advisor, Professor Lifeng Wang, who gave me the freedom to pursue my own ideas. Without his continuous encouragements, I won't be able to complete this thesis timely. I also would like to thank my thesis committee members, Professor Toshio Nakamura, Professor Shikui Chen, and Professor Jie Yu, whose insightful comments were a tremendous help to improve this thesis.

I highly appreciate the graduate courses and lectures I attended at Stony Brook University, especially those instructed by Professor Toshio Nakamura, Professor Sam Huang, and Professor Ya Wang. The intellectual interactions with these brilliant minds have been one of the most fun and inspiring experiences I had in my graduate study at Stony Brook University.

I would also like to thank all my collaborators and whom I have not met so far: Professor Fabrizio Scarpa, Professor Lei Zuo, Professor Haimin Yao, Professor Jiahong Sun, Professor Katia Bertoldi, Tiantian Li, Dr. Pai Wang, Dr. Pu Zhang, Professor Vincent Laude, and Professor Zhengyou Liu. I have benefited substantially from the discussions and exchange of ideas with them.

My graduate study would not have been possible without the devoted love and understanding from my parents. I would like to give my special thanks to my wife Belle Zhou, whose unconditional love, deep care, and constant supports enabled me to finish my thesis.

CHAPTER 1. INTRODUCTION

1.1 Overview and objectives

Noise and vibration are prevalent in our daily life. They could arise from the use of tools and machine, construction, transportation, and aircraft (Figure 1.1). The undesired noise and vibration often harm human life and animal activities. In addition, the long-term and cycling vibration could cause crack and subsidence of surrounding buildings. It is well recognized that noise and vibration are not only an annoyance, but also have adverse health, social, and economic impacts. To avoid the undesired noise and vibration, a lot of basic technologies have been proposed in the past decades. In general, these technologies can be divided into two categories, i.e., active control and passive control. [1, 2] For active control, a second wave is specifically designed to interact with the vibration source, resulting in destructive interferences between these two waves and wave attenuation (Figure 1.2). [3, 4] This technology is particularly useful to control low-frequency noise and vibration but is unmanageable for high frequency due to the limitation of free space and zone of silence techniques. In this regard, passive control is more effective to control noise and vibration without the need for active control. [1, 5, 6] Soft materials based on wave energy dissipation or hard materials for wave reflection are often employed for passive control (Figure 1.3). It has been demonstrated that the both active and passive noise and vibration control methods are effective under certain circumstances; however, they still suffer from some drawbacks. For example, for active control, the frequency range is very limited, thereby limiting their potential applications in complex noise and vibrational environments. For passive control, there is a conflict between the wave energy dissipation and mechanical robustness. For example, soft materials

coated on the surface of submarines have the capability to control acoustic wave effectively, but the mechanical performance is very poor. This conflict is particularly prominent for noise and vibration control in mechanically challenging environments.

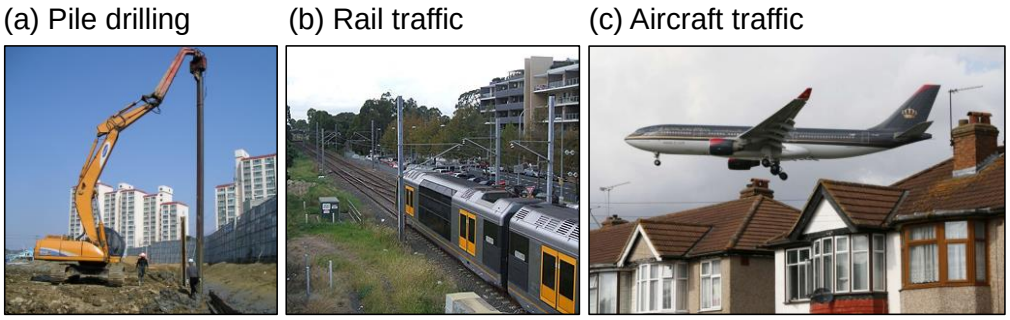

Figure 1.1 Possible vibration sources. (a) Pile drilling, (b) rail traffic, and (c) aircraft traffic. (Images source: https://www.thestar.com/news/world/2013/10/09)

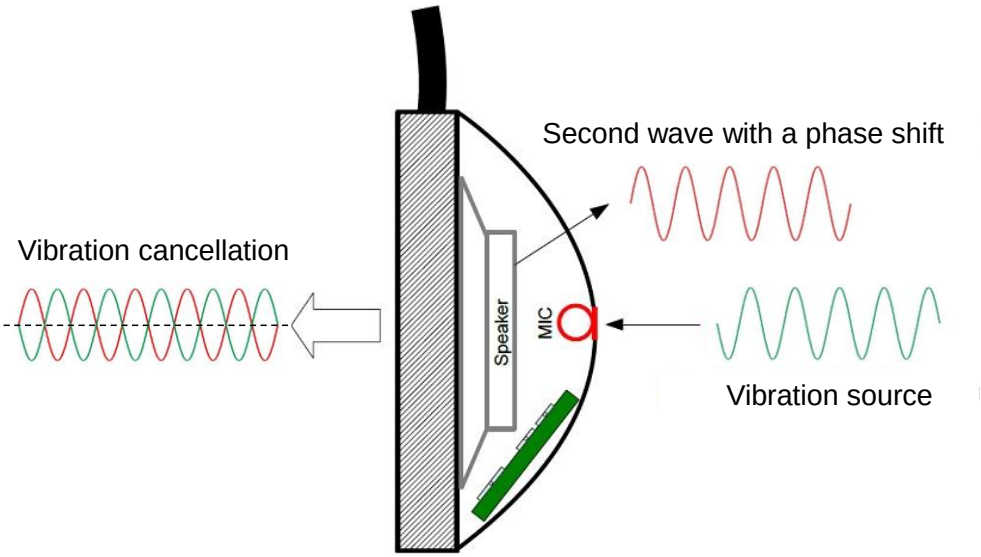

Figure 1.2 Schematic of active vibration control method.

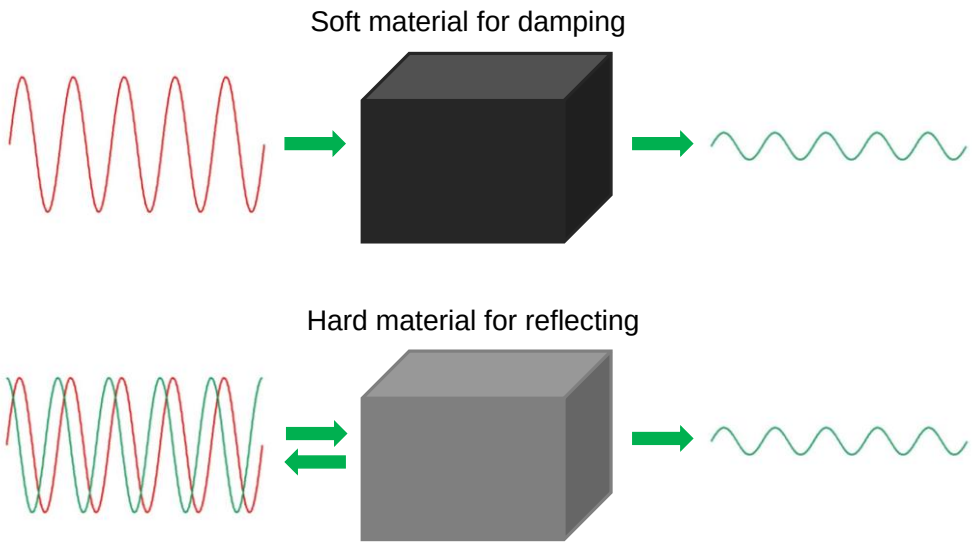

Figure 1.3 Schematic of passive vibration control.

Recently, architected materials with spatially modulated elastic constants and densities have been proposed to control noise and vibration. [7-10] When the wavelength of the propagating mechanical wave is comparable to the structural periodicity, destructive interferences arise at the interfaces of the compositions. As a result, the incident wave will be totally reflected and redirected to elsewhere. Despite remarkable achievement in this area has been obtained, challenges remains. For example, most of the previous studies are focused on exploring new physical mechanisms while little attention has been devoted to exploring the potential applications. Specifically, in engineering practice, broadband and multiband wave filtering capabilities are highly desired. In addition, improved mechanical performance including stiffness, strength, and fracture toughness are essential in structural components where load-carrying ability and vibration mitigation are simultaneously pursued. These pose a great challenge for the coupled architecture-material design strategy.

The research objective of this thesis is to control undesired vibration using architected metamaterials by integrative numerical and experimental approaches. Here architected metamaterials indicate that the effectiveness of noise and vibration control strongly depends on the designed architectures of the metamaterials, rather than their compositions. The objectives and approaches are shown in Figure 1.4. Specifically, the optimally architected metamaterials should have broadband and multiband wave filtering and waveguiding capabilities. In addition, the tunability of vibration mitigation capability using external mechanical stimuli will be explored. Importantly, excellent mechanical properties such as stiffness, strength, and fracture toughness will be considered in the metamaterial design. These research objectives will be accomplished by integrating metamaterial design, numerical modeling, 3D printing, and mechanical testing.

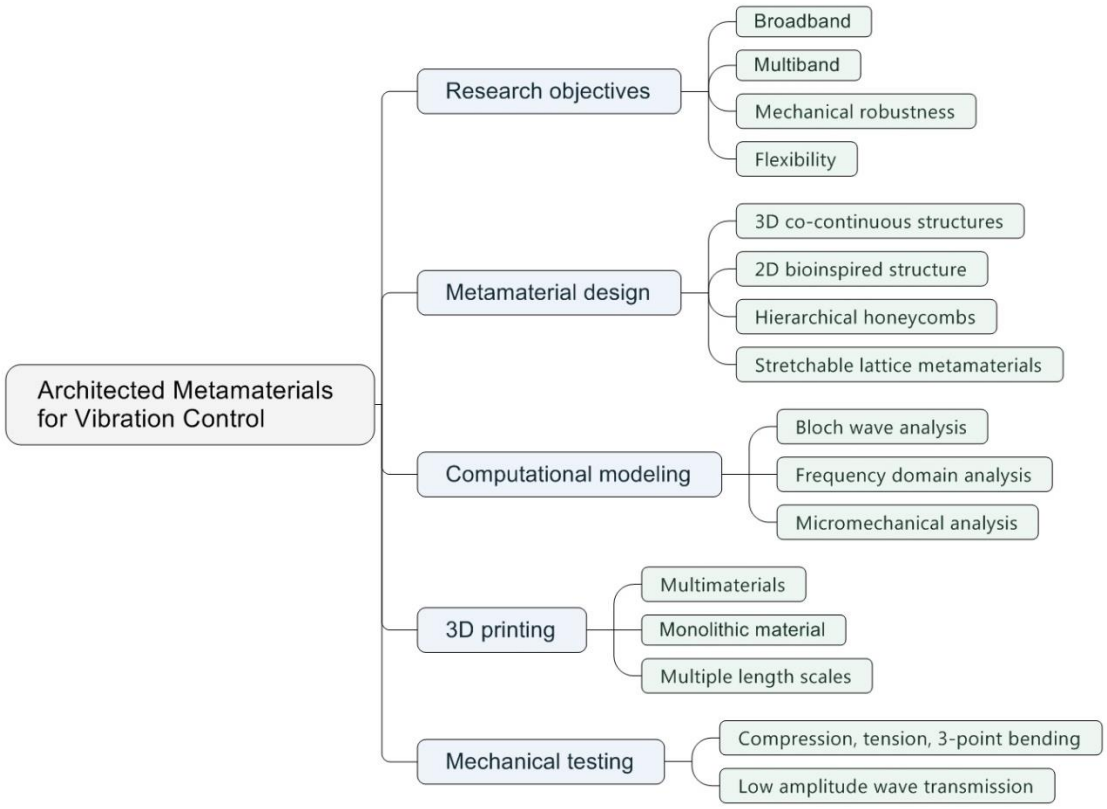

Figure 1.4 Flow chart of the specific objectives and approaches of this thesis.

1.2 Background and motivation

Historically, the study of wave propagation in architected materials can reach back to Rayleigh's treatment of wave propagations in his book The Theory of Sound. [11] After then, studies on wave propagation have evolved into an emerging multidisciplinary that encompasses physical mechanisms and applications from both condensed matter physics and acoustical engineering. Among these, periodic structures and materials with spatially modulated elastic constants and densities have attracted extensive research interests due to their capabilities to manipulate the propagation of sound and heat. [12-15] The introduction of structural periodicity leads to modification of phonon dispersion relations, providing avenues to tailor group velocities. One of the remarkable features in phonon dispersion relations is the existence of complete wave band gaps: frequency ranges where the propagation of phonons is suppressed irrespective of incident angles.

The technical word, phonon, coming from the study of vibrations of atomic crystal lattices, now has been widely adopted in studies on mechanical wave propagation. After the discovery of the first complete phononic band gap by Sigalas and Economou in 1993, [16] a new term, phononic crystal, was then coined by Kushwaha and his colleagues, differentiating it from its counterparts in electronics and optics, photonic crystals. [10] However, the first observation of noise and vibration attenuation using periodically architected materials was not reported until 1995 when a research group in Spanish studied the acoustic wave propagation in a sculpture. [17] They found that this sculpture enables the attenuation of sound waves in the audio frequency range. Intrinsically, the formation of the band gaps in phononic crystals is due to the destructive interferences of the propagating wave, which are intrinsically dedicated by the geometric

arrangements and material properties of the compositions. [18-21] In this regard, the complete band gaps are called Bragg-type band gaps.

The emergence of complete Bragg-type band gaps requires that the structural periodicity must be of the same magnitude as the effective wavelength in the periodic structures. This could pose a great challenge to design compact phononic crystals for audio frequency range since the size of the desired phononic crystals will be very large for low-frequency waves. In 2000, Liu and his colleagues developed a new type of periodic structure where low-frequency band gaps are observed. [22] This new structure was termed acoustic metamaterials. [18, 23, 24] Indeed, there is no clear boundary between these two types of mechanisms. As it will be shown in Chapter 2, there could be overlapping between these two kinds of band gaps. [25] As a result, the overlapping band gap is larger than conventional pure locally resonant band gaps. Now, the progress in the field of phononic crystals and acoustic metamaterials has since proliferated into a rich subject with numerous applications, including wave filtering, [26-28] acoustic cloaking, [29-31] heat management, [15, 32, 33] energy harvesting. [34-36]

Despite the extensive research interests and enticing potential applications, current phononic crystals and acoustic metamaterials still, suffer from some drawbacks. These limitations include 1) conflict between wave energy dissipation and mechanical performance. In mechanically challenging environmental conditions, the excellent mechanical performance of structures is a basic requirement and often essential. However, the mechanical properties are often conflicting with the demand for high dissipation of wave energy induced by vibrations and shocks. For example, the soft materials coated on the surface of submarine have excellent wave energy dissipation, but the mechanical performance is very poor. As a result, the soft coating materials need to be repaired and replaced frequently; 2) limited operation frequency range. Conventional

phononic crystals and acoustic metamaterials often operate in limited frequency ranges due to the narrow bandwidth of their band gaps. However, in engineering practice, broadband and multiple wave filtering and waveguiding are highly desired; 3) poor flexibility in practice. Conventionally, band gaps can be tuned by tailoring the inherent architectures and materials properties of compositions. However, once the designed structures are fabricated and installed in practice, it is impractical or spendy to tune the band gaps.

The proposed research is motivated by recent advances in architected mechanical metamaterials. It is well recognized that changing compositions and microstructures are common routines to change the material properties. However, recent studies have shown than tailoring the inherent architectures is a powerful tool to explore novel physical properties and functionalities, such as mechanical, optical, and phononic properties. A typical example is structural biological materials, which have been long served as a source of inspiration for developing high-performance composites. Indeed, many structural biological materials such as seashells, bone, and teeth have developed sophisticated architectures enabling an unusual combination of high stiffness, high strength, fracture toughness, and energy dissipation. [37-43] For example, nacre, the inner layer of a seashell, which is composed of 95 *vol*.% of hard mineral aragonite embedded within a soft organic matrix, exhibits a fracture toughness about three orders of magnitude higher than that of pure aragonite. [44] In addition, nacreous layer together with a prismatic layer in seashell has developed a multilayered protecting system to maintain their structural integrity under dynamic attack. [45] Notably, such a heterogeneous architecture enables a combination of enhanced stiffness and a surface hardness in the upper layer, with flexural modulus and fracture toughness in the inner layer. [46-48] Similar heterogeneous architectures have also been observed in human teeth, [49] consisting outer hard and brittle enamel layer and the relatively soft but tough dentin

layer, and fish scale armor, [50-53] which possess multiple mineralized layers where each layer is composed of a different nanocomposite material with varying structural and mechanical anisotropy. These natural design principles not only reveal the mechanisms responsible for the outstanding mechanical properties of structural biological composites but also provide us clues to design and develop architected mechanical metamaterials with simultaneous mechanical performance and vibration mitigation capability.

In addition to designing architected mechanical metamaterial by learning from nature, a lot of approaches have been proposed to achieve other novel physical properties, such as tunable phononic/photonic band gaps. Among these, introducing structural hierarchy into regular materials is a widely used approach. In fact, the structural hierarchy is prevalent in our daily life. The most famous hierarchical structure is Eiffel tower, which features lightweight and excellent mechanical performance. Other hierarchical examples range from nacreous biological materials and human bones with the multilevel structural hierarchy to synthesized hierarchically architected nano trusses with multiple length scales. [54-56] Recent studies show that it is possible to manipulate wave propagation by harnessing multiscale characteristic of hierarchical architectures. These rationally designed hierarchical architectures can give rise to multiple and broadband phononic band gaps as well as low-frequency band gaps. [27, 57, 58] The progress in these areas also motivates us to explore noise and vibration mitigation capability by rationally designing the architectures of conventional materials.

1.3 Outline of this thesis

In this thesis, it will be numerically and experimentally demonstrated that novel mechanical performance and vibration control capability can be simultaneously achieved using architected metamaterials.

In Chapter 2, we will briefly introduce four types of rationally designed architected metamaterials. Numerical methods of wave propagation in these architected metamaterials will be described. In addition, experimental studies using 3D printing in combination with mechanical testing will also be briefly introduced.

In Chapter 3, 3D co-continuous composites will be proposed to control noise and vibration. Complete elastic wave band gaps will be reported in the co-continuous periodic structures. Importantly, a new physical mechanism response for the elastic wave band gaps will be identified.

In Chapter 4, broad and multiple phononic band gaps will be demonstrated in 2D bio-inspired architected composites with a nacre-like microstructure. These prominent vibration control capabilities derive from the overlapping of local resonance and Bragg scattering. Moreover, we will show that the topological arrangement of the mineral platelets and changes of material properties can be utilized to tune the evolution of complete band gaps. Effects of structural hierarchy and heterogeneity in the bioinspired architected composites will be systematically investigated. For hierarchical composites with two levels of structural hierarchy, multiple band gaps, and passbands, covering an ultrawide frequency range, will arise. The interplay between the multilevel structural hierarchy and the multiband characteristic will be discussed. We will also numerically demonstrate that broadband wave attenuation zones can be achieved by tailoring the

geometric features of the heterogeneous architecture. Physical mechanisms and geometric features accounting for these vibration mitigation capabilities will be identified.

In Chapter 5, it will be demonstrated that hierarchically architected honeycombs can be exploited to achieve prominent wave attenuation and load-carrying capabilities. The hierarchically architected honeycombs exhibit broad and multiple phononic band gaps. The mechanisms responsible for these band gaps depend on the geometric features of the hierarchical honeycombs rather than their compositions. Furthermore, the mechanical performance of the hierarchical honeycombs will be numerically evaluated.

In Chapter 6 and 7, a class of stretchable lattice metamaterials with mechanically tunable negative Poisson's ratios and vibration mitigation capability will be presented. The proposed architected lattice materials are built by replacing regular straight beams with sinusoidally shaped ones, which are highly stretchable under uniaxial tension. Numerical and experimental results indicate that the proposed lattice metamaterials exhibit Poisson's ratios varying between -0.7 and 0.5 over large tensile deformations up to 50%. This large variation of Poisson's ratio values is attributed to the deformation pattern switching from bending to stretch within the sinusoidal beams. It will also be shown that broadband and multiple band gaps in these lattice metamaterials can be dynamically tuned by an external mechanical stimulus.

Finally, main contributions, broad impacts, and future work will be briefly illustrated in Chapter 8.

CHAPTER 2. MATERIALS AND METHODS

2.1 Periodic structures and wave propagation

A periodic structure is defined as an assembly of objects that repeat regularly in space. Depending on its repeating directions, we have one-dimensional (1D), two-dimensional (2D), and three-dimensional (3D) periodic structures. To demonstrate the periodic feature of the periodic structure, we will use a two-dimensional periodic structure as an example. Figure 2.1 (a) shows a 2D periodic structure, which extends infinitely in the 2D plane. The representative repeating object can be obtained by drawing two sets of equally spaced parallel lines, as shown in Figure 2.1 (b). The divided objects are exactly same in terms of their size and shape. As a result, the 2D periodic structure can be considered as the assembly of these objects that are arranged regularly in space.

To more clearly characterize the feature of the periodic structure, each repeated object can be imaged a virtual point (Figure 2.1 (c)). As a result, we will have a corresponding array of periodic points, which is called a point lattice of the 2D periodic structure (Figure 2.1 (d)). It is noticeable that the point lattice is equivalent to the repeated objects. We can use the two lattice vectors ($\mathbf{a_1}$, $\mathbf{a_2}$) along with a lattice angle (γ) to uniquely define the periodic structure:

$$\mathbf{R} = n_1\mathbf{a_1} + n_2\mathbf{a}_2 \tag{2.1}$$

where n_1 and n_2 are arbitrary integer numbers. Depending on the structural periodicity, there are five types of two-dimensional point lattices, i.e., oblique, rectangular, square, triangular, and rhombus. A similar procedure can be applied to 1D and 3D periodic structures.

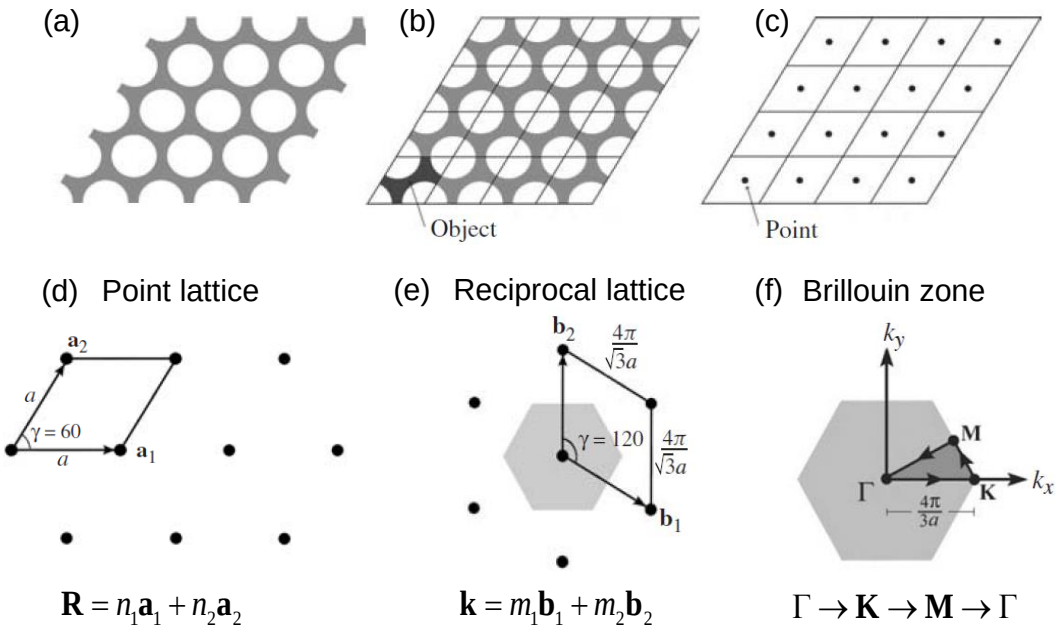

Figure 2.1 Schematic of a two-dimensional periodic structure. (a)-(c) Two-dimensional periodic structure, (d) point lattice, (e) reciprocal lattice, and (f) the first irreducible Brillouin zone. (Images are taken from Maldovan, M. and Thomas, E.L. John Wiley & Sons, 2009.)

To study wave propagation in periodic structures, it is necessary to find the relation between wave vectors and their corresponding eigenfrequencies, which is called a phononic dispersion relation. The most fundamental property of phononic dispersion relation is the existence of complete wave band gaps: frequency range where wave propagation is suppressed. To do this, we need to find the wave vectors associated with the periodic structure that can completely describe the wave propagation. When the plane wave propagating in periodic structures, there are certain wave vectors that satisfying the periodicity of the point lattice. [59] As a result, we have

$$e^{i\mathbf{k}\cdot\mathbf{r}} = e^{i\mathbf{k}\cdot(\mathbf{r}+\mathbf{R})} \tag{2.2}$$

By combining Eq. (2.2) with Eq. (2.1), we can calculate the wave vector, **k**, as shown in Figure 2.1 (e). By connecting the midpoints of the reciprocal lattices, we have a gray hexagonal area, which is called Brillouin zone (Figure 2.1 (f)). In view of the symmetry of this Brillouin zone, only 1/12 of the gray region needs to be considered. That means, to study wave propagation in the 2D periodic structure, we only need to study the wave propagation along the path shown in the first irreducible Brillouin zone. Next, we will show how to numerically calculate the phononic dispersion relation and wave transmission in periodic structures.

2.2 Numerical modeling of wave propagation in architected metamaterials

2.2.1 Bloch wave analysis for infinite periodic structures

All the proposed architected metamaterials in this thesis are spatially periodic and infinite. To evaluate the wave propagation in these periodic metamaterials, only one unit cell need to be considered by imposing periodic boundary conditions according to the Bloch theory. Bloch wave analysis for infinite periodic structures will be briefly shown as follows.

2.2.1.1 Construction of the first irreducible Brillouin zone

To evaluate the vibration mitigation capability of the periodic structures or the existence of complete wave band gaps, the phononic dispersion relation, i.e., the relation between wave vector and eigenfrequency, needs to be constructed. To this end, we first need to find the set of wave vectors that can completely describe the propagation of mechanical waves in periodic structures. This set of wave vectors is called the Brillouin zone. For example, the Brillouin zones can be defined as shown below for the 3D periodic structures with different lattice symmetries.

Consider an arbitrary Bravais lattice that described by the primitive vectors $\mathbf{a_1}$, $\mathbf{a_2}$, and $\mathbf{a_3}$. The associated reciprocal lattice wave vectors **G** is given by

$$\mathbf{G} = m_1\mathbf{b_1} + m_2\mathbf{b_2} + m_3\mathbf{b_3} \tag{2.3}$$

where m_1, m_2, and m_3 are arbitrary integer numbers and $\mathbf{b_1}$, $\mathbf{b_2}$, and $\mathbf{b_3}$ are reciprocal lattice wave vectors, which can be calculated as

$$\mathbf{b_1} = 2\pi \frac{\mathbf{a_2} \times \mathbf{a_3}}{\mathbf{a_1} \cdot (\mathbf{a_2} \times \mathbf{a_3})}$$

$$\mathbf{b_2} = 2\pi \frac{\mathbf{a_3} \times \mathbf{a_1}}{\mathbf{a_1} \cdot (\mathbf{a_2} \times \mathbf{a_3})} \tag{2.4}$$

$$\mathbf{b_3} = 2\pi \frac{\mathbf{a_1} \times \mathbf{a_2}}{\mathbf{a_1} \cdot (\mathbf{a_2} \times \mathbf{a_3})}$$

Then the Brillouin zones can be obtained by bounding the planes half was between adjacent reciprocal lattice points. The 3D first irreducible Brillouin zones for SC, BCC, and FCC metamaterials are shown in Figure 2.2.

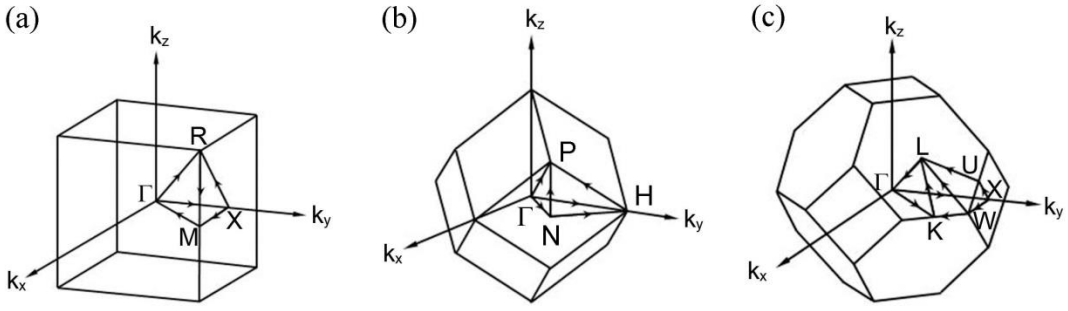

Figure 2.2 The first irreducible Brillion zones for different co-continuous composites with different lattice symmetries. (a) –(c): The irreducible Brillouin zones for the SC, BCC, and FCC

Bravais lattices, respectively. For SC lattice, the wave vectors are

$\Gamma=(0,0,0)$, $\mathbf{X}=\frac{\pi}{a}(0,1,0)$, $\mathbf{M}=\frac{\pi}{a}(1,1,0)$, $\mathbf{R}=\frac{\pi}{a}(1,1,1)$; for BCC lattice, the wave vectors are

$\Gamma=(0,0,0)$, $\mathbf{N}=\frac{\pi}{a}(1,1,0)$, $\mathbf{P}=\frac{\pi}{a}(1,1,1)$, $\mathbf{H}=\frac{\pi}{a}(0,2,0)$; for FCC and Octet lattices, the wave vectors are

$\Gamma=(0,0,0)$, $\mathbf{X}=\frac{\pi}{a}(0,2,0)$, $\mathbf{U}=\frac{\pi}{a}\left(\frac{1}{2},2,\frac{1}{2}\right)$, $\mathbf{L}=\frac{\pi}{a}(1,1,1)$, $\mathbf{W}=\frac{\pi}{a}(1,2,0)$, $\mathbf{K}=\frac{\pi}{a}\left(\frac{3}{2},\frac{3}{2},0\right)$.

2.2.1.2 Governing equation and numerical implementation

The governing equation of elastic wave propagating in the 3D periodic structures is given by: [60]

$$-\rho\omega^2\mathbf{u}=\frac{E}{2(1+\nu)}\nabla^2\mathbf{u}+\frac{E}{2(1+\nu)(1-2\nu)}\nabla(\nabla\cdot\mathbf{u}) \tag{2.5}$$

In Eq. (2.5) **u** is the displacement vector and ω is the angular frequency. E, ν, and ρ are Young's modulus, the Poisson's ratio, and the density of each constituent material, respectively.

The phononic dispersion relations are constructed by performing eigenfrequency analysis. The Bloch's periodic boundary conditions are applied at the boundaries of the unit cell such that: [61]

$$\mathbf{u}_i(\mathbf{r}+\mathbf{a})=\mathbf{u}_i(\mathbf{r})\exp(i\mathbf{k}\cdot\mathbf{a}) \tag{2.6}$$

where **r** is the location vector, **a** is the lattice translation vector, and **k** is the wave vector.

In finite element implementation, Eq. (2.6) is decomposed into two parts, i.e., the real part and imaginary part, which are given by

$$\mathbf{u}_i^{re}(\mathbf{r}+\mathbf{a})=\mathbf{u}_i^{re}(\mathbf{r})\cos(\mathbf{k}\cdot\mathbf{a})-\mathbf{u}_i^{im}(\mathbf{r})\sin(\mathbf{k}\cdot\mathbf{a}) \tag{2.7}$$

$$\mathbf{u}_i^{im}(\mathbf{r}+\mathbf{a})=\mathbf{u}_i^{re}(\mathbf{r})\sin(\mathbf{k}\cdot\mathbf{a})+\mathbf{u}_i^{im}(\mathbf{r})\cos(\mathbf{k}\cdot\mathbf{a}) \tag{2.8}$$

Now the governing equation Eq. (2.5) combined with the boundary condition Eq. (2.7) and Eq. (2.8) leads to the standard eigenvalue problem:

$$\left(\mathbf{K}-\omega^2\mathbf{M}\right)\mathbf{U}=0 \tag{2.9}$$

where **U** is the assembled displacement vector, and **K** and **M** are the global stiffness and mass matrices assembled using standard finite element analysis procedure. The unit cell is discretized using 10-node tetrahedral elements. In our simulations, we have used a discretization of 40 elements for the minimum wavelength. Eq. (2.9) is then numerically solved by imposing the two components of the wave vectors and hence calculates the corresponding eigenfrequencies. The phonon dispersion relations are obtained by scanning the wave vectors in the first irreducible Brillouin zones.

2.2.2 Frequency domain analysis for finite-size structures

For engineering practice in noise and vibration control, only finite-size structures can be used. Therefore, it is necessary to evaluate the vibration mitigation capability in finite-size structures. In this case, frequency domain analysis is needed. For example, to model the elastic wave incident normally to the surface of co-continuous metamaterials, a harmonic vertical displacement with a small amplitude is applied on the left surface (Figure 2.3). Perfectly matched layers (PMLs) are applied at the two ends of the homogeneous parts to prevent reflections by the scattering waves from the domain boundaries. [24, 62]

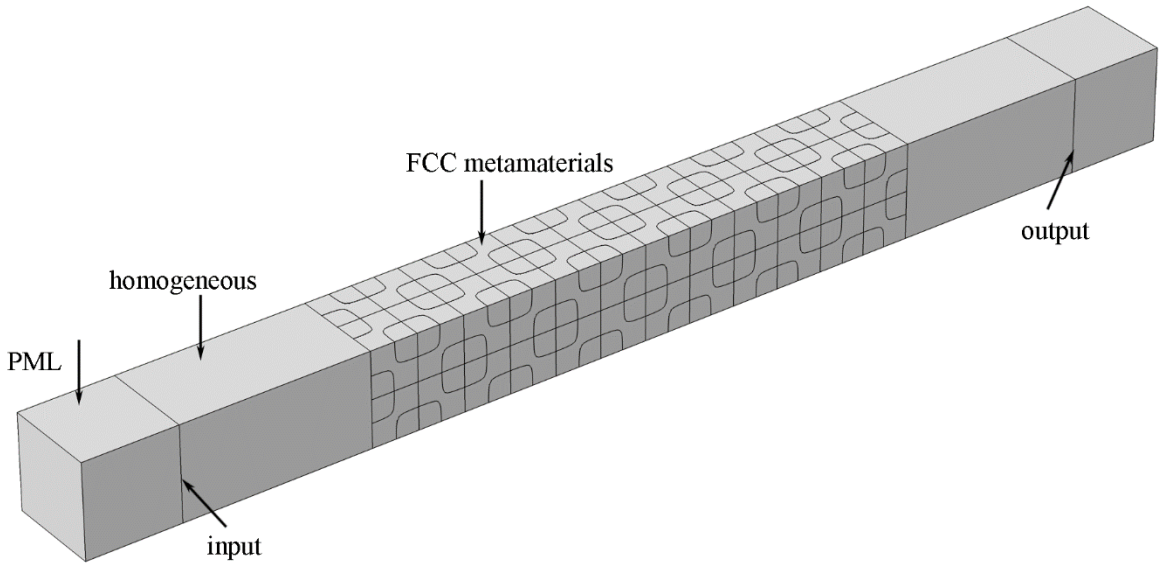

Figure 2.3 FE model of FCC co-continuous metamaterial for frequency domain analysis.

The size of the elements in each FE model depends on the frequency range of incident wave. Here we have used a discretization 40 elements for the minimum wavelength. The transmission coefficient is defined as

$$\phi = 20\log_{10}\left[\left(\bar{u}+\bar{v}+\bar{w}\right)/\left(u_0+v_0+w_0\right)\right] \tag{2.10}$$

where $\bar{u}$, $\bar{v}$, and $\bar{w}$ are the amplitudes of averaged displacement components collected on the right surface, respectively; u_0 , v_0 , and w_0 are the amplitudes of the applied displacement components, respectively.

2.3 Design and 3D printing of architected metamaterials

It is a common practice that tailoring architecture is a powerful routine to achieve new properties and functionalities. For example, with the evolution of time, the wheels have been improved from initial solid stone to cellular structures with well-defined topologies. With newly architectural design, these modern wheels are highly structural efficient. Typical properties including

lightweight, more uniform strain energy distribution, and higher specific mechanical properties. This motives us to design architected metamaterials to explore novel properties and functionalities.

Here four types of architected metamaterials will be designed: 1) *Co-continuous composites*. As mentioned before, the mechanical performance of soft materials is very poor for passive vibration control method. Here we proposed a system of co-continuous composites, aiming at achieving simultaneous improved mechanical performance and vibration control capability (Figure 2.4 (a)). 2) *2D bio-inspired architected composites*. As will be shown in Chapter 3, co-continuous composites exhibit a single complete wave band gap. While under certain circumstances, broadband and multiband vibration control capabilities are highly desired. Inspired by the observation that many structural biological materials exhibit improved mechanical performance under both static and dynamic loading conditions, we will focus on a typical biological material, nacre, where a brick-and-mortar-like microstructure has been observed (Figure 2.4 (b)). 3) *Hierarchical honeycombs*. The first two architected metamaterials are composite materials, where the coupled architecture-material design is a great challenge. In addition, in applications including aerospace and race shells, lightweight design are highly essential. In this regard, lattice materials have great potential applications. Here a group of hierarchical honeycombs with different node connectivity will be created (Figure 2.4 (c)). 4) *Stretchable lattice metamaterials*. Wave propagation properties can be tuned by tailoring the geometric features of the architected metamaterials. However, it is impractical to change the geometric features in practice when a given design is implemented. Here we hope to dynamically tune the wave propagation using external stimuli. Aiming at harness buckled mode of regular beams, we proposed a system of lattice metamaterials with high stretchability and tunable vibration control capability (Figure 2.4 (d)).

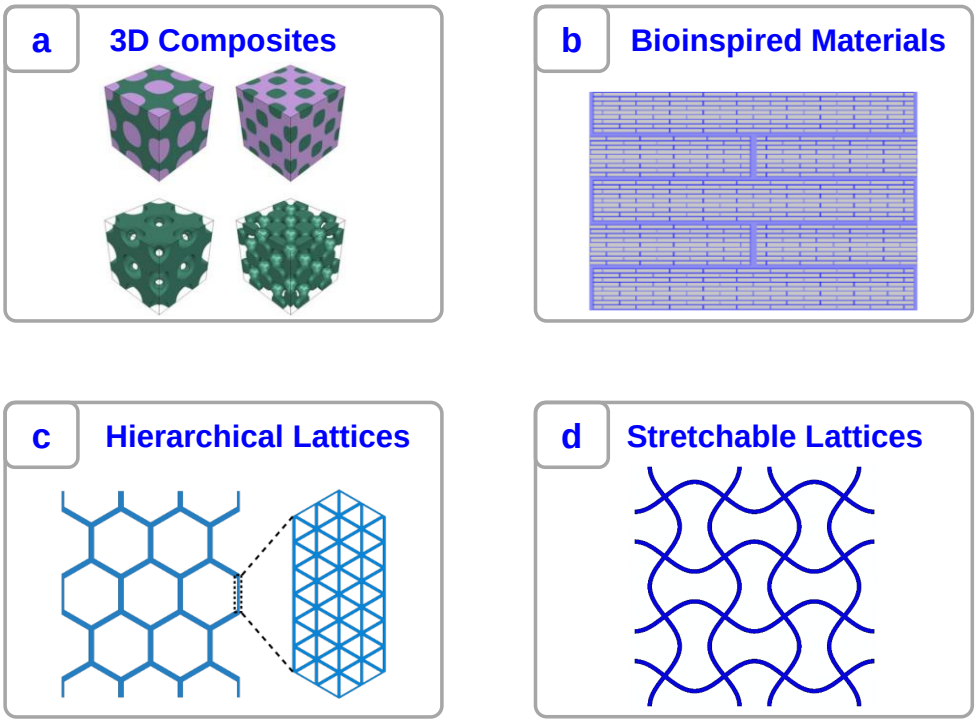

Figure 2.4 Four types of architected metamaterials for vibration control. (a) 3D co-continuous composites, (b) 2D bioinspired architected composites, (c) hierarchical honeycombs, and (d) stretchable lattice metamaterials.

All specimens including dogbone and architected metamaterials used in the study have been printed by using an Objet Connex260 multi-material 3D printer (Stratasys) (Figure 2.5). Tango plus and verowhite will be used as the constitutive materials for the samples. The chemistry of these materials is proprietary to Stratasys. The dimensions of the dogbone specimen comply with the ones prescribed by the ASTM D412 standard. Within the limitation of 3D printing technology, the layer orientation was found to influence the mechanical properties of the material; therefore, all the specimens were printed along the same orientation on the printer build platform. The as-fabricated specimens were kept at room temperature for 7 days to allow for the saturation of the curing. The detailed dimensions and topologies for 3D printed can be found in each chapter.

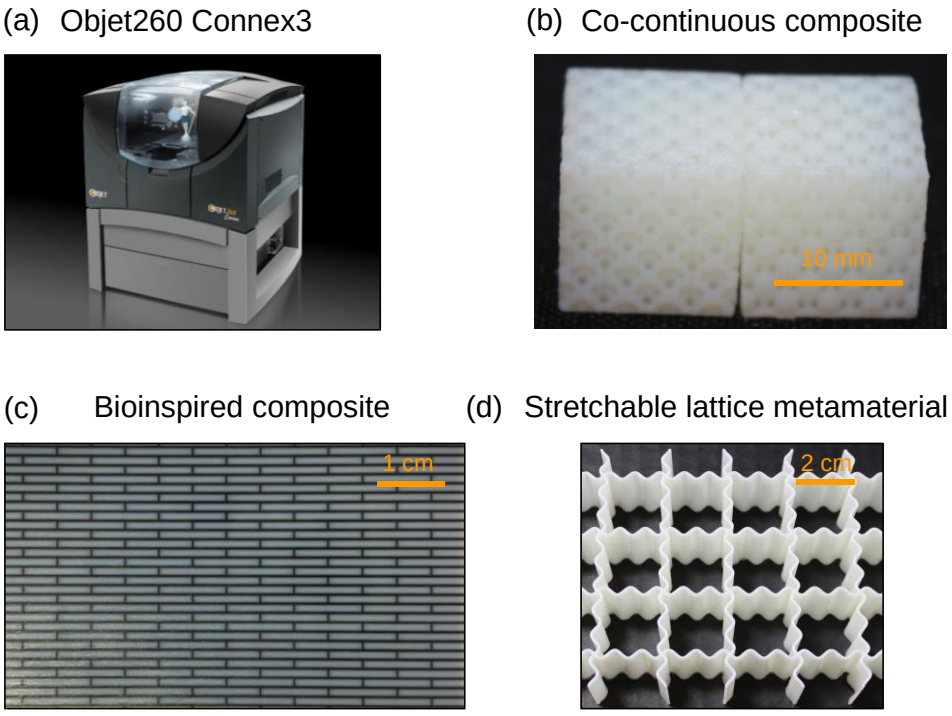

Figure 2.5 3D printer and 3D printed architected metamaterials. (a) Objet260 Connex3 3D printer, (b) 3D printed co-continuous composite, (c) 3D printed bioinspired composite, and (d) 3D printed stretchable lattice metamaterials.

2.4 Mechanical testing

To evaluate the mechanical properties of the architected metamaterials, uniaxial tensile testing will be performed using a MTS mechanical tester (C43) with a 10 kN load cell. All experiments were conducted in a quasi-static regime with a constant strain rate of 0.001 s^{-1}. The load-displacement curves measured from the uniaxial tensile tests were then transferred into nominal stress- strain behaviors based on the measured dimensions of the specimens. Images of the specimens at various loading conditions were taken at a rate of 1 FPS (VicSnap, Correlated Solution). For the dogbone specimen, speckles were sprayed on the samples using a spray paint for digital image correlation (DIC) measurements. The deformation and local strain contours of the samples were tracked by

using DIC (Vic-2D, Correlated Solution) to calibrate the nominal stress- strain curves and to obtain the Poisson's ratio of the constitutive material.

Low amplitude wave transmission tests were performed on the 3D-printed samples to validate the simulated phononic band gaps. The sample was supported by two specially designed holders to avoid the friction damping effect from the testing table (Figure 2.6). An ICP® Impact Hammer with a hard tip (Model 086E80) was used to provide impulse forces exerted at the input end of the samples. The hammer can generate an impulse force with the frequency range up to 30 kHz that is sufficient to cover the frequency range of interest. A piezoelectric accelerometer was attached at the receiving end of the sample to capture the response signal transmitted from the input excitation. A Coco 80 data collector was adopted to record both the input force and output acceleration.

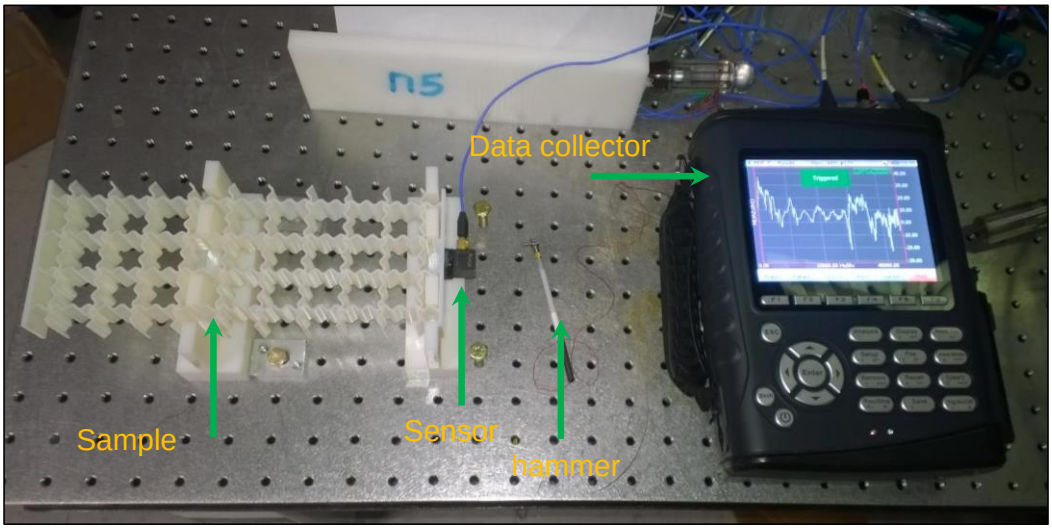

Figure 2.6 Experimental setup of low amplitude wave transmission test.

CHAPTER 3. 3D CO-CONTINUOUS COMPOSITES FOR VIBRATION CONTROL

3.1 Introduction

In recent years, the metamaterial concept has been extended to exploit unusual mechanical properties, such as negative Poisson's ratio, [63, 64] ultra-lightweight and stiffness, [65-68] high energy absorption, [69-71] negative bulk modulus, and negative mass density. [72-76] One particular class of mechanical metamaterials, locally resonant acoustic metamaterials, has attracted much interest because they exhibit lower frequency band gaps as compared to the Bragg band gaps in conventional phononic crystals. [22, 77, 78] The band gaps in these acoustic metamaterials stem from local resonances associated with substructures, leading to narrow acoustic band gaps. These acoustic metamaterials offer promising applications such as wave filtering, [22, 77, 78] acoustic cloaking, [79] and energy harvesting. [35, 36] However, the substructures with local resonant units may lead to poor mechanical performance. [80, 81]

Mechanical properties such as high stiffness, high strength are essential in most structural components, yet they are often conflicting with the demand for high dissipation of wave energy induced by vibrations and shocks. Little attention, however, has been paid to the trade-off between the mechanical properties and wave filtering capability of acoustic metamaterials. This, in turn, may limit the potential employment of the metamaterials under harsh environments and extreme loading conditions. In this Chapter, a group of co-continuous acoustic metamaterials will be introduced, where mechanical properties and wave energy dissipation are provided by different constituent phases. In a two-phase co-continuous composite, each constituent phase completely interpenetrates through the composite microstructure in all three dimensions and contributes its

own properties in a quite independent manner to the overall properties of the composite, while these two phases are topologically interconnected and mutually reinforced in the three dimensions. [71, 82] This synergistic mechanism has been numerically and experimentally demonstrated in a group of periodic polymer co-continuous composites, which enable enhanced mechanical performance achieving a unique combination of stiffness, strength, and energy absorption compared with other conventional composites. [69-71]

The model system of co-continuous metamaterials investigated here is based on level set structures possessing interfaces close to those of triply periodic minimal surfaces, and an octet-truss lattice structure (see Figure. 3.1). These level set structures have been shown to exhibit enhanced elastic properties compared with their rod-connected model counterparts. [83] While the octet-truss lattice structure is a typical stretching-dominated structure with a very high strength-to-weight ratio. It has been shown that the octet-truss lattice material can be considered as a promising alternative to metallic foams in lightweight structures. [83, 84] These rationally designed periodic structures with proper combinations of constituent materials could help guide the creation of mechanically robust acoustic metamaterials.

In this Chapter, the existence of complete band gaps in four types of metamaterials will be demonstrated through numerical simulations. The mechanisms of the band gaps formation in the co-continuous metamaterials are discussed. Furthermore, frequency tunability of the band gaps is achieved by tailoring the topological arrangements of the co-continuous metamaterials.

3.2 Model description

Figure 3.1 displays the triply periodic co-continuous metamaterials with simple cubic (SC), body-centered cubic (BCC), face-centered cubic (FCC) and octet-truss lattices, where the volume

fraction (V_f) of each phase is approximately 50%. The interfaces of SC, BCC, and FCC co-continuous metamaterials are defined by a function of form F: $\mathbf{R}^3 \rightarrow \mathbf{R}$ that satisfies the equation $f(x, y, z) = t$, where $t \in \mathbf{R}$ is a constant and $(x, y, z) \in \mathbf{R}^3$ are the coordinates of a point on the level surface,

$$\begin{aligned} f_{\mathrm{SC}}(x,y,z) &= \cos(x)+\cos(y)+\cos(z)-0.5\cos(x)\cos(y)-0.5\cos(y)\cos(z)-0.5\cos(z)\cos(x)+t, \\ f_{\mathrm{BCC}}(x,y,z) &= \cos(x)\cos(y)+\cos(y)\cos(z)+\cos(z)\cos(x)+t, \\ f_{\mathrm{FCC}}(x,y,z) &= 4\cos(x)\cos(y)\cos(z)+\cos(2x)\cos(2y)+\cos(2y)\cos(2z)+\cos(2z)\cos(2x)+t, \end{aligned} \tag{3.1}$$

where t is a constant that determines the volume fraction of the solid phase. As a result, the symmetry and volume distribution in these structures can be precisely controlled.

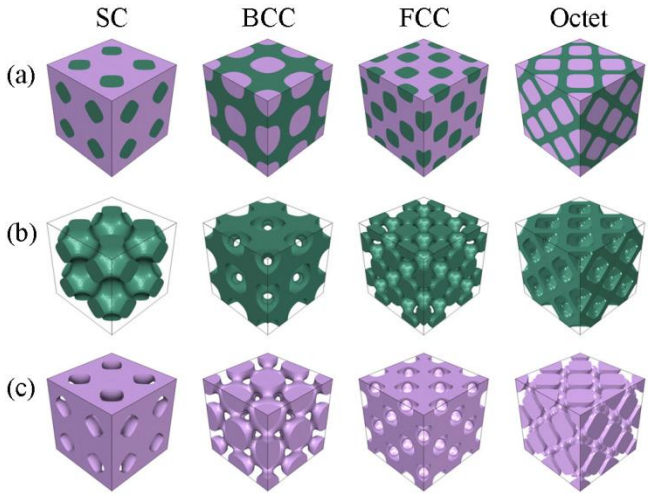

Figure 3.1 Schematics of the proposed 3D co-continuous composites. (a) Triply periodic co-continuous acoustic metamaterials consisting of 2×2×2 unit cells with simple cubic lattice, body-centered cubic lattice, face-centered cubic lattice, and octet-truss lattice. (b) The corresponding phase *A* in these metamaterials. (c) The corresponding phase B in these metamaterials.

The lattice constants along three directions are all set to 2 mm. The constituent phase *A* and phase *B* in each metamaterial are chosen to be a ceramic (Boron Carbide, B_4C, a hard ceramic

material) and a glassy polymer (SU-8, a commonly used epoxy). The material properties are characterized by Young's modulus E_A= 460 GPa, Poisson's ratio υ_A= 0.17 and density ρ_A= 2500 kg/m^3 for B_4C; the ones for SU-8 are E_B= 3.3 GPa, Poisson's ratio υ_B= 0.33 and density ρ_B= 1180 kg/m^3. The mechanical stiffness and strength of these co-continuous metamaterials are well retained due to the mutual constraints in the interpenetrating phases. [69-71]

3.3 Results and discussion

3.3.1 Phononic dispersion relations

The simulated phononic dispersion relations of the ceramic/polymer co-continuous metamaterials with SC (V_f =59%), BCC (V_f =59%), FCC (V_f =62%), and octet-truss lattices (V_f =49%) are shown in Figure 3.2. At the given volume fraction, complete band gaps arise in the dispersion relations of the co-continuous metamaterials. To be specific, the widths of complete band gaps in the four types of metamaterials are 0.008 MHz, 0.054 MHz, 0.069 MHz, and 0.075 MHz, respectively. At the approximate volume fraction of 60%, the metamaterials with BCC and FCC lattices possess larger complete band gaps as compared to the metamaterial with SC lattice. Notably, the largest width of the complete band gap is achieved in the metamaterial with octet-truss lattice at a lower volume fraction, indicating that the metamaterials with octet-truss lattice hold potential in the future design of lightweight acoustic metamaterials. It also should be noted that the frequency ranges of the complete band gaps reported here are much higher than those of other locally resonant metamaterials. [22, 78] This is because the relatively soft phase in the co-continuous metamaterials is much stiffer than a silicon rubber that is widely used as the soft phase in locally resonant metamaterials**.**

The most remarkable feature in the phononic dispersion relations discussed above is the existence of flat bands across the edges of Brillouin zones, which is a strong evidence of local resonances arising in these four types of co-continuous metamaterials. [22, 78] To examine the origin of these flat bands, we plot the eigenmodes on both the lower and upper edges of the band gaps, as shown in Figure 3.2. Clearly, the displacements are almost localized in the relatively soft phase, indicating that the complete band gaps in the four types of co-continuous metamaterials are caused by local resonances. However, previous studies have shown that complete band gaps resulting from local resonances and Bragg scattering can coexist in periodic composites. [85, 86] To further reveal the mechanisms of complete band gaps formation, we compare the wavelength at the midgap frequency with the lattice constant of the metamaterial with FCC lattice, as an example. The wavelength at midgap frequency is given by $\lambda = c_t / \varpi$, where λ is the wavelength, c_t is the transverse velocity in the metamaterial, and ϖ is the midgap frequency. The transverse velocity in the metamaterial is given by $c_t = \sqrt{\mu^* / \rho^*}$, where μ^* and ρ^* are the effective shear modulus and effective density of the metamaterial, respectively. As a rough estimation, using the effective shear modulus (81.6 GPa) of the metamaterial calculated from FEM, we have obtained the estimated wavelength $\lambda = 5$ mm, half of which is the same magnitude as the lattice constant 2.0 mm. This comparison indicates that Bragg scattering also contributes to the complete band gap formation. In other words, the frequency ranges of Bragg band gaps have the same order of magnitude as those of locally resonant band gaps. Therefore, the simulated complete band gaps originate from the overlap between locally resonant band gap and Bragg band gap.

It should be pointed out that the overlapping complete band gaps reported here are different from those achieved by manipulating the periodicity of substructures in the composite media. [87]

The coupling effects of local resonances and Bragg scattering in this work are intrinsically governed by the topological arrangements of the co-continuous structures and the mechanical properties of the constituent phases, and hence independent of lattice constants. However, the scalability of the periodic structure is still applied and can be used to achieve lower band gap frequencies as desired. Relatively soft materials (but keeping high mechanical impedance ratio between two phases) can be chosen to further lower the band gap frequency.

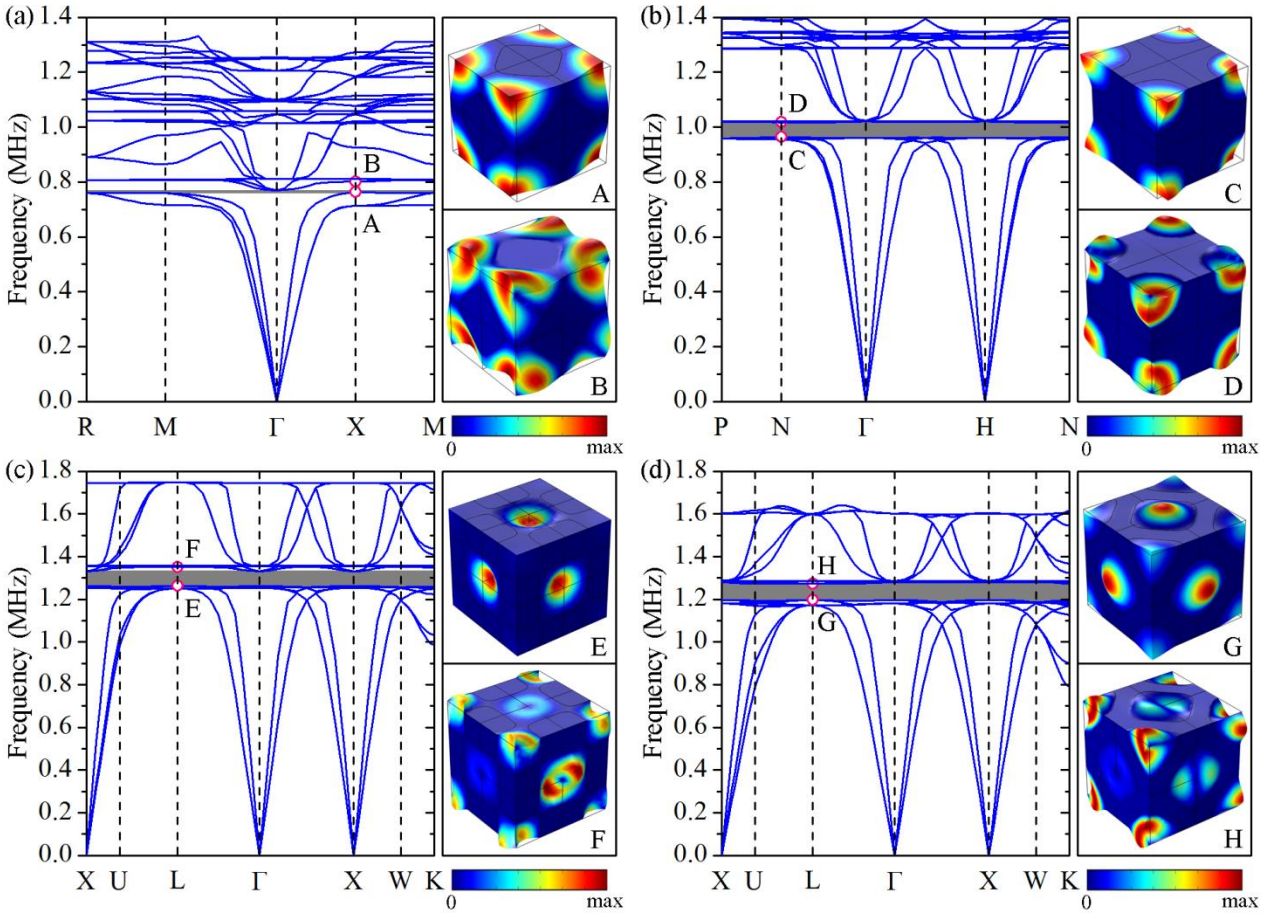

Figure 3.2 Phononic dispersion relations and the corresponding eigenmodes of the ceramic/polymer co-continuous metamaterials. (a) SC (V_f =59%), (b) BCC (V_f =59%), (c) FCC (V_f =62%), and (d) octet-truss (V_f =49%) lattices.

3.3.2 Dynamic response of finite-size structure

Additional insight into the origin of the band gaps can be gained by observing the response of the metamaterials under incident waves with different frequencies. To this end, we investigate elastic wave propagation along ΓX/ΓH direction in the co-continuous metamaterials with finite unit cells. As shown in Figure 3.3 (a)-(d), strong attenuation zone in the transmission spectrum of each co-continuous metamaterial is observed, which agrees well with the partial band gap in the corresponding band structures in Figure 3.2. For simplicity, taking the co-continuous metamaterial with FCC lattice as an example, we present the response of this metamaterial under the excitation frequencies below, within and above the band gap along ΓX direction, respectively (Figure 3.4 (a)-(c)). As expected, when the frequency of the incident wave lies below and above the band gaps, i.e., 0.85 MHz and 1.36 MHz, the incident elastic wave partially passes through and is partially reflected by the co-continuous metamaterial. In contrast, the incident elastic wave with a frequency within the band gap (1.28 MHz) is localized at x=7 mm and its amplitude is amplified to 12.9, indicating that local resonances arise in the soft phase. The incident wave, however, attenuates rapidly after propagating for a distance of 4 mm. This phenomenon is attributed to Bragg scattering arising in the co-continuous metamaterial. The responses of the metamaterial experiencing different incident waves further support our claim that the complete band gaps result from the coupling effects of local resonances and Bragg scattering. Similar behaviors hold for other types of co-continuous metamaterials.

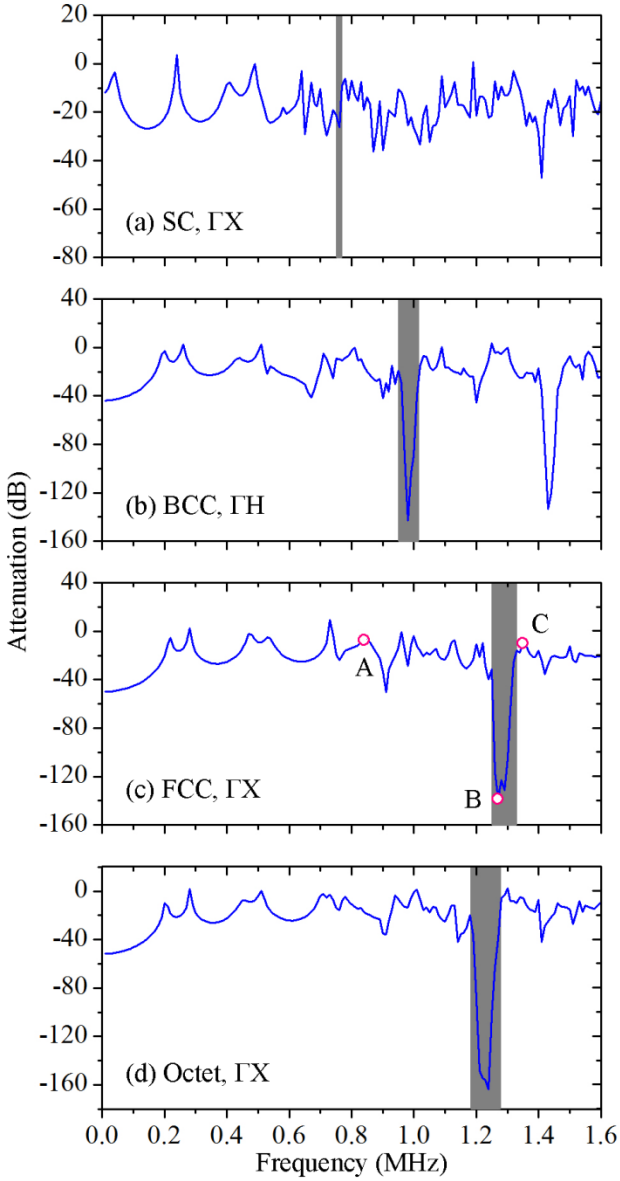

Figure 3.3 Transmission spectra of the ceramic/polymer co-continuous metamaterials. (a) SC (V_f=59%), (b) BCC (V_f=59%), (c) FCC (V_f=62%), and (d) octet-truss lattices (V_f=49%) along ΓX/ΓH direction.

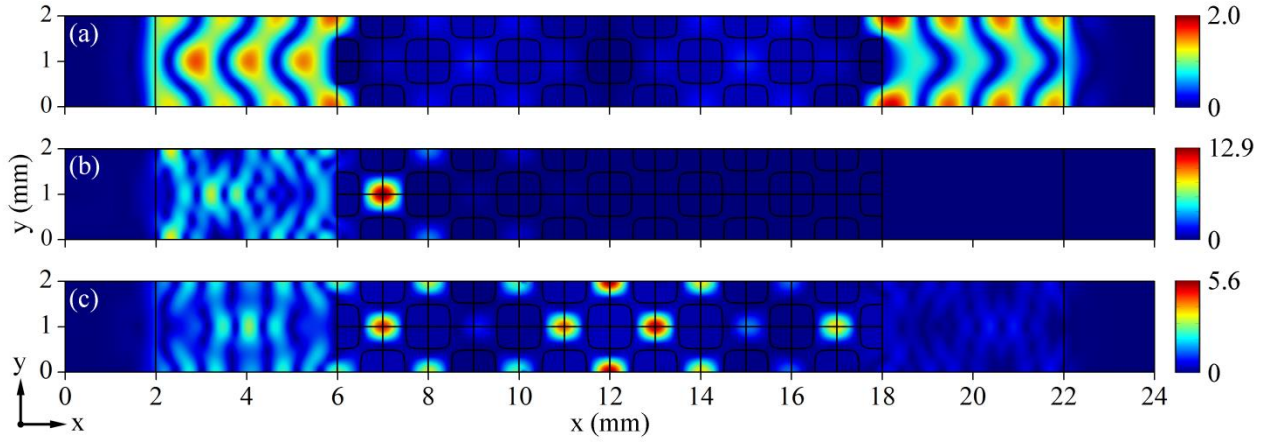

Figure 3.4 Total displacement fields for different excitation frequencies. (a) Below, 0.85 MHz, (b) within, 1.28 MHz and (c) above, 1.36 MHz, the band gap associated with the points A, B, and C in Fig. 3 (c), respectively. The incident wave with an amplitude of 1 μm is placed at x=2 mm along ΓX direction and the displacements are collected at the interface x=22 mm. Periodic boundary conditions are applied at the surfaces along y and z directions. The domains within x= [0, 2] and [22, 24] mm are defined as Perfectly Matched Layers. [24]

3.3.3 Tunability of complete wave band gaps

Acoustic metamaterials operating over narrow bandwidths are not desirable in engineering practice. To overcome this limitation, several approaches have been proposed to broaden the width of complete band gaps, including optimization of phononic structures, [88] introduction of more levels of structural hierarchy, [27] and use of mechanical deformation. [89] Here we examine the effect of volume fraction of Phase A on the frequency tunability in the co-continuous metamaterials. Figure 3.5 plots the evolution of the complete band gaps, where for the metamaterial with SC lattice, the complete band gap opens at V_f ≈57% and closes at V_f ≈60%, suggesting that only a small complete band gap can be achieved in a limited frequency range.

While the frequency ranges of the complete band gaps in metamaterials with BCC, FCC, and octet-truss lattices are gradually increased as the volume fraction increases. Notably, the maximum widths of the complete band gaps in the metamaterials with BCC, FCC, and octet-truss lattices are 0.054 MHz, 0.079 MHz, and 0.075 MHz, respectively. These results indicate that we can achieve desired complete band gaps by tailoring topological arrangements and volume fraction of the co-continuous metamaterials.

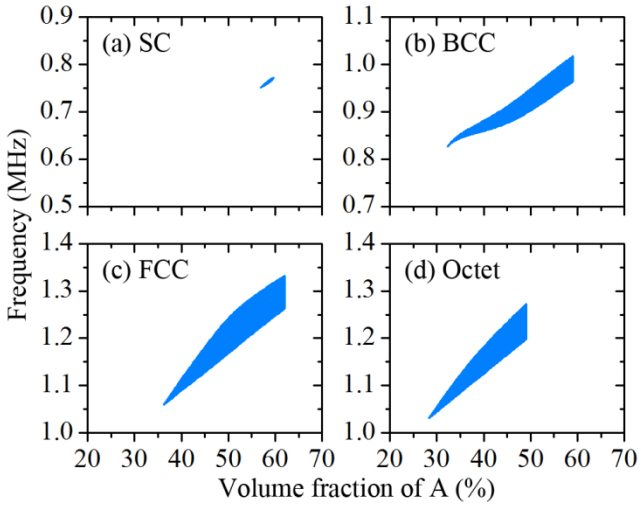

Figure 3.5 Effect of the volume fraction of Phase A on the evolution of complete band gaps in the co-continuous acoustic metamaterials. (a) SC, (b) BCC, (c) FCC, and (d) octet-truss lattices.

3.4 Conclusions

In summary, a group of triply periodic co-continuous acoustic metamaterials with a unique combination of wave attenuation capability and enhanced mechanical properties have been reported. Unlike other pure locally resonant or Bragg band gaps, the complete band gaps reported here result from the coupling effects of local resonances and Bragg scattering, which are intrinsically governed by the topological arrangements of the co-continuous structures and mechanical properties of constituent phases. The complete wave band gaps resulting from this

coupling mechanism is typically larger than that induced by pure local resonances. In addition, from an engineering perspective, the localized kinetic energy resulting from local resonances could be converted into electrical energy by introducing piezoelectric materials, which could be coated on the surfaces of one phase or alternatively chosen as the soft phase. Meanwhile, the enhanced mechanical properties resulting from the synergistic mechanism of the co-continuous structures and constituent phases provides opportunities to design mechanically robust acoustic metamaterials for wave absorption under harsh environments, such as for deep water applications where high hydrostatic pressure, high dynamic load, and wave coexist. The multifunctionality in the proposed co-continuous metamaterials will be of particular interest for aerospace, automotive, and defense industries where mechanical robustness, wave filtering, and self-powering capabilities are simultaneously pursued.

CHAPTER 4. 2D BIO-INSPIRED ARCHITECTED MATERIALS FOR BROADBAND WAVE FILTERING AND WAVEGUIDING

4.1 Introduction

It has been shown in Chapter 3 that 3D co-continuous metamaterials can exhibit simultaneous mechanical robustness and vibration mitigation capability. The resultant complete wave band gaps are relatively large compared with those induced by the pure locally resonant effect. However, as shown in phononic dispersion relations, each type of metamaterials only exhibit one complete band gap. In complex environmental conditions where noise and vibration sources are random, broadband and multiband wave filtering capability are highly desired.

In this chapter, a new system of 2D bioinspired architected metamaterials will be proposed to explore broadband and multiband wave filtering and waveguiding features. The metamaterials design concept presented here is inspired by the observation that many biological materials have developed the capability to shield from external attacks and maintain their structural integrity. This remarkable feature motivates us to investigate the relation between stress wave reduction and the inherent architectures of structural biological materials. Here we will focus on elastic wave propagation in periodic composites with 2D nacre-like, brick-and-mortar microstructure using finite element analysis. First, the existence of complete band gaps and the mechanisms responsible for band gap formation will be investigated. Then, we will validate the simulated band gaps through analyzing elastic wave propagation in the periodic composites consisting of a finite number of unit cells. Finally, the effects of topological arrangement of the mineral platelets and the material properties of organic matrix on the frequency tunability of band gaps will be studied.

Indeed, besides the brick-and-mortar-like architecture, other geometric characteristics such as hierarchy and heterogeneity are prevalent in nacreous composites. For example, many structural biological composites have developed multilevel of structural hierarchy to improve their mechanical performance and the capability to maintain their structural integrity under external attack. [90-92] Multilevel structural hierarchy is observed in a wide range of systems from chromosome, protein, cell, tissue to organisms. In addition, heterogeneous architecture is another important geometric characteristic of biological composites that enable an unusual combination of mechanical performance. [47, 48] For example, in nacreous composites, there is the prismatic layer where mineral platelets are orientated vertically on the top of brick-and-mortar architecture. [45] This heterogeneous architecture allows for enhanced stiffness and a surface hardness of the upper layer and enhanced flexural modulus and fracture toughness in the inner layer.

The mechanical performances of bio-inspired hierarchical composites and heterogeneous composites have been studied extensively. However, the interplay between the hierarchy and heterogeneity and the dynamic response of structural biological composites has not been revealed. In this chapter, wave propagation in bio-inspired composites with hierarchy and heterogeneity will be systematically investigated.

4.2 Wave filtering capability of the bio-inspired architected materials

4.2.1 Model description

The considered periodic composites with nacre-like microstructure consist of multilayered staggered mineral platelets embedded in the organic matrix, as schematically illustrated in Figure 4.1 (a). The periodicity of the 2D microstructure is characterized by a rhombic lattice with vectors

$$\mathbf{a}_1 = \left[\left(L + d \right)/2,\ \tan\alpha \cdot \left(L + d \right)/2 \right]$$

$$\mathbf{a}_2 = \left[(L+d)/2, -\tan\alpha \cdot (L+d)/2 \right] \tag{4.1}$$

where L is the length of the mineral platelet, d is the thickness of the organic matrix along x direction and α is the lattice angle. (see Figure 4.1(b)). The volume fraction (V_f) of the mineral platelets is characterized as

$$V_f = \frac{2Lh}{(L+d)^2 \cdot \tan\alpha} \tag{4.2}$$

where h is the height of the mineral platelets. Note that the manner of defining volume fraction using the lattice angle enables us to distinguish the first irreducible Brillouin zone for the unit cell with different lattice angles and hence provides a convenient way to parametrically study the effect of geometric features on the evolution of band gaps.

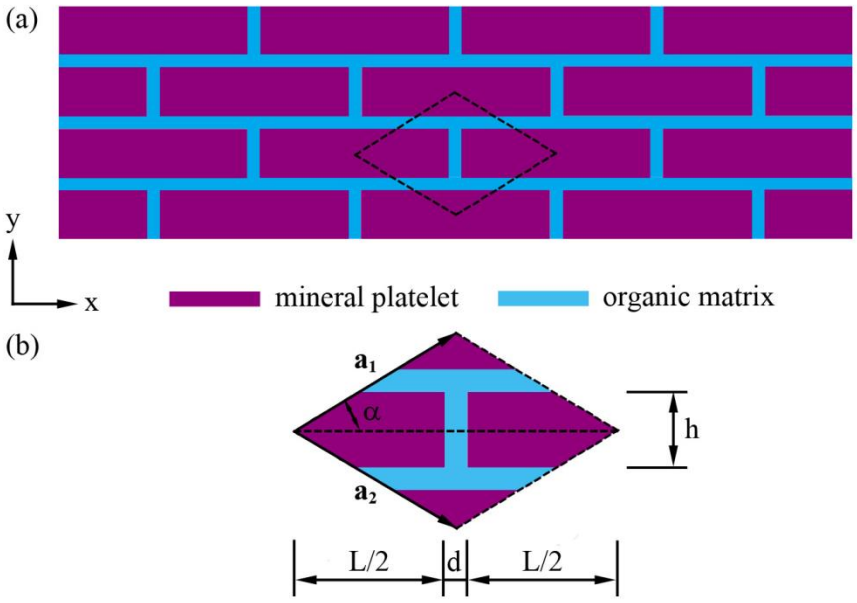

Figure 4.1 Schematic illustration of the 2D bioinspired periodic composite. (a) 2D nacre-like periodic composites consisting of mineral platelets and organic matrix. (b) 2D unit cell. L is the length of the mineral platelets; d is the thickness of the organic matrix along x direction and α is the lattice angle.

The procedure of constructing Brillouin zones is similar to that of 3D co-continuous metamaterials reported in Chapter 2. Here the first irreducible Brillouin zones of the unit cells with different ranges of lattice angles are constructed by following the same routine, as shown in Figure 4.2.

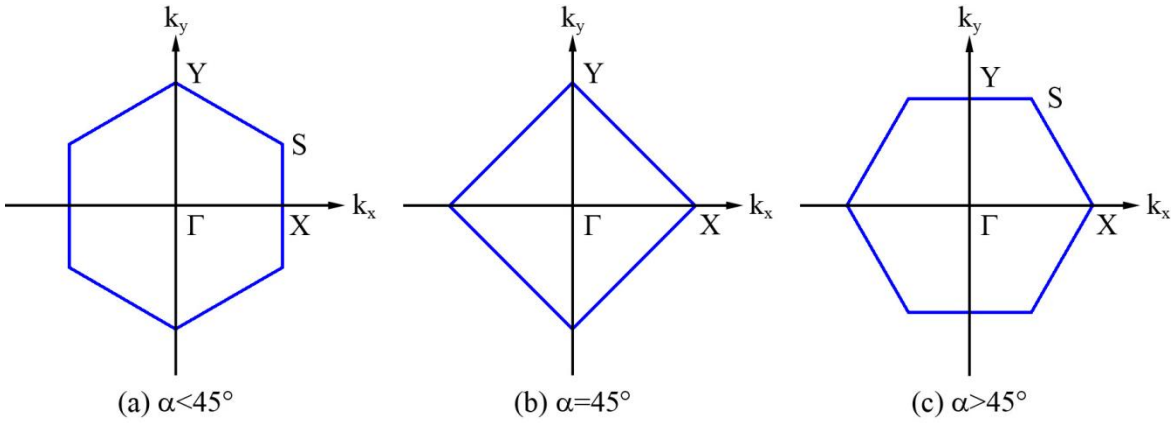

Figure 4.2 The first irreducible Brillouin zones for the composites with different lattice angles.

(a) α<45°, $\Gamma=(0,\ 0)$, $\mathrm{X}=\left(\frac{2\pi}{(L+d)},\ 0\right)$, $\mathrm{S}=\left(\frac{2\pi}{(L+d)},\ \frac{2\pi\cdot\cot 2\alpha}{(L+d)}\right)$, $\mathrm{Y}=\left(0,\ \frac{2\pi\cdot\csc 2\alpha}{(L+d)}\right)$;

(b) α=45°, $\Gamma=(0,\ 0)$, $\mathrm{X}=\left(\frac{2\pi}{(L+d)},\ 0\right)$, $\mathrm{Y}=\left(0,\ \frac{2\pi}{(L+d)}\right)$, and (c) $\alpha>45$ °,

$$\Gamma=(0,\ 0),\ \mathrm{X}=\left(\frac{\pi\csc^2\alpha}{(L+d)},\ 0\right),\ \mathrm{S}=\left(\frac{\pi\left(1-\cot^2\alpha\right)}{(L+d)},\ \frac{2\pi}{(L+d)\cdot\tan\alpha}\right),\ \mathrm{Y}=\left(0,\ \frac{2\pi}{(L+d)\cdot\tan\alpha}\right)$$

The mineral platelets and the organic matrix are assumed to be linearly elastic, homogeneous, and isotropic. The length of each mineral platelet is L=10 μm and the thickness of the organic matrix along x direction is $d=L/50$=0.2 μm, which are similar to the values reported in nacre. [93-95] The material properties of the mineral platelets and the organic matrix are assigned as follows unless otherwise specified: for the mineral platelets, Young's modulus E_m =100 GPa, density ρ_m

=2950 kg/m^3, and Poisson's ratio ν_m=0.30; for the organic matrix, Young's modulus E_o=20 MPa, density ρ_o=1350 kg/m^3, and Poisson's ratio ν_o=0.30.

To investigate the wave attenuation capability of the 2D bio-inspired composites, phononic dispersion relations are constructed by performing eigenfrequency analysis within the finite element framework using the commercial package COMSOL Multiphysics. Note that we focus on the in-plane wave propagation in the 2D composites, thus a plane strain assumption is made without loss of generality. To capture the periodic feature of the idealized composites, Bloch's periodic boundary conditions are applied at the boundaries of the unit cell. The unit cell is discretized using 6-node triangular elements. We then solve the wave equation by scanning the wave vectors in the first irreducible Brillouin zone. More details concerning the modeling of wave propagation can be found in Chapter 2.

4.2.2 Phononic dispersion relation

The phononic dispersion relations of the unit cells with different lattice angles are constructed to examine the existence of complete wave band gaps in the considered composites. The volume fraction of the mineral platelets in each unit cell is set as 0.90 for comparison purposes. Phononic dispersion relations of the unit cells with lattice angles α=10°~75° are shown in Figure 4.3. Multiple band gaps arise in the band structures of the unit cells with lattice angles α=10°~30°. The frequency range of the widest band gap is ω=162~200 MHz for α=10°, ω=105~180 MHz for α=15°, ω=38~133 MHz for α=30°. In contrast, only one complete band gap exists in each phononic dispersion relation of the unit cell when the lattice angle increases to α=45°~75°. These results suggest the existence of band gaps in the periodic composites with nacre-like microstructure

and also indicate that the geometric feature of the unit cell, i.e., the lattice angle, is significantly associated with the evolution of band gaps.

To reveal the mechanism of band gap formation in the considered composites, phononic dispersion relation of the unit cell with lattice angle $\alpha = 15°$ (Figure 4.3 (b)) is further discussed. The very flat bands are observed in the band structure and correspond to localized modes. The eigenmodes of the unit cells are plotted at given points (Point *A* and *B*) on the flat bands, as shown in Figure 4.4 (a) and (b). Evidently, the total displacement is almost concentrated in the organic matrix, indicating that the local resonances arise in the soft phase. Therefore, the formation of the band gap bounded by the flat bands is derived from locally resonant effects. However, the first band gap in the band structure is bounded by two normal bands and hence can be termed as a Bragg-type band gap, which is further supported by the corresponding eigenmodes at points *C* and *D* (Figure 4. 4(c) and (d)).

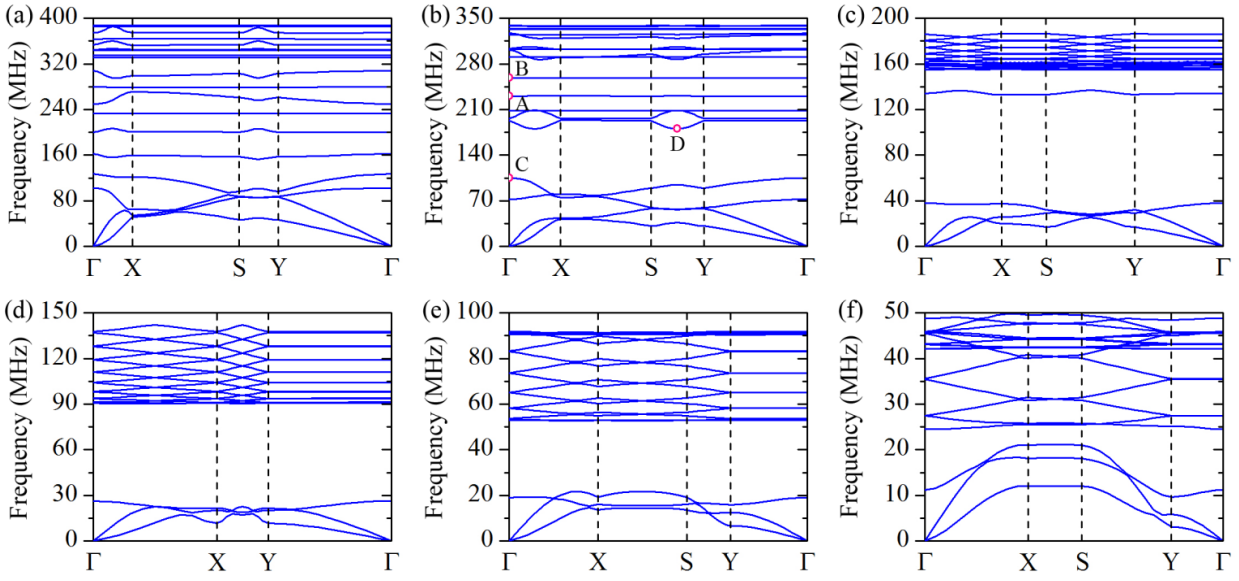

Figure 4.3 Phononic dispersion relations of the unit cells with different lattice angles. (a) $\alpha = 10°$, (b) $\alpha = 15°$, (c) $\alpha = 30°$, (d) $\alpha = 45°$, (e) $\alpha = 60°$ and (f) $\alpha = 75°$. The volume fraction of the mineral platelets is $V_f = 0.90$.

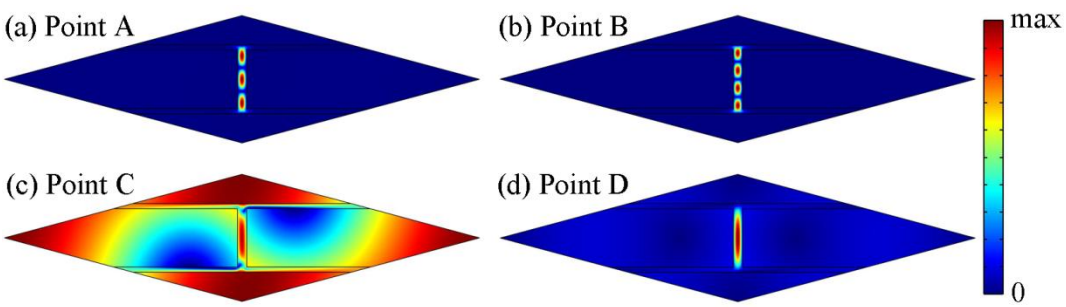

Figure 4.4 Eigenmodes of the composites at the representative points in the band structure. The color scale indicates the amplitude of total displacement.

4.2.3 Wave transmission of bioinspired architected materials

Now we investigate the behavior of elastic wave propagation in the periodic composites consisting of a finite number of unit cells. The goal of this analysis is, on the one hand, to validate the simulated complete band gaps by calculating the transmission coefficient of elastic wave propagation, and on the other hand, to further reveal the mechanisms of band gap formation by observing the deformation behavior of the periodic composites. The periodic composite under investigation consists of an assembly of 4×8 unit cells sandwiched by two homogeneous parts of the organic matrix, as illustrated in Figure 4.5 (a). The volume fraction of mineral platelets is V_f =0.90 and the lattice angle is α=15° in the unit cell. To determine the transmission coefficient along YΓ direction, an incident elastic wave along *y* direction is modeled by applying harmonic displacements with an amplitude of u_0=0 and v_0=100 nm in the *x* and *y*-direction, respectively, at line S. Perfectly matched layers (PMLs) are applied at the two ends of the homogeneous part to prevent reflections by the scattering waves from the domain boundaries.[24] In addition, periodic boundary conditions are applied to the left and right edges of the considered composite. The transmission coefficient is defined as $\phi = 20\log\left[\left(|u|+|v|\right)/\left(|u_0|+|v_0|\right)\right]$, where *u* and *v* are

horizontal and vertical displacements collected along the interface between PML and homogeneous part on the bottom side.

The frequency domain analysis sweeping from 0 to 350MHz is performed and the simulated transmission coefficient as a function of frequency is plotted in Figure 4.5 (c). Strong attenuation zones can be observed in the transmission spectrum, which agrees well with the corresponding partial band gaps along YΓ direction in the phononic dispersion relation (Figure 4.5 (b)). This confirms that the simulated band gaps using Bloch theorem is reliable and demonstrates the potential application of finite periodic composite as elastic wave filters.

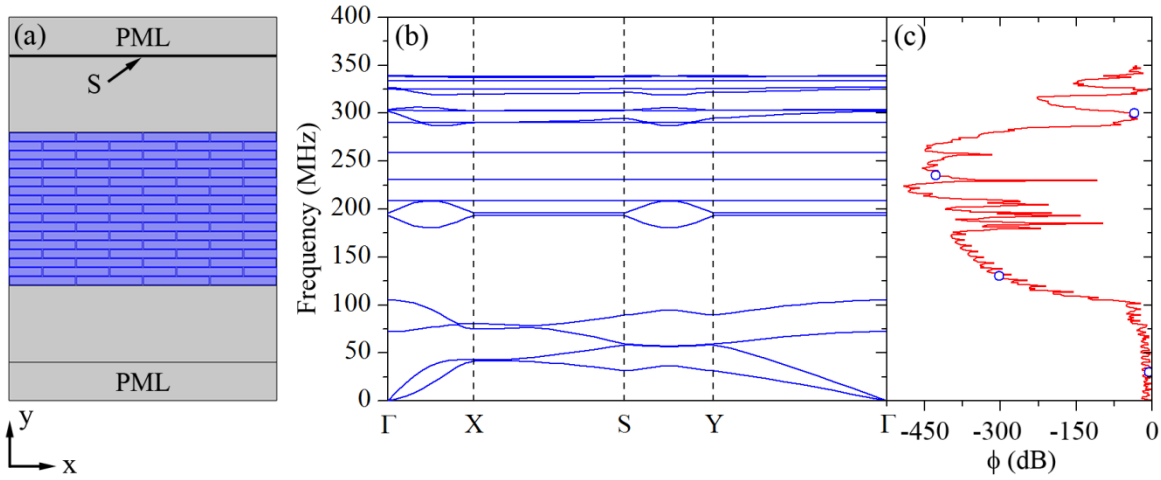

Figure 4.5 Frequency domain analysis for finite-size bioinspired structures. (a) FEA model of the finite periodic composite consisting of 4×8 unit cells sandwiched by two homogeneous parts, where α=15° and V_f = 0.90. (b) The corresponding phononic dispersion relation and (c) the transmission coefficient along the YΓ direction.

To gain further insight into the mechanism of band gap formation, we present in Fig.6 the displacement fields of the composite at excitation frequencies below, within and above the complete wave band gaps. Figure 4.6 (a) and (b) show the horizontal and vertical displacement fields of the finite periodic composite at the frequency of 30MHz, which is below the first band

gap. The incident elastic wave is partly reflected and partly passes through the periodic composite. A similar trend holds for the composite with incident wave frequency above the fourth band gap (Figure 4.6 (g)-(h)). In contrast, the incident elastic wave is almost totally reflected and confined in the top homogeneous part when the frequency of the incident wave (130MHz) lies within the first band gap (Figure 4.6(c)-(d)). This phenomenon is consistent with what have been experimentally observed in a periodic array of pillars when the frequency of incident surface elastic wave lies in a Bragg-type band gap. [18] When the frequency of the incident wave lies in the third band gap, as shown in Figure 4.6 (e) and (f), the vertical displacement is localized in the organic matrix of the first mineral layer and the amplitude is amplified to 447 nm, indicating that locally resonant effect plays a role in wave absorption. These results provide direct support to our previous identification of the Bragg-type and locally resonant band gaps in the same periodic composite. It also demonstrates that two mechanisms can be achieved simultaneously to maximize band gaps in the same composite.

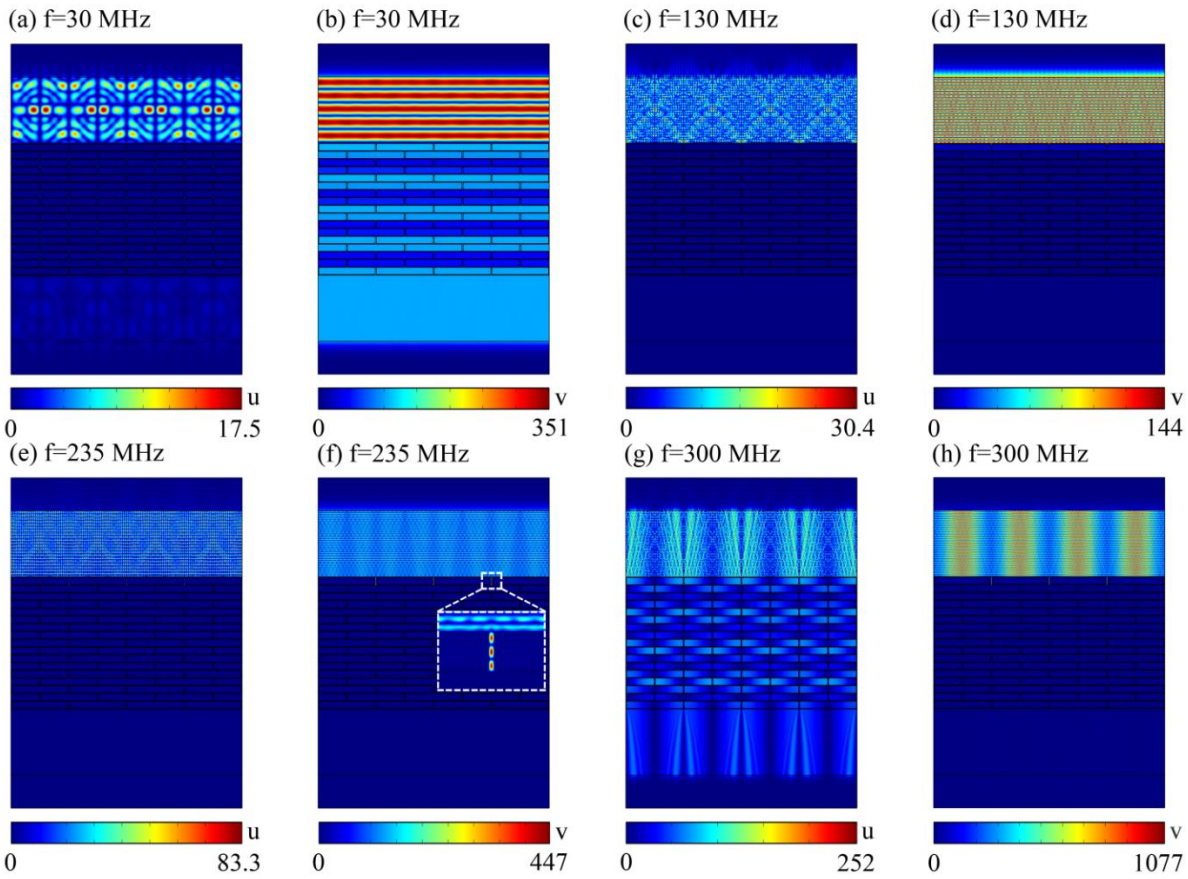

Figure 4.6 Displacement fields for elastic wave propagation in the considered periodic composite with different excitation frequencies. (a)-(b) 30 MHz, below the first band gap, (c)-(d) 130 MHz, within the first band gap, (e)-(f) 235 MHz, within the third band gap, and (g)-(h) 300 MHz, above the fourth band gap.

4.2.4 Effect of topological arrangement of mineral platelets

To understand the effect of the topological arrangement of mineral platelets on the evolution of complete wave band gaps, two geometric parameters, the volume fraction and the lattice angle, are chosen to perform a parametric study. The effect of volume fraction on the evolution of band gaps for the unit cells with different lattice angles is shown in Figure 4.7 (a)-(e). For the unit cell with a lattice angle $\alpha = 10°$, three complete band gaps are observed and the width of these band gaps

increases as the volume fraction increases from 0.50 to 0.80. When the volume fraction continues increasing, the width of the first two band gaps tends to shrink and several new band gaps arise. It shows that the maximum width of the first two complete band gaps is achieved at an intermediate volume fraction and these complete band gaps tend to close when the volume fraction is relatively high. This phenomenon is consistent with those have been observed in other 2D and 3D periodic composites, in which the band gaps are induced by Bragg scattering. [78, 96] This behavior still exists for the first complete band gap of the unit cell with α=15°. However, the width of the rest complete band gaps enlarges and shifts towards higher frequency range as the volume fraction increases. The maximum widths of these band gaps are observed at the volume fraction of 0.90. For the unit cell with lattice angle α=30°~60°, the maximum width of band gaps is all achieved at the volume fraction of 0.90. The only difference between these band gaps is that the band gaps open at larger volume fraction for larger lattice angle. These results indicate that the width of band gaps is governed by the volume fraction and hence can be tuned by tailoring the volume fraction for the unit cell with a given lattice angle.

The effect of lattice angle on the evolution of band gaps is presented in Figure 4.7 (f). The volume fraction of the mineral platelets is set as 0.90, where the periodic composite exhibits largest band gaps when the lattice angle is above 10°. The band gaps shift towards lower frequency range as the lattice angle increases. Two wide band gaps are observed for the unit cell with lattice angle α=15°~35°. Specifically, the maximum width of the first band gap is 95.03 MHz with a lattice angle of 30° and the maximum width of the second band gap is 80.06 MHz with a lattice angle of 20°. Moreover, the relative width of band gaps, which is defined as the ratio between gap width and the midgap location, in the unit cell with a lattice angle of 30° is 1.1, which is larger than those have been reported in other 2D and 3D periodic composites. [97-99]

These results indicate that the volume fraction of the mineral platelets and the lattice angle are two important geometric parameters governing the evolution of band gaps and indicate that we can achieve desired band gaps in the periodic composites with an optimal design.

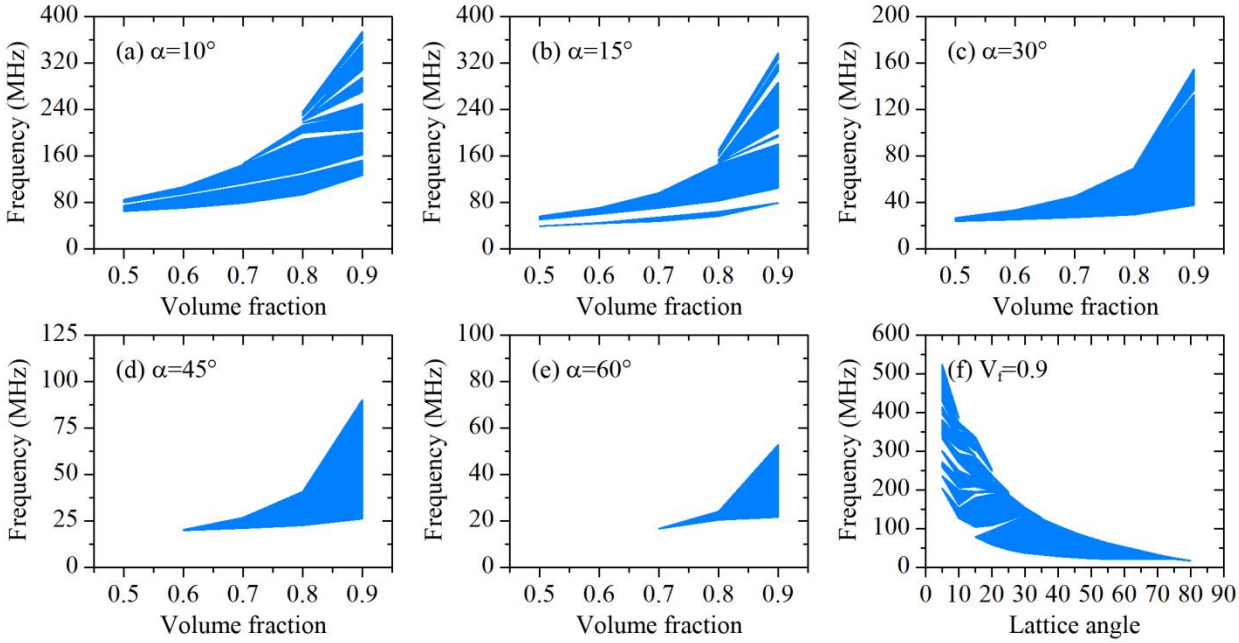

Figure 4.7 Evolution of complete band gaps as a function of the volume fraction of the mineral platelets with different lattice angles. (a) α=10°, (b) α=15°, (c) α=30°, (d) α=45°, and (e) α=60°. (f) Evolution of complete band gaps as a function of the lattice angle, where V_f = 0.90.

We have numerically demonstrated the capability to manipulate the elastic wave propagation in bio-inspired periodic composites with nacre-like microstructure. Multiple complete band gaps are observed in the periodic composites with a wide range of lattice angles and volume fractions. The formation of these complete band gaps can be attributed to Bragg scattering or local resonance in each unit cell or due to coexisting of them in the same periodic composites. Wide multiple complete band gaps can be obtained by utilizing these two formation mechanisms simultaneously. In addition, the investigation of elastic wave propagation in a finite periodic composite shows good

agreement between transmission coefficient and the simulated complete band gaps and further supports the origins of complete band gaps. The frequency tunability of complete band gaps can be achieved not only by engineering the length scale of the composites but also by tailoring the topological arrangement of the mineral platelets and material properties of each phase. The results of this work can help guide the creation of mechanically robust metamaterials while having integrated wave filtering capability.

Note that here we only consider the first level of the hierarchy of the nacre-like microstructure, while it has been observed that many biomaterials, e.g., nacre and bones, have a multi-level structural hierarchy with self-similar microstructures. [100] This, in turn, gives rise to the formation of band gaps in a broader frequency range on the transmission spectra of elastic wave propagation in one-dimensional periodic structure as compared to conventional periodic structures with single periodicity. [101] It is expected the hierarchy could also play a role to further improve complete band gaps and transmission spectrum of periodic composites with multi-level hierarchical nacre-like microstructures.

4.3 Hierarchical composites for broadband and multiple band wave filtering and waveguiding

This section aims to explore the elastic wave propagation in bio-inspired hierarchical composites with nacre-like and biocalcite-like architectures. These two types of architectures consist of hard mineral and soft organic phases, which are hierarchically assembled to develop multilevel of a structural hierarchy (Figure 4.8). Guided by the finite element modeling, we will show that multiple band gaps and passbands, covering an ultrawide frequency range, arise in the hierarchical composites with two levels of hierarchy. In particular, low-frequency band gaps, akin to the subwavelength characteristic in acoustic metamaterials, exist in the hierarchical composites with

two levels of hierarchy. The mechanisms responsible for the multiple band gaps and passbands are totally different, depending on the frequency ranges of the band gaps and passbands.

4.3.1 Characterization of the hierarchically architected composites

The proposed bio-inspired hierarchical composites have a nacre-like architecture and a biocalcite-like architecture with two levels (N=2) of a structural hierarchy (Figure 4.8. (a) and (b)). In the nacre-like composite, the soft organic phase is continuous, with the hard mineral platelets dispersed in the soft organic matrix. In the biocalcite-like composite, however, the soft organic platelets are distributed in the continuous hard mineral phase. The two-dimensional periodicity at each level of the hierarchical architectures is characterized by a rhombic lattice with vectors

$$\mathbf{a}_{n1} = \left[\left(l_n + t_n \right)/2,\ \tan\alpha_n \cdot \left(l_n + t_n \right)/2 \right]$$
$$\mathbf{a}_{n2} = \left[\left(l_n + t_n \right)/2,\ -\tan\alpha_n \cdot \left(l_n + t_n \right)/2 \right] \tag{4.3}$$

where l_n is the length of the mineral platelet, t_n is the thickness of the matrix, α_n is the lattice angle (Figure 4.8. (c) and (d)), and the subscript n denotes the order of structural hierarchy level. In this regard, the volume fraction of the mineral phase can be defined as

$$v_{fn} = 2 l_n h_n \Big/ \left[\left(l_n + t_n \right)^2 \cdot \tan\alpha_n \right] \tag{4.4}$$

for level n=1, 2 of nacre-like composite and level n=2 of the biocalcite-like composite; while for level n=1 of biocalcite-like composites, the volume fraction of mineral phase is given by

$$v_{fn} = 1 - 2 l_n h_n \Big/ \left[\left(l_n + t_n \right)^2 \cdot \tan\alpha_n \right] \tag{4.5}$$

where h_n is the height of the organic platelets at level n.

It is assumed that the overall volume fractions of mineral phase in the composites with N=1 and N=2 levels of the hierarchy are equal to V_{fn} =0.80. To ensure the self-similarity in each level of the composite with N=2 levels of hierarchy, the volume fraction of mineral phase in each level is given by $v_{fn} = \sqrt{V_{fn}} = 0.894$. In addition, the lattice angle is taken as α_n =30° in each level. For level n=1 of the nacre-like and biocalcite-like composites, l_1=10 μm and t_1= l_1/50=0.2 μm. Considering the trade-off between accuracy and computational burden, we use four unit cells (nine layers of hard minerals) along the vertical direction in each level of the structural hierarchy. Then the parameters in level n=2 can be calculated as l_2=97.69 μm and t_2= l_2/50=1.95 μm accordingly.

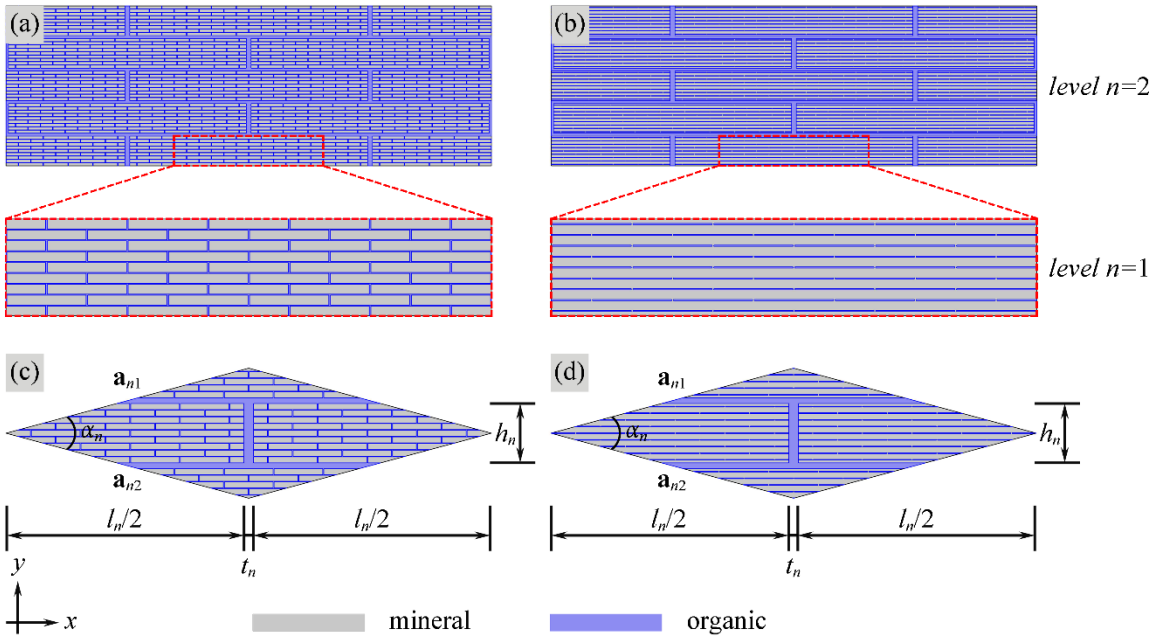

Figure 4.8 Schematics of the hierarchical composites and the associated supercells. (a)-(b): Nacre-like and biocalcite-like hierarchical composites with two (N=2) levels of structural hierarchy, where N is the total number of structural hierarchy level; (c)-(d) supercells of nacre-like and biocalcite-like hierarchical composites. The two-dimensional periodicity at each level is characterized by a rhombic lattice with vectors $\mathbf{a}_{n1} = [(l_n+t_n)/2, \tan\alpha_n\cdot(l_n+t_n)/2]$, and $\mathbf{a}_{n2} = [(l_n+t_n)/2,$

-tanα_n·(l_n+t_n)/2], where l_n is the length of the platelet, t_n is the thickness of the matrix, α_n is the lattice angle, and the subscript n denotes the order of structural hierarchy level.

4.3.2 Numerical modeling of wave propagation

Numerical simulation methods for phononic dispersion relations and transmission spectra can be found in Chapter 2. Here it is assumed the constituent phases of the hierarchical composites are homogeneous, isotropic and linearly elastic. Their properties are characterized by, Young's modulus E_m =100 GPa, Poisson's ratio ν_m =0.30, and density ρ_m =2950 kg/m^3 for the mineral phase, and Young's modulus E_o =1 GPa, Poisson's ratio ν_o =0.30, and density ρ_o =1350 kg/m^3 for the organic phase. [102-106]

4.3.3 Results and discussion

Figure 4.9 shows the transmission spectra of the normally incident elastic wave propagating in the nacre-like and biocalcite-like hierarchical composites with N=1 and N=2 levels of structural hierarchy. It is observed that in both composites with N=1 level of the hierarchy, about 7 wide continuous band gaps arise in the frequency range 0.4~1.5 GHz. These band gaps are attributed to Bragg scattering and/or local resonances, as our previous study revealed. [86] However, when the total number of the structural hierarchy is increased into N=2, the original wide continuous band gaps degenerate into multiple sharp band gaps and passbands. The most remarkable phenomenon in the transmission spectra of composites with N=2 levels of structural hierarchy is the emergence of 4~5 new band gaps located in low-frequency range 0~0.3 GHz, akin to the subwavelength characteristic of acoustic metamaterials. [22] These phenomena are similar to those observed in one-dimensional layered composites with multilevel hierarchies and two-dimensional solid-fluid system with fractal architectures. [27, 58] The difference is that these new features arising in the

proposed composites are obtained by simply assembling the mineral and organic phases in a hierarchical manner. Therefore, we believe that the structural hierarchy itself accounts for the low frequency and multiband features of the composites with N=2 levels of hierarchy. Specifically, the periodic arrangement of mineral and organic phases in hierarchical level n=2 leads to the emergence of low-frequency band gaps. At level n=1, however, the structural periodicity is interrupted, resulting in multiple shape band gaps and passbands.

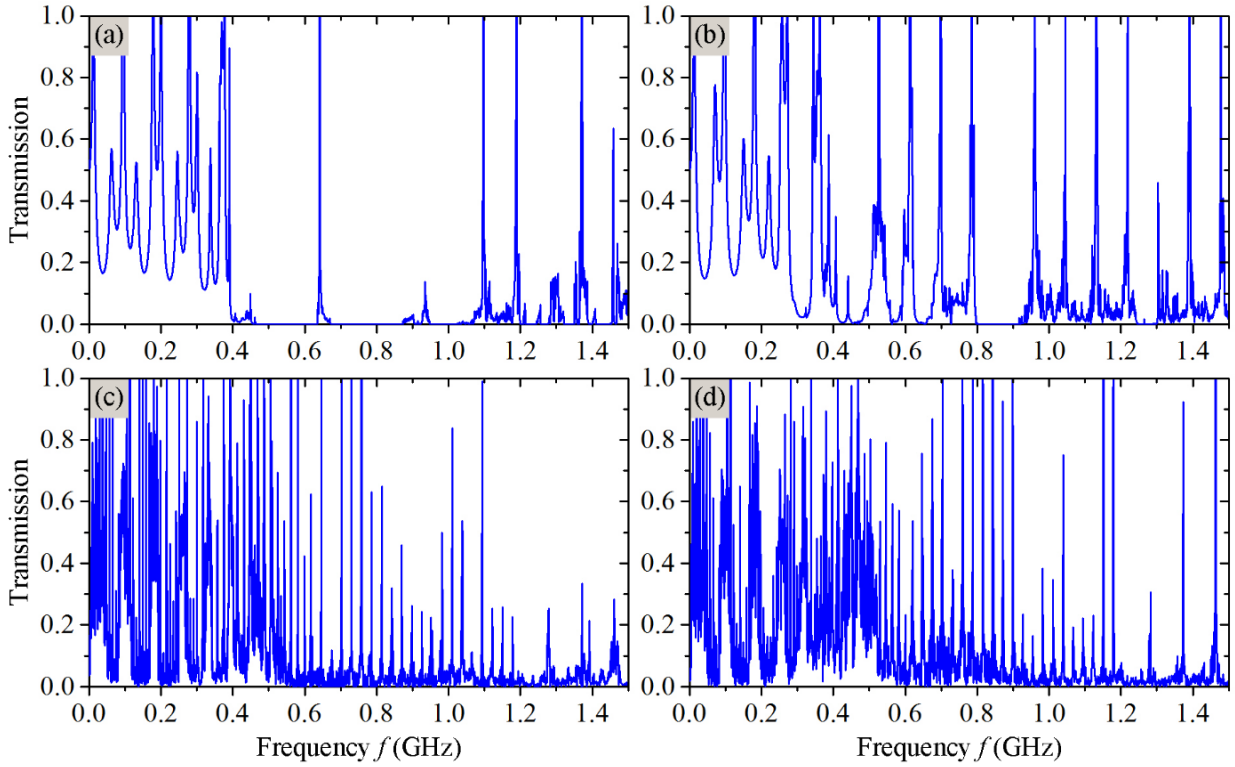

Figure 4.9 Transmission spectra of the proposed hierarchical composites with N=1 and N=2 level of the hierarchy. (a)-(b): Transmission spectra of nacre-like and biocalcite-like composites with N=1 level of the hierarchy; (c)-(d): Transmission spectra of nacre-like and biocalcite-like composites with N=2 levels of hierarchy. The overall volume fractions of mineral phase in the composites with N=1 and N=2 levels of the hierarchy are equal to V_{fn} =0.80.

To validate the hypothesis of low-frequency band gap formation, we calculate the phonon dispersion relations of the two types of hierarchical composites with N=2 levels of hierarchy. To this end, a two-dimensional supercell for each composite is considered to calculate the phonon dispersion relations (Figure 4.8. (c) and (d)). Note that the normally incident elastic wave propagation in the hierarchical composites corresponds to wave propagation along YΓ direction of their first irreducible Brillouin zones. [86] Figure 4.10 (a) and (c) present the phonon dispersion relations of nacre-like and biocalcite-like composites with N=2 levels of hierarchy, respectively. For the purpose of comparison, the transmission spectra within 0~0.3 GHz are also displayed (Figure 4.10. (b) and (d)). One notices that multiple partial band gaps arise in the dispersion relations, which agree well with the attenuation zones in the corresponding transmission spectra. This result supports that the low-frequency band gaps stem from the structural periodicity at level n=2 of the hierarchical composites. It is important to note that this low-frequency feature enables the design of compact and lightweight wave filters, thus providing more flexibility in engineering practice.

To gain a better understanding of the low-frequency band gap formation, we plot in Figure 4 the total displacement fields of the composites with N=2 levels of hierarchy under incident wave frequencies within the low-frequency band gaps, as well as frequencies at passbands. At frequencies f=0.079 GHz and f=0.071 GHz, within the band gaps of nacre-like and biocalcite-like composites, respectively, the incident wave is mostly reflected by the hierarchical composites, which is a strong evidence of Bragg scattering (Figure 4.11. (a) and (c)). By contrast, at frequencies of passbands, the normally incident wave can pass through both of the hierarchical composites without decay. These phenomena suggest that the low-frequency band gaps are Bragg-type, where the wavelengths of the elastic wave have the same order of magnitude as the structural periodicities

at level n=2 of the hierarchical composites. It is interesting to note that the widths of these low-frequency band gaps are much narrower than those of the continuous band gaps in hierarchical composites with N=1 level of the hierarchy. We believe that this is mainly because the contrast in elastic constants at hierarchical level n=2 is significantly reduced when the structural hierarchy is increased from N=1 to N=2. [86] To demonstrate this, we evaluate the stiffness contrasts of the hierarchical composite with a nacre-like architecture, as an example. For N=1, the stiffness contrast between mineral phase and the organic phase is given by $\gamma_{N=1} = E_{m1}/E_o = 100$, whereas for N=2, this contrast becomes $\gamma_{N=2} = E_{m2}/E_o = 30.8$, where E_o=1 GPa, E_{m1}= E_m=100 GPa, and E_{m2}=30.8 GPa is estimated by the shear lag model. [107] Intrinsically, the stiffness contrast is solely dictated by the geometric features of the nacre-like architecture including the level of the structural hierarchy, volume fraction, and lattice angle. This finding not only provides us a better understanding of the mechanisms accounting for the low-frequency band gaps but also suggests possible avenues design tunable phononic crystals with optimal band gaps.

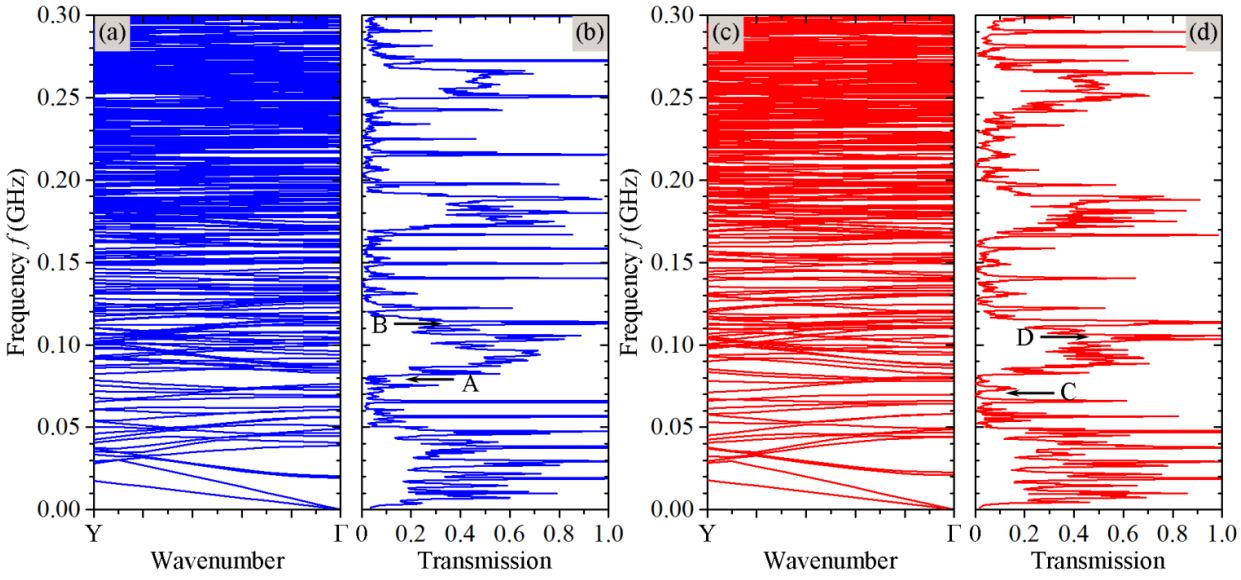

Figure 4.10 Phononic dispersion relations and transmission spectra for hierarchical composites. (a) and (c): phonon dispersion relations of nacre-like and biocalcite-like hierarchical composites at level n=2 along YΓ direction, where Y= $(0, \frac{\pi}{(l_n + t_n)} \cdot \left(\cot\frac{\alpha_n}{2} + \tan\frac{\alpha_n}{2} \right))$, and Γ= (0, 0); [86] (b) and (d): The corresponding transmission spectra of nacre-like and biocalcite-like composites with N=2 levels of hierarchy.

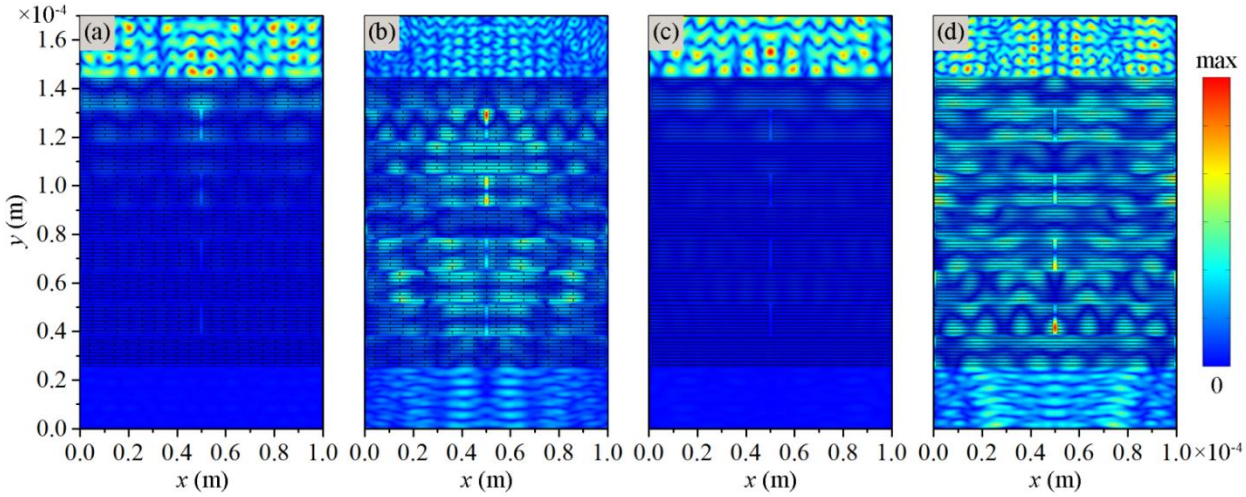

Figure 4.11 Total displacement fields of hierarchical composites with N=2 levels of hierarchy at different frequencies. (a) f=0.079 GHz, inside the band gap, and (b) f=0.113 GHz, at passband for nacre-like composites; (c) f=0.071 GHz, inside the band gap and (d) f=0.105 GHz, at passband for biocalcite-like composite. The positions of the selected frequencies for (a)-(d) are labeled as *A*, *B*, *C* and *D* in Figure 3, respectively.

Having revealed the mechanisms responsible for the low-frequency band gaps, we next explore the origin of a multiband feature of the composites with N=2 levels of hierarchy. Here the band gaps and passbands within high-frequency range 0.4~1.5 GHz are particularly interested. A direct comparison of transmission spectra between composites with N=1 and N=2 levels of structural hierarchy inspire us to postulate that the interrupted periodicity at hierarchical level n=1 is

responsible for the multiple sharp band gaps and passbands in the composites with N=2 levels of hierarchy. Indeed, the hierarchical composites with N=2 levels of hierarchy can be considered as two-dimensional periodic composites with defects. To validate this hypothesis, we calculate the transmission spectra of periodic composites without being interrupted, which is equivalent to the hierarchical composites with N=1 level of the hierarchy, except that here the volume fraction of the hard mineral phase is v_{fn}=0.894 (Figure 4.12.(a) and (b)). As expected, the perfectly periodic composites exhibit wide continuous band gaps, as compared to the multiple sharp band gaps and passbands of composites with N=2 levels of hierarchy. This phenomenon further supports our claim that the structural hierarchy itself is responsible for the multiband feature. In other words, the defects, acting as waveguides in the composites with N=2 levels of hierarchy, give rise to multiple band gaps and passbands.

To demonstrate that the waveguide modes are responsible for the multiple band gaps and passbands at high-frequency range, we present the total displacement fields of the composites with N=2 levels of hierarchy at these high frequencies. Note that for the purpose of comparison, the frequencies of selected band gaps and passbands also locate inside the band gaps of the perfectly periodic composites. At frequencies f=0.957 GHz and f=0.968 GHz, inside the band gaps, the elastic wave is well confined within the waveguides. This is because the wave propagation is prohibited by the surrounding perfectly periodic composites (Figure 4.13. (a) and (c)). At passbands, as indicated in Figure 4. 13. (b) and (d), the incident elastic wave is concentrated in the waveguides and transmits through the waveguides, and then radiates at the exits of the waveguides. Although some of the wave energy penetrates into the surrounding supercells, as indicated in Figure 4. 13 (d_1), we believe this energy only takes a small proportion and most of the concentrated wave energy transmits through the waveguide efficiently. This is supported by the high

transmission coefficient (0.75) of the elastic wave at f=1.039 GHz, which corresponds to a waveguide mode. Apparently, the physical mechanisms of multiple band gaps and passbands at high frequencies are totally different from those of low-frequency band gaps. We emphasize that the high-frequency band gaps and passbands of the hierarchical composites with N=2 levels of hierarchy correspond to waveguide modes, which result from the introduction of defects; whereas the continuous band gaps in the perfectly periodic composites and hierarchical composites with N=1 level of the hierarchy are attributed to Bragg scattering or local resonances. [86] It should be pointed out that the proposed hierarchical architectures with multilevel structural hierarchies also endow the composites with enhanced mechanical properties including high strength and high fracture toughness. [90, 107, 108] These additionally exceptional features together with the wave filtering and waveguiding capabilities imply the possibility to design phononic crystals suitable for mechanically challenging environmental conditions.

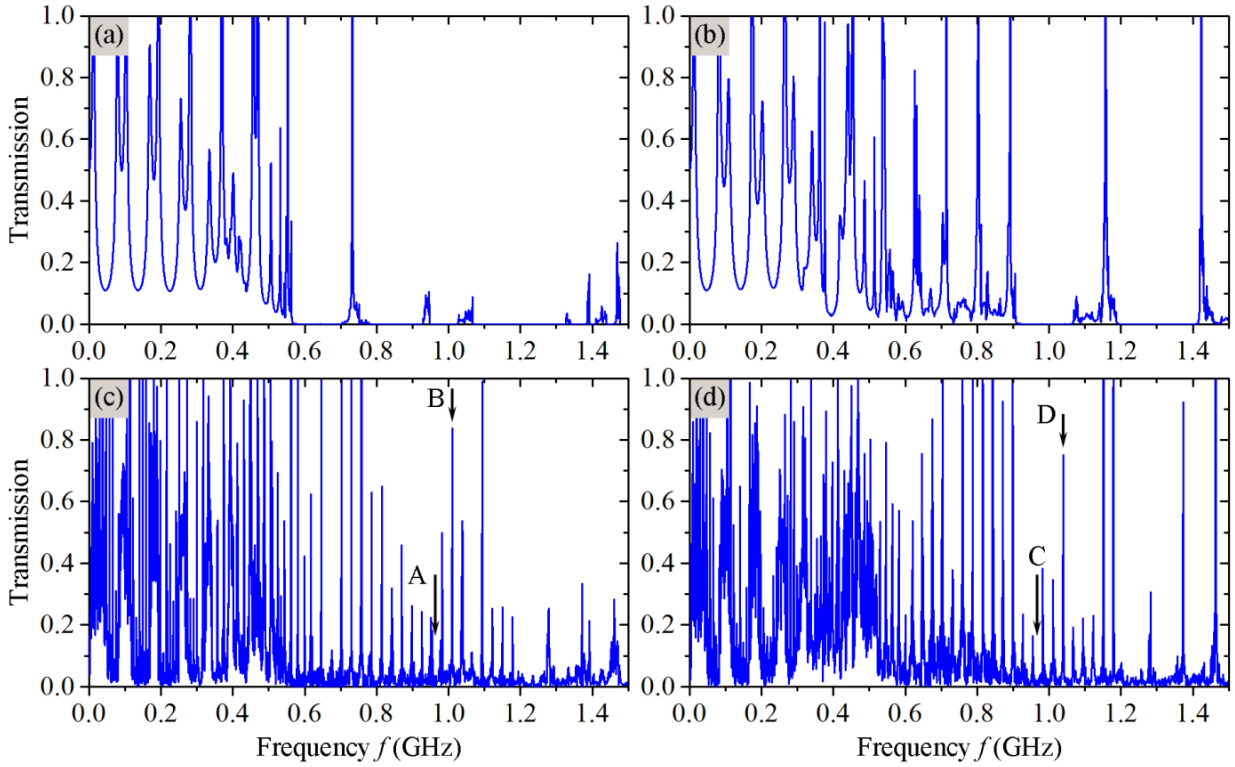

Figure 4.12 Comparison of transmission spectra for regular bioinspired structures and hierarchical structures. (a)-(b): Transmission spectra of nacre-like and biocalcite-like perfectly periodic composites without being interrupted, the unit cells of which are the same as those at level n=1 of composites with N=2 levels of hierarchy, except that here the volume fraction of the hard mineral phase is v_{fn}=0.894; (c)-(d): Transmission spectra of nacre-like and biocalcite-like composites with N=2 levels of hierarchy.

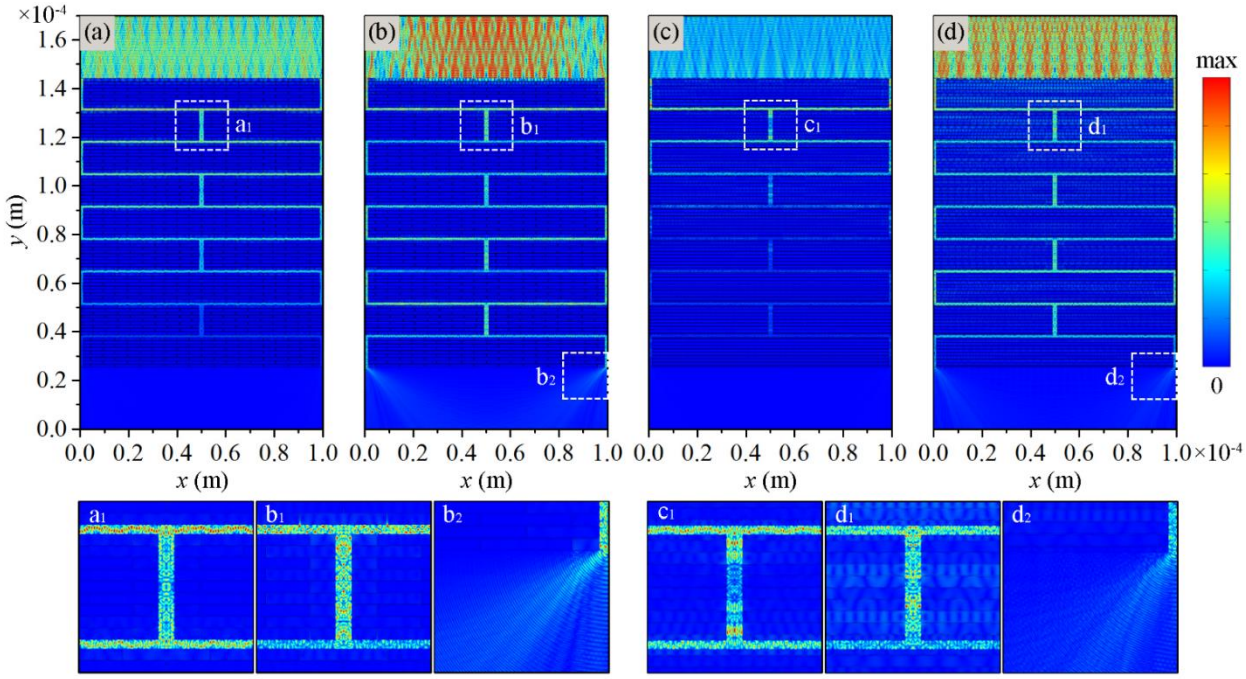

Figure 4.13 Total displacement fields of hierarchical composites with N=2 levels of hierarchy at different frequencies. (a) f=0.957 GHz, inside the band gap, and (b) f=1.010 GHz, at passband for nacre-like composites; (c) f=0.968 GHz, inside the band gap and (d) f=1.039 GHz, at passband for biocalcite-like composite. The positions of the selected frequencies for (a)-(d) are labelled as *A*, *B*, *C* and *D* in Figure 5, respectively.

4.4 Heterogeneous composites for broadband vibration mitigation

In this section, we will investigate the elastic wave propagation in bio-inspired heterogeneous composites, aiming at addressing the bandwidth limitation and the conflict between vibration mitigation and mechanical performance of conventional periodic structures. The model system under investigation consists of two layers where each layer consists of high volume of platelet-shape reinforcements embedded in the low-volume soft matrix, which is a typical brick-and-mortar microstructure of biological structural composites (see Figure 4.14 (a)). The vibration mitigation capability of the proposed heterogeneous composites is demonstrated by studying the transmission property of the normally incident elastic wave using the finite element method. Physical mechanisms responsible for the vibration mitigation are revealed. Furthermore the effect of local characteristics of the heterogeneous architecture on the wave attenuation capability is investigated.

4.4.1 Model description

Figure 4.14 (b) shows the schematics of the proposed heterogeneous architecture consists of two layers with elastic wave incident normally to the top surface. The periodicity of each layer is characterized by a rhombic lattice with vectors $\mathbf{a}_1 = [(l+d)/2, \tan\alpha\cdot(l+d)/2]$ and $\mathbf{a}_2 = [(l+d)/2, -\tan\alpha\cdot(l+d)/2]$, where l is the length of the mineral platelet, d is the thickness of the organic matrix and α is half of the lattice angle (see Figure 4.14 (c)). The volume fraction of the mineral platelets is defined as $V_f = 2Lh/[(l+d)^2 \tan\alpha]$, where h is the height of mineral platelet. Here we assume l=10 μm and d=0.2 μm, which are similar to the reported geometric parameters of nacre. [94, 95, 109] The lattice angle in each layer is taken as $2\alpha = 30°$. For these given lattice constants of the unit cell, the first Brillouin zone can be constructed accordingly (see Figure 4.14 (d)). The mineral platelets and the organic matrix are assumed isotropic and linearly elastic. Their properties are characterized

by, Young's modulus E_m =100 GPa, Poisson's ratio ν_m =0.30, and density ρ_m =2950 kg/m^3 for mineral platelets; Young's modulus E_o =20 MPa, Poisson's ratio ν_o =0.30, and density ρ_o =1350 kg/m^3 for organic matrix. The transmission spectra and phonon dispersion relations are obtained by conducting frequency domain analyses and eigenfrequency analyses, respectively. Details concerning the numerical simulations can be found in Chapter 2.

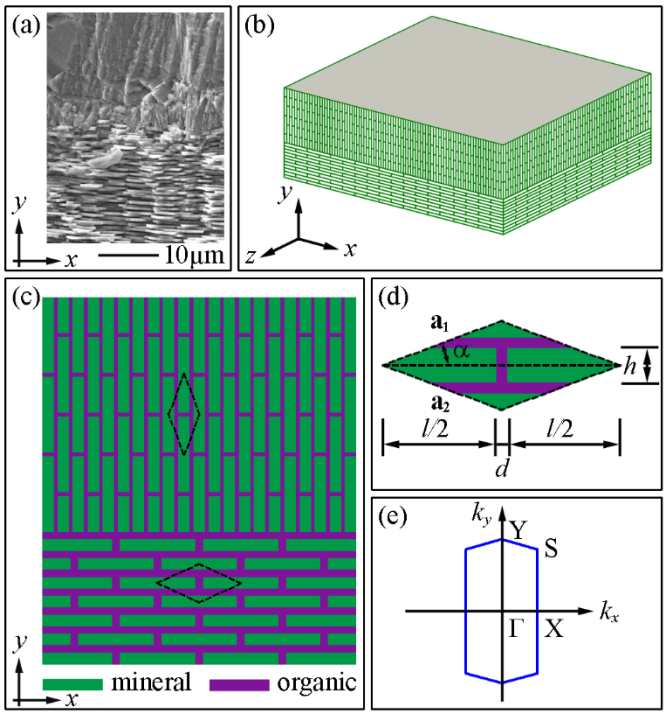

Figure 4.14 Schematics of the proposed bio-inspired composites with heterogeneous architecture. (a) A scanning electron microscope image of the cross-section of the prismatic layer and nacreous layer in a *Trochus niloticus* shell. (b) Heterogeneous architecture of the proposed composite consists of two layers, where the normal of the layers is perpendicular to the *x*-*z* plane. The minerals in the upper layer are oriented in the *y*-direction while the mineral platelets in the lower layer are oriented in the *x*-direction. (c) Idealized 2D representative of the proposed heterogeneous composite architecture. (d) Unit cell for the calculation of the phononic dispersion relation and (e)

the corresponding first Brillouin zone. The lattice constants are given by $\mathbf{a_1} = [(l+d)/2, \tan\alpha\cdot(l+d)/2]$ and $\mathbf{a_2} = [(l+d)/2, -\tan\alpha\cdot(l+d)/2]$, where l is the length of the mineral platelet, d is the thickness of the organic matrix and α is one half of the lattice angle. h is the height of mineral platelet.

4.4.2 Broadband vibration mitigation

Figure 4.15 (a) shows the transmission spectrum of the proposed heterogeneous composite, where the volume fractions of the mineral platelets in the lower layer and the upper layer are set to 0.70 and 0.90, respectively, mimicking those in typical structural biological materials. Multiple attenuation zones within 46~285 MHz are observed in the transmission spectrum as compared to the transmission spectrum of the bulk mineral. To gain an intuitive understanding of these multiple attenuation zone formations, we calculate the transmission spectrum of each constituent layer, as shown in Figure 4.15 (b) and (c). The resulting attenuation zones of the lower layer mostly lie within 46~179 MHz, while the attenuation zones of the upper layer appear within 104~285 MHz. Note that the bandwidths of the attenuation zones in each constituent layer are narrower than those of the heterogeneous composite are. By comparing the frequency ranges of the attenuation zones in each layer with those of the heterogeneous composite, we believe that the broadband wave attenuation capability results from the direct superimposition of attenuation zones in each constituent layer. To demonstrate this, we divide the broadband wave attenuation zones in transmission spectrum of the heterogeneous composite into three regions, which are regions I (f=46~96 MHz), II (f=104~179 MHz), and III (f=207~285 MHz), respectively. By comparing these regions with the attenuation zones of each constituent layer, we can conclude that region I and III mainly result from the attenuation zones in the lower and upper layer, respectively. However, the enhanced attenuation zones in region II are attributed to the direct superimposition of those in both

lower and upper layer. If the frequency is normalized by $\varpi = fa/2\pi c_t$ where a=10μm is the lattice constant and c_t=75.5 m/s is the transverse velocity of the matrix phase, the widths of attenuation zones in region I, II, and III are 1.05, 1.58, and 1.64, respectively. These findings indicate that broadband and enhanced wave attenuation capability can be readily achieved by designing the heterogeneous composites with two distinct constituent layers, leading to direct enhancements in vibration mitigation.

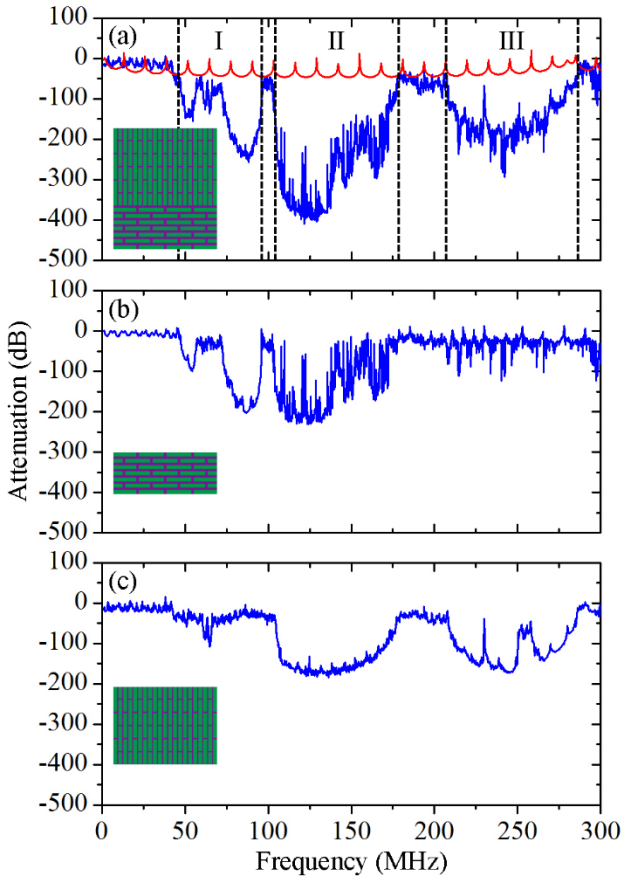

Figure 4.15 Transmission spectrum of the proposed heterogeneous composites. (a) Transmission spectrum of the proposed heterogeneous composite (the blue line), which is divided into three regions I, II, and III, and transmission spectrum of the bulk mineral (the red line). (b)-(c)

Transmission spectrum of the lower layer and upper layer, respectively. The insets show the schematics of the heterogeneous composite and its lower and upper layer.

To qualitatively show the broadband wave attenuation capability of the proposed heterogeneous composite, we plot in Figure 4.16 the total displacement field of the heterogeneous composite at incident frequencies below the attenuation zones and within regions I, II and III, respectively. At the frequency f=25.8 MHz, below the attenuation zones, the incident wave can pass through the heterogeneous composite without decay. Interestingly, when the incident frequency, f=79.8 MHz, lie within region I, the incident wave passes through the upper layer without decay, whereas it is totally reflected by the lower layer. This observation is consistent with our finding that the attenuation zones within region I are attributed to the lower layer. When the incident frequencies, f=127.4 MHz and f=236.2 MHz, lie within region II and III, respectively, the incident wave is mostly reflected by the upper layer, indicating that the proposed heterogeneous composite can mitigate vibration more effectively.

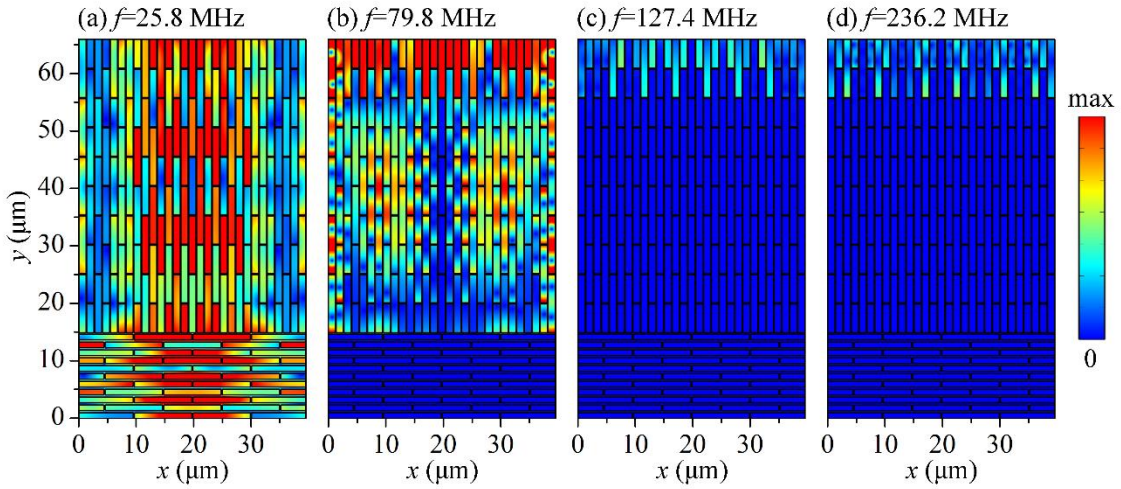

Figure 4.16 Total displacement field of the proposed heterogeneous composite under different incident wave frequencies. (a) f=25.8 MHz, below the attenuation zones, (b) f=79.8 MHz, within

region I, (c) f=127.4 MHz, within region II and (d) f=236.2 MHz, within region III. The total displacement is calculated as the magnitude of overall displacement vector with horizontal and vertical components at each material point.

4.4.3 Physical mechanisms of the attenuation zones

To gain insight into the physical mechanisms responsible for the broadband attenuation zones of the heterogeneous composite, phonon dispersion relations need to be constructed. The proposed heterogeneous composite as a whole is not periodic; however, each constituent layer indeed is a two-dimensional periodic structure. In this regard, the phonon dispersion relation of each layer can be calculated accordingly, as shown in Figure 4.17 (a) and (b). Notice that the elastic wave incident normally on the top surface of the heterogeneous composite corresponds to wave propagation along YΓ and ΓX directions for the lower and upper layer, respectively. The partial band gaps along YΓ and ΓX directions in the phonon dispersion relations agree well with the attenuation zones in the transmission spectrum of each constituent layer. By superimposing the partial band gaps along these two directions, we can obtain broadband attenuation zones, which are consistent with those in Figure 4.15 (a). This result further confirms our claim that the broadband wave attenuation capability of the heterogeneous composite is achieved by directly superimposing the attenuation zones in each constituent layer.

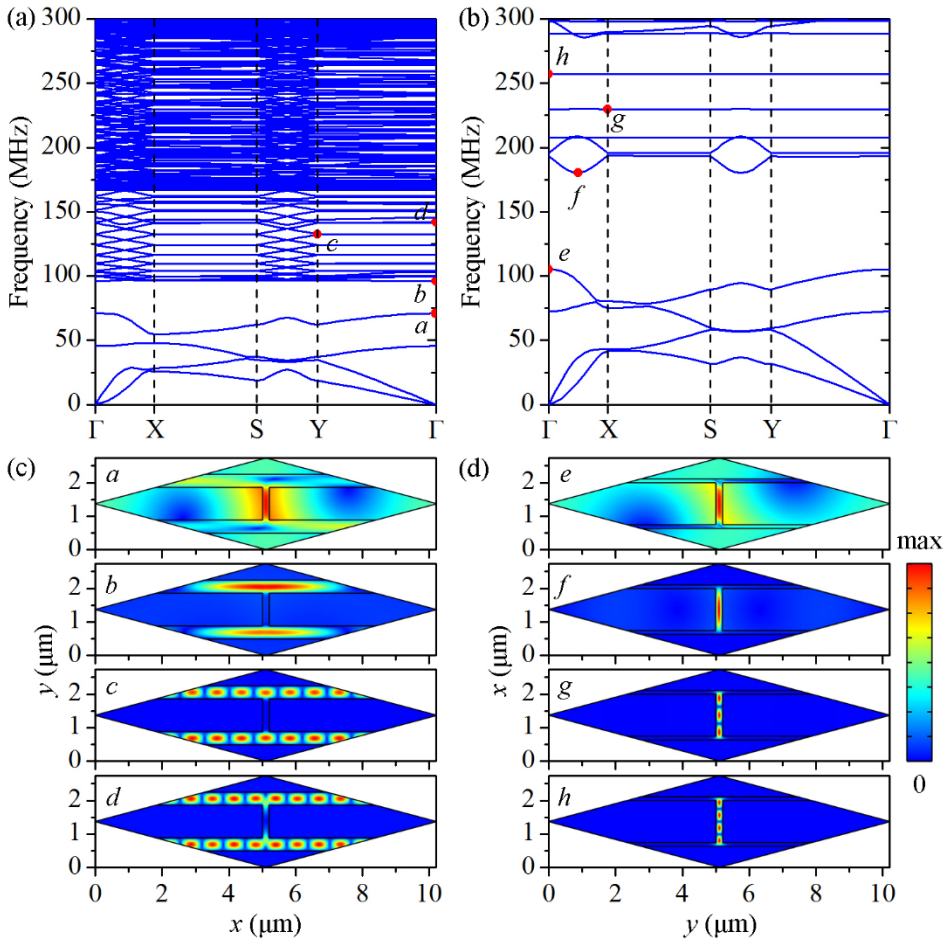

Figure 4.17 Phononic dispersion relation for each layer of the heterogeneous composites. (a)-(b): The phonon dispersion relation of the lower layer and upper layer, respectively; (c)-(d) typical eigenmodes on the edges of band gaps in the lower layer and upper layer. The volume fractions of mineral platelets in the lower and upper layer are set to 0.70 and 0.90, respectively.

Here the band gaps corresponding to attenuation region I, II and III are taken as examples to reveal the physical mechanisms of band gap formation. As previously predicted, the first two band gaps in each layer are due to Bragg scattering. [86] This is also supported by the typical eigenmodes on the lower and upper edges of the band gaps, as shown in Figure 4.17 (c) and (d). By contrast, some of the band gaps in the constituent layers, e.g., the ones pinned by point *c*, *d* and

g, *h*, are believed to result from local resonances. This observation is supported by the distinctive feature that the band gaps are bounded by flat bands, indicating that zero group velocity exists and hence the energy flow is prohibited. [18, 22, 78, 110] To give a better understanding of the local resonance effect, we plot in Figure 4.17 (c) and (d) the eigenmodes on the flat bands of the band gaps in lower and upper layers, respectively. The displacement field of each mode is totally localized in the soft organic matrix, preventing the elastic wave propagation. These characteristics indicate that the resulting band gaps are attributed to local resonances. Having determined the physical mechanisms of band gap formation in each layer, we are able to identify the mechanisms of superimposed attenuation region I, II and III in the heterogeneous composite, respectively. In short, the resulting broadband wave attenuation capability can be attributed to Bragg scattering and/or local resonances, depending on the mechanisms of the band gaps in each constituent layer.

4.4.4 Effects of mineral platelet orientation and concentration

Through millions of years' evolution, biological materials have optimized their shapes to handle external multidirectional loading conditions, whereby the biological materials exhibit enhanced site-specific mechanical properties. [47, 48, 106, 111-113] Importantly, this naturally widespread phenomenon has provided inspiration for researchers to produce heterogeneous composites with controlled reinforcement orientation and concentration. [46] We expect the proposed heterogeneous composites still exhibit broadband wave attenuation capability when the local orientation and concentration of the mineral platelets are rationally tailored to deal with external mechanical stimuli. To this end, we examine the effect of mineral platelet orientation and mineral platelet concentration on the transmission spectra of the proposed heterogeneous composites. Figure 4.18 shows the effect of mineral platelet orientation in the upper layer changing from 0 °to 90 °while remaining the same for the lower layer. Notice that the original broadband attenuation

zones persist when the angle is rotated from 0° to 15°. When the alignment angle reaches 45°, additional attenuation zones arise around 195 MHz. Remarkably, multiple additional attenuation zones arise between 180 MHz and 208 MHz when the alignment angle reaches to 75° and 90°. It should be noted that the wave attenuation capability is progressively enhanced with the increase of the alignment angle from 0° to 90°. These results indicate that the proposed heterogeneous composites can maintain the broadband wave attenuation capability when the mineral platelet orientation is locally manipulated.

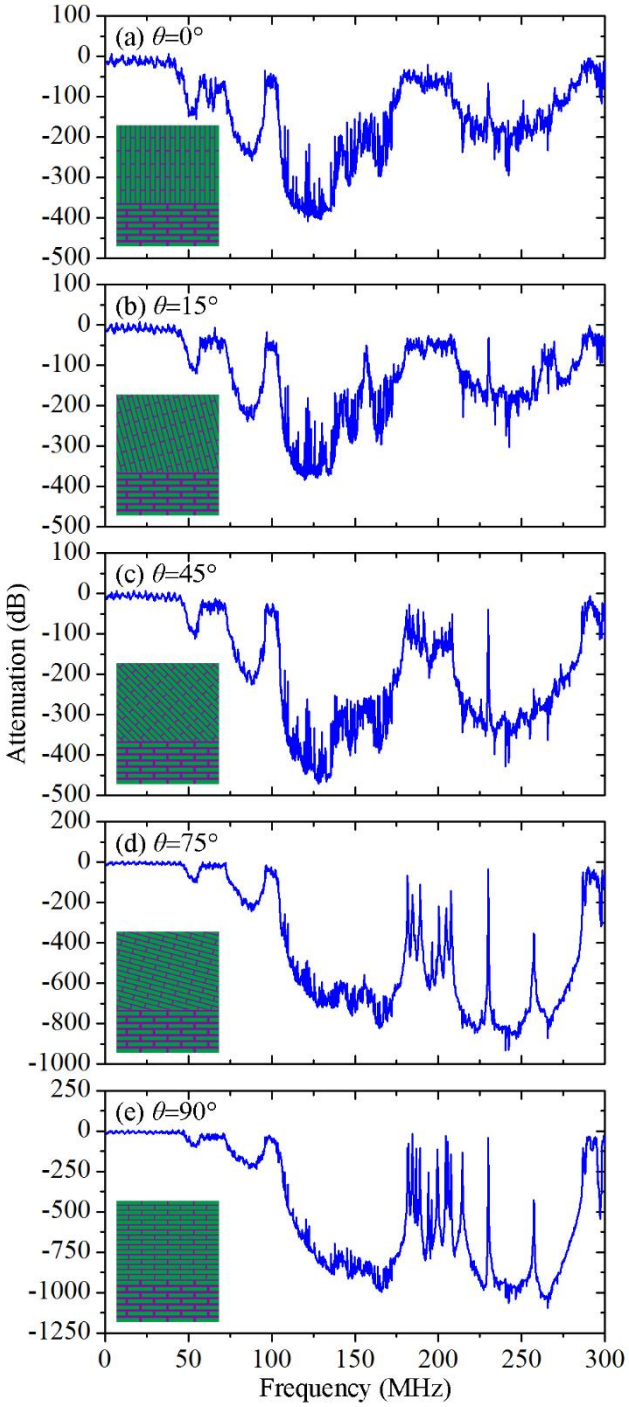

Figure 4.18 Effect of mineral platelet orientation in the upper layer on the wave attenuation. (a) θ=0 °, (b) θ=15 °, (c) θ=45 °, (d) θ=75 °, and (e) θ=90 °. The mineral platelets in the upper layered

are rotated by θ in the counterclockwise direction. The volume fractions of mineral platelets in the lower layer and upper layer are set to 0.7 and 0.9, respectively.

Next, the effect of local mineral platelet concentration of the proposed heterogeneous composites on the wave attenuation capability will be explored. The mineral platelet concentration in the lower layer is varied from 0.50 to 0.90, while that in upper layer remains 0.90. Figure 4.19 shows the effect of mineral platelet concentration in the lower layer on the wave attenuation capability. When the volume fraction is increased from 0.50 to 0.70, the bandwidths of the attenuation zones stay the same. However, the attenuation zones below 96 MHz tend to gradually disappear when the volume fraction is increased to 0.80 and 0.90. This is because the attenuation zones of the lower layer tend to shift towards higher frequency ranges and to mostly overlap with those in the upper layer when the mineral platelet concentration in the lower layer is increased to that in the upper layer. This finding suggests that a contrast between mineral platelet concentrations of the two constituent layers is essential to maintain the broadband wave attenuation capability.

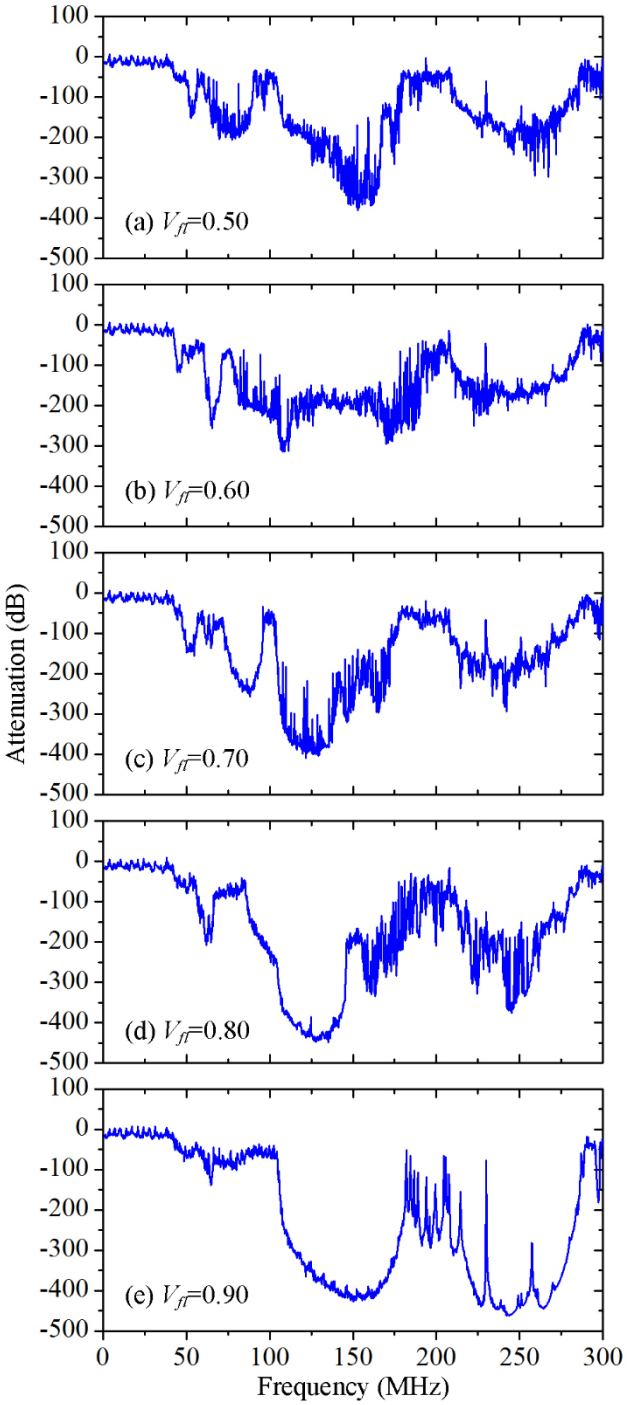

Figure 4.19 Effect of mineral platelet concentration in the lower layer (V_{fl}) on the wave attenuation. (a)V_{fl}=0.50, (b) V_{fl}=0.60, (c) V_{fl}=0.70, (d) V_{fl}=0.80, and (e) V_{fl}=0.90. The volume fraction of mineral platelets in the upper layer is set to 0.90.

4.4.5 Discussion

The existence and robustness of broadband wave attenuation capability have been demonstrated in the bio-inspired heterogeneous composites. It is shown that the broadband attenuation zones in the heterogeneous composites are achieved by directly superimposing the attenuation zones in each constituent layer. It should be pointed out that the constituent layers of the proposed heterogeneous composites in this work are bases on the biological structural composites with high mechanical performance. The stiffness and strength contour maps of the constituent layers as a function of the aspect ratio and the volume fraction of mineral platelets were plotted in Figure 4.20. Note that each constituent layer of the proposed heterogeneous architecture has considerable stiffness and strength. In addition, the bio-inspired heterogeneous architecture with mineral platelets oriented out-of-plane in the upper layer and in-plane in the lower layer enables the unusual combination of hardness, flexural modulus, and fracture toughness. [46-48, 50, 52, 111-113] However, a systemic investigation into the mechanical properties of the composite architecture is beyond the scope of this study. The broadband vibration mitigation capability combining the notable mechanical performance of the proposed heterogeneous architecture makes it particularly suitable for vibration mitigation and impact resistance in hostile environments, such as for deep water applications.

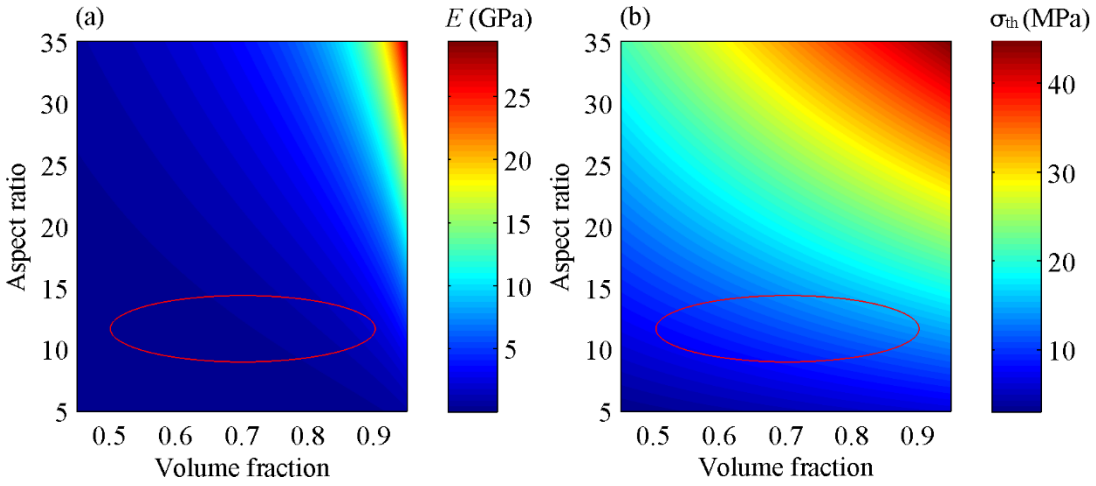

Figure 4.20 Mechanical properties of the proposed heterogeneous composite. (a) Stiffness (E) and (b) strength (σ_{th}) contour maps of each constituent layer of the proposed heterogeneous composite. The stiffness and strength as a function of aspect ratio and volume fraction of mineral platelets are predicted by the shear lag model. [41, 102] The regions surrounded by the red ellipses in (a) and (b) indicate the stiffness and strength of the constituent layers of the proposed heterogeneous composites, respectively.

In general, a few approaches have been proposed to improve the wave attenuation capability of composite materials, including topological optimization, [88] introduction of fractal microstructures, [114] and external mechanical loading. [89, 115]. In this study, however, broadband attenuation zones are achieved by simply stacking two layers mimicking the heterogeneous architectures of structural biological materials. This flexible approach also endows the proposed heterogeneous composites with mechanical performance as compared to those achieved by other approaches. It should be pointed out that improved wave attenuation capability and enhanced mechanical properties can be simultaneously achieved by introducing multilevel structural hierarchies in one-dimensional layered composites. [27] However, the resulting broadband attenuation zones are undermined and do not directly result from the superposition of

those in each structural level, because the moduli are reduced and the structural periodicities are interrupted at higher levels. This phenomenon is more prominent in two-dimensional multilevel hierarchical composites.

It is revealed that the attenuation zones in the proposed heterogeneous composites are attributed to Bragg scattering and/or local resonances. Besides dictating the band gaps of the heterogeneous composites, these physical mechanisms also contribute to the outstanding mechanical properties of structural biological composites. [116] Hypothetically, the multiple scattering and localization of elastic wave can control the interaction of elastic energy among locally high-stress regions. As a result, more elastic energy will be dissipated by the soft organic matrix, and hence enhanced fracture toughness can be achieved. To some extent, this further supports our claim that broadband vibration mitigation and enhanced mechanical performance can be simultaneously achieved in the proposed heterogeneous composites. It should be noted that the material properties of the constituents, such as Young's modulus and Poisson's ratio, can have a great impact on the size of band gaps. [86] Therefore these parameters can be further utilized to tune the band gaps.

It is also shown that the original broadband attenuation zones will be maintained and additional attenuation zones will arise when the mineral platelet orientation in the upper layer is rationally manipulated. Importantly, a contrast between mineral platelet concentrations of each constituent layer is essential to generate broadband vibration mitigation. Indeed, manipulating local characteristics of heterogeneous architectures to handle externally mechanical challenges is prevalent in structural biological composites. For example, synthetic composites with locally tunable orientation and concentration of reinforcements have been recently reported. By coating the reinforcements with a minimal concentration of superparamagnetic nanoparticles, the

orientation and concentration of the coated reinforcements can be remotely controlled using an ultralow magnetic field. [46, 117, 118] These progress provide a flexible approach to precisely tailor the local characteristics of the proposed heterogeneous architecture, suggesting the possibility to design optimal multifunctional composites with improved wave attenuation capability and mechanical performance simultaneously.

4.5 Conclusions

In summary, the effects of hierarchy and heterogeneity of bioinspired architected metamaterials on the vibration mitigation have systematically investigated in this Chapter. Multiple band gaps and passbands arise in the proposed hierarchical composites with two levels of hierarchy. Remarkably, the low-frequency band gaps, akin to the subwavelength characteristic of acoustic metamaterials, are attributed to the periodic arrangement of mineral and organic phases at the second hierarchical level. By contrast, the band gaps and passbands in high-frequency ranges correspond to the waveguide modes, enabling the incident wave can be either well trapped inside the waveguides or efficiently transmit through the waveguides. These features enable the design of compact and lightweight wave filters and waveguides operating in an ultrawide frequency range. Notably, the hierarchical architectures with multilevel structural hierarchies also endow the proposed composites with enhanced strength and toughness, which are highly desirable for phononic crystals under mechanically challenging environmental conditions. The findings in this chapter not only provide us a better understanding of the mechanisms accounting for the multiband features of bio-inspired hierarchical composites but also offer new opportunities towards the design of compact and mechanically robust phononic crystals with capabilities to effectively manipulate wave propagation.

It is also reported broadband vibration mitigation capability in the bio-inspired heterogeneous composites that are based on the biological structural composites with high mechanical performance. Broadband wave attenuation capability is achieved by directly superimposing the attenuation zones in each constituent layer. Physical mechanisms, including Bragg scattering and local resonances responsible for the attenuation zones, have been identified by studying the phonon dispersion relation of each layer. The investigation into the effect of local characteristics of the heterogeneous composites on attenuation capability indicates that the broadband wave attenuation capability will be maintained, if a contrast between mineral platelet concentrations exists. The current study not only provides a better understanding of the dynamic response of bio-inspired heterogeneous composites but also opens new avenues to design optimal multifunctional composites for broadband vibration mitigation and impact resistance under mechanically challenging environmental conditions.

CHAPTER 5. LIGHTWEIGHT YET STIFF LATTICE METAMATERIALS FOR BROADBAND AND MULTIBAND VIBRATION CONTROL

5.1 Introduction

In previous Chapters, it has been demonstrated that broad and multiple phononic band gaps can be achieved 3D and 2D architected composites. Importantly, these architected composites also have excellent mechanical performance, including high strength, stiffness, and energy absorption. These unusual mechanical performances and vibration mitigation capability make the architected composites particularly useful in mechanically challenging environmental conditions. However, in aerospace engineering, lightweight is another important criteria that limit the applications of conventional materials. In this regard, lattice materials with different coordinate numbers, such as hexagonal lattice, kagome lattice, and triangular lattice, have been widely deployed due to their lightweight, novel thermomechanical properties, and energy absorption capability. In this Chapter, a new type of lattice materials will be proposed, where lightweight, vibration mitigation, and excellent mechanical performance can be simultaneously achieved.

The structural hierarchy has been employed as an important strategy to explore improved mechanical properties and other unusual physical properties. Typical examples range from Eiffel tower to hierarchically architected nano truss with multiple length scales. [54-56] Recent studies show that it is possible to manipulate wave propagation by harnessing multiscale characteristic of hierarchical architectures. [27, 57, 58] These rationally designed hierarchical architectures can give rise to multiple and broadband phononic band gaps as well as low-frequency band gaps. In

addition, these hierarchical architectures also enable the coexisting of multiband wave filtering and waveguiding in an ultrawide frequency range. [119]

Despite these considerable efforts, challenges remain. For example, to achieve the desired wave attenuation, soft materials using thermally coupled dissipation mechanism are often employed in engineering practice. As a result, the wave attenuation capability strongly depends on the thickness of the materials, thus posing a great challenge to design lightweight and stiff materials with strong wave attenuation ability. Furthermore, conventional phononic crystals with periodic architectures can only provide limited frequency band gaps since the Bragg interference requires that the wavelength must be comparable to the given structural periodicity. To overcome the bandwidth limitation, numerical approaches such as topology optimization have been developed to maximize the band gap size. [120, 121] It is worth noting that the objective function of this approach is to maximize a single band gap size, and the resultant architectures are still spatially periodic. Lightweight and stiff phononic crystals with broadband and multiband wave attenuation ability remain unrealized.

Recently, inspired by the observation that many biological materials have developed multilevel of structural hierarchy enabling the combination of unusual mechanical properties to protect against environmental threats, researchers have introduced structural hierarchy into the conventional lattice materials. [122-127] For example, by replacing the cell walls of regular honeycombs with kagome and triangular lattices, it is theoretically demonstrated that the stiffness of the hierarchical honeycombs is increased by about two orders of magnitude as compared to that of regular honeycombs. [125]

Here, a hierarchical metamaterial design concept will be proposed, aiming at addressing the conflicts between lightweight, mechanical performance, and vibration mitigation. The vibration mitigation and mechanical response of the hierarchical honeycombs will be investigated using the finite element method. The introduction of structural hierarchy in regular honeycombs gives rise to multiple and broad phononic band gaps. More important, the proposed hierarchical honeycombs also exhibit enhanced mechanical properties, thereby providing opportunities to design architected materials with simultaneous improvement in lightweight, vibration mitigation, and load-carrying capacity.

5.2 Characterization of the hierarchical honeycombs

The proposed hierarchical architectures are constructed by replacing the cell walls of the regular honeycombs with hexagonal, kagome, and triangular lattices, respectively (referred to as hexagonal, kagome, and triangular hierarchical honeycombs for simplicity in the following, Figure 5.1 (a)-(e)). For the purpose of fair comparison, kagome, and triangular hierarchical honeycombs are subsequently obtained by connecting the midpoints and vertices of the hexagonal lattice, respectively. The proposed hexagonal hierarchical honeycombs are characterized by two geometric parameters, hierarchical length ratio, $\gamma = l_h/l_0$, and the number of hexagonal lattices away from the central axis, *N*, where l_0 and l_h are the lengths of cell walls of regular honeycomb and hexagonal lattice, respectively (Figure 5.1). The length and thickness of the hexagonal, kagome and triangular lattices are determined by mass equivalence between regular honeycombs and hierarchical honeycombs. For hexagonal hierarchical honeycombs, the mass equivalence gives

$$t_0 l_0 - \frac{t_0^2}{2\sqrt{3}} = 3P\left(t_h l_h - \frac{t_h^2}{2\sqrt{3}} \right) \tag{5.1}$$

where t_0 and t_h are the cell wall thickness of regular honeycomb and hexagonal lattice, respectively; P is the number of a hexagonal lattice with one-half thickness and is determined by γ and N.

As a result, the thickness and length of the hexagonal lattice can be calculated as

$$\frac{t_h}{l_h}=\sqrt{3}\left(1-\sqrt{1-\frac{2}{3\sqrt{3}P\gamma^2}\left[\frac{t_0}{l_0}-\frac{1}{2\sqrt{3}}\left(\frac{t_0}{l_0}\right)^2\right]}\right) \tag{5.2}$$

Similarly, the thickness and length of kagome lattice and triangular lattice are given by

$$\frac{t_k}{l_k}=\frac{\sqrt{3}}{2}\left(1-\sqrt{1-\frac{16}{3\sqrt{3}Q\gamma^2}\left[\frac{t_0}{l_0}-\frac{1}{2\sqrt{3}}\left(\frac{t_0}{l_0}\right)^2\right]}\right) \tag{5.3}$$

$$\frac{t_t}{l_t}=\frac{1}{\sqrt{3}}\left(1-\sqrt{1-\frac{4\sqrt{3}}{3R\gamma^2}\left[\frac{t_0}{l_0}-\frac{1}{2\sqrt{3}}\left(\frac{t_0}{l_0}\right)^2\right]}\right) \tag{5.4}$$

where t_k and l_k are the thickness and length of cell walls of kagome lattice; t_t and l_t are the thickness and length of cell walls of a triangular lattice, respectively; Q and R are the numbers of kagome and triangular lattices, respectively.

The composition of the regular honeycombs and hierarchical honeycombs is a glassy polymer, SU-8, whose properties are characterized by Young's modulus E_s=3.3 GPa, Poisson's ratio ν=0.33, a yield stress σ_y=105 MPa, and density ρ_s=1200 kg/m^3. [71]

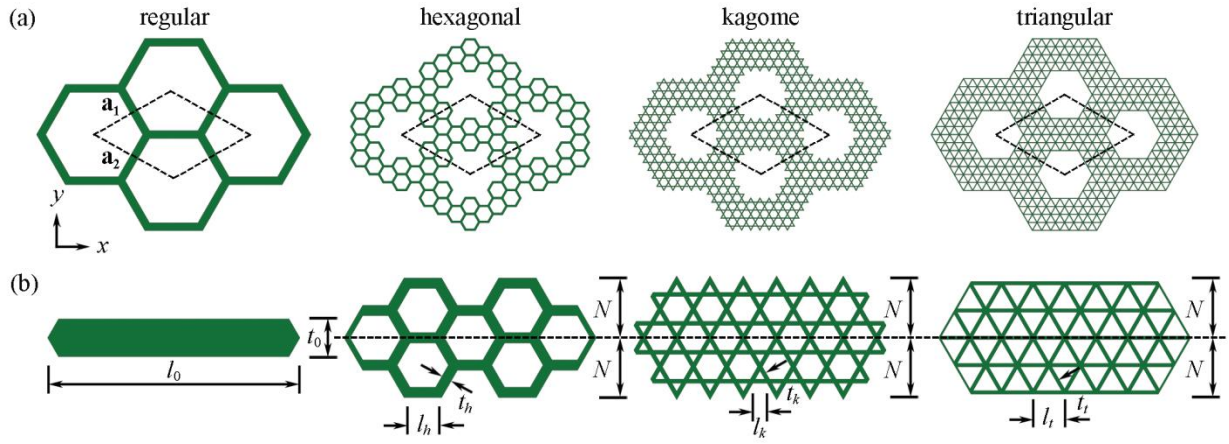

Figure 5.1 Schematics of the proposed hierarchical honeycombs. (a) Regular honeycomb and hierarchical honeycombs. Here $\mathbf{a}_1=(3l_0/2, \sqrt{3}l_0/2)$, $\mathbf{a}_2=(3l_0/2, -\sqrt{3}l_0/2)$ are lattice constants; l_0 and t_0 are the length and thickness of cell walls. The dash lines indicate the supercells; (b) schematics of cell walls of regular honeycombs hexagonal, kagome, and triangular hierarchical honeycombs, respectively.

5.3 Numerical modeling

5.3.1 Bloch wave analysis for infinite periodic structures

5.3.1.1 Calculation of the Brillouin zone

The unit cells of the proposed hierarchical architectures can be described by two lattice vectors, $\mathbf{a}_1=(3l_0/2, \sqrt{3}l_0/2)$, $\mathbf{a}_2=(3l_0/2, -\sqrt{3}l_0/2)$ (Figure 5.2 (a)). Then the reciprocal lattice primitive vectors can be calculated as

$$\mathbf{b}_1 = 2\pi \frac{\mathbf{a}_2 \times \hat{\mathbf{z}}}{\mathbf{a}_1 \cdot (\mathbf{a}_2 \times \hat{\mathbf{z}})}$$

$$\mathbf{b}_2 = 2\pi \frac{\hat{\mathbf{z}} \times \mathbf{a}_1}{\mathbf{a}_1 \cdot (\mathbf{a}_2 \times \hat{\mathbf{z}})} \tag{5.5}$$

By connecting the perpendicular bisectors of the reciprocal lattice, the corresponding Brillouin zone can be constructed (Figure 5.2 (b)). [59] Due to the presence of the rotation and mirror symmetries of the unit cells, the first irreducible Brillouin zone (shaded gray polygon) is considered in the phononic dispersion relations simulation.

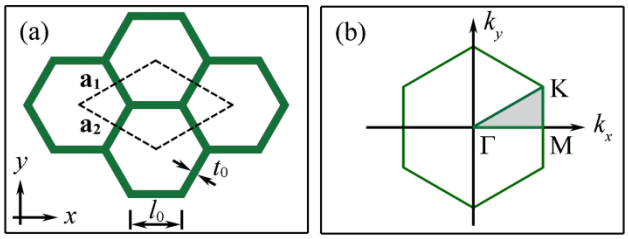

Figure 5.2 The first irreducible Brillouin zone for hierarchical honeycombs. (a) Regular honeycomb. Here $\mathbf{a}_1=(3l_0/2, \sqrt{3}l_0/2)$, $\mathbf{a}_2=(3l_0/2, -\sqrt{3}l_0/2)$ are lattice constants; l_0 and t_0 are the length and thickness of cell walls. (b) The associated first Brillouin zone, where $\mathbf{\Gamma}= (0, 0)$, $\mathbf{M}= (2\pi/3l_0, 0)$, and $\mathbf{K}= (2\pi/3l_0, 2\sqrt{3}\pi/9l_0)$.

5.3.1.2 Calculation of phononic dispersion relations

Details concerning the modeling of phononic dispersion relations and wave transmission can be found in Chapter 2.

5.3.2 Micromechanical modeling of periodic structures

5.3.2.1 Material behavior of SU-8

The material properties of SU-8 were determined from the experimentally obtained uniaxial stress-strain relation. [128] The measured stress-strain behavior is shown in Figure 5.3. The properties of SU-8 are characterized by Young's modulus E_s=3.3 GPa, Poisson's ratio ν=0.33, a yield stress

σ_y =105 MPa, and density ρ_s=1200 kg/m^3. The true stress-true strain relation is implemented as the constitutive equation for the mechanical behavior simulations.

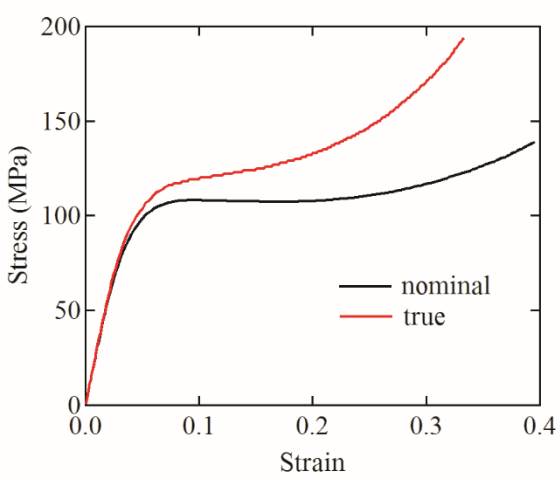

Figure 5.3 Measured stress-strain relation of SU-8. The strain rate is 0.01/s.

5.3.2.2 Implementation of periodic boundary conditions

To study the mechanical response of periodic structures, as long as no microscopic bifurcation happens, modeling on a smallest repeating representative volume element (RVE) together with periodic boundary conditions is computationally efficient. When the RVE is subjected to a macroscopic deformation gradient, **F**, periodic boundary conditions are applied on the sides of RVE such that [129, 130]

$$\mathbf{u}(B)-\mathbf{u}(A)=(\mathbf{F}-\mathbf{I})\{\mathbf{X}(B)-\mathbf{X}(A)\}=\mathbf{H}\{\mathbf{X}(B)-\mathbf{X}(A)\}, \tag{5.6}$$

where *A* and *B* are two points periodically located on the two sides of the RVE; **u** denotes displacement, **X** denotes the position in reference configuration, **F** is the deformation gradient tensor, and **H**=**F**-**I** is the macroscopic displacement gradient tensor (Figure 5.4). Note that for the plane strain problem in this work, the displacement gradient is reduced to a 2×2 matrix

$$\mathbf{H}=\begin{bmatrix} H_{11} & H_{12} \\ H_{21} & H_{22} \end{bmatrix}=\begin{bmatrix} F_{11}-1 & F_{12} \\ F_{21} & F_{22}-1 \end{bmatrix}. \tag{5.7}$$

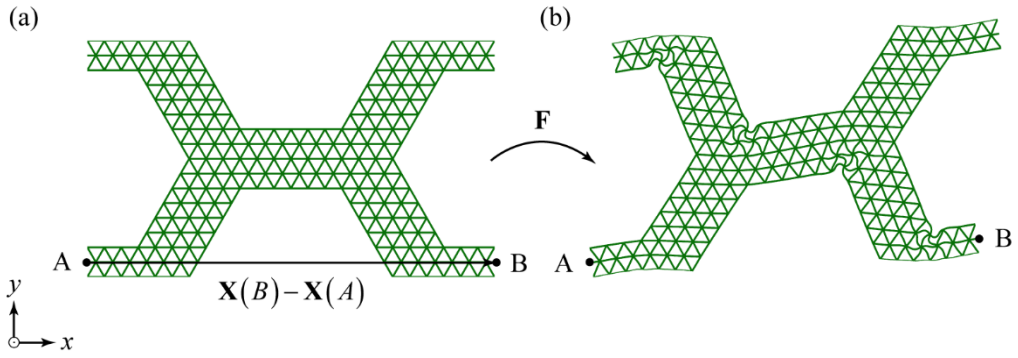

Figure 5.4 Schematic illustration of periodic boundary conditions on the representative volume element of the triangular hierarchical honeycomb. (a) Undeformed and (b) deformed states. Here *A* and *B* are two points periodically located on the two sides of the RVE.

To evaluate the macroscopic mechanical response of the hierarchical honeycombs, we use the principle of virtual work,

$$\delta W^{\text{int}}=\delta W^{\text{ext}}, \tag{5.8}$$

The external virtual work, δW^{ext}, can be written as

$$\delta W^{\text{ext}}=\int_{S_0}\mathbf{P}(\mathbf{X})\mathbf{n}_0\cdot\delta\mathbf{u}(\mathbf{X})\,dS_0=\int_{S_0}\mathbf{t}_0(\mathbf{X})\cdot\delta\mathbf{u}(\mathbf{X})\,dS_0, \tag{5.9}$$

where **P** is the local first Piola-Kirchhoff stress tensor, $\mathbf{n}_0$ is the outward unit vector normal to the surface area, S_0, in the reference configuration. $\delta\mathbf{u}$ and $\mathbf{t}_0$ are the virtual displacement and surface traction in the reference configuration, respectively. The macroscopic first Piola-Kirchhoff stress, $\bar{\mathbf{P}}$, can be calculated as

$$\bar{\mathbf{P}}=\frac{1}{V_0}\int_{V_0}\mathbf{P}(\mathbf{X})\,dV_0, \tag{5.10}$$

where V_0 is the volume of the representative volume element in the reference configuration.

The internal virtual work, δW^{int}, is given by

$$\delta W^{\text{int}} = \int_{V_0} \mathbf{P}(\mathbf{X}) \cdot \delta \mathbf{F}(\mathbf{X}) dV_0 = V_0 \bar{\mathbf{P}} \cdot \delta \mathbf{F}, \tag{5.11}$$

Combining equation (5.8), (5.9), and (5.11), we have

$$V \bar{\mathbf{P}} \cdot \delta \mathbf{F} = \int_{S_0} \mathbf{t}_0(\mathbf{X}) \cdot \delta \mathbf{u}(\mathbf{X}) dS_0, \tag{5.12}$$

As a result, the macroscopic first Piola-Kirchhoff stress is a function of surface traction.

In finite element implementation, the components of **F** assigned to the RVE model by introducing two reference nodes with four generalized degrees of freedom, ξ_i ,

$$\begin{bmatrix} \xi_1 & \xi_2 \\ \xi_3 & \xi_4 \end{bmatrix} = \begin{bmatrix} F_{11} - 1 & F_{12} \\ F_{21} - 1 & F_{22} - 1 \end{bmatrix}, \tag{5.13}$$

Then the external virtual work can be restated as

$$\delta W^{\text{ext}} = \sum_{i=1}^{4} \Xi_i \delta \xi_i, \tag{5.14}$$

where Ξ_i are the reaction forces associated with the assigned displacement ξ_i. By using equation (5.11) and (5.14), macroscopic first Piola-Kirchhoff stress can be identified as

$$\begin{bmatrix} \bar{P}_{11} & \bar{P}_{12} \\ \bar{P}_{21} & \bar{P}_{22} \end{bmatrix} = \frac{1}{V_0} \begin{bmatrix} \Xi_1 & \Xi_2 \\ \Xi_3 & \Xi_4 \end{bmatrix}. \tag{5.15}$$

Note that in all of the mechanical simulations, 4-node bilinear plane strain quadrilateral elements are adopted and mesh size effect has been studied to ensure the better convergence.

5.4 Results and discussion

5.4.1 Broadband and multiband features

We start by examining the phononic dispersion relations of hierarchical honeycombs with γ=1/5, N=1, and relative density ρ/ρ_s=0.06. For the purpose of comparison, phononic dispersion relation

of the associated regular honeycomb is also reported. For the regular honeycomb, we only observe one narrow band gap at ϖ=0.059-0.061 (Figure 5.5 (a)). By contrast, the introduction of structural hierarchy in the regular honeycombs leads to much broader band gaps (Figure 5.5 (b)-(d)). Specifically, the maximum band gaps in hexagonal, kagome, and triangular hierarchical honeycombs are ϖ=0.047-0.079, ϖ=0.108-0.133, and ϖ=0.064-0.078, respectively. In addition, the introduction of structural hierarchy also gives rise to multiple band gaps, as shown in the phononic dispersion relations. To gain a deeper understanding, we plot the eigenmodes of the high-symmetry points $\bar{\Gamma}$, $\bar{M}$, and $\bar{K}$ at the lower band edges of the band gaps (Red lines in Figure 5.5). For hexagonal and kagome hierarchical honeycombs, the vibrational modes of the high-symmetry points exhibit a global nature, indicating a Bragg-type band gap. Interestingly, localized vibrational modes are observed for the triangular hierarchical honeycombs, suggesting that local resonances are responsible for the broad band gaps. [22-24, 78] This is also supported by the flat band edge of the band gaps. A direct comparison between the geometric features of the regular honeycomb and hierarchical honeycombs leads us to believe that different mechanisms of band gaps formation are intrinsically dictated by the slenderness ratio and coordination number of the lattice. It should be pointed out that damping effect resulting from the viscoelastic feature of the glassy polymer may contribute to the wave attenuation. [131] However, recent experimental results indicate that the damping effect will not swamp the band gaps in the phononic dispersion relations. [132]

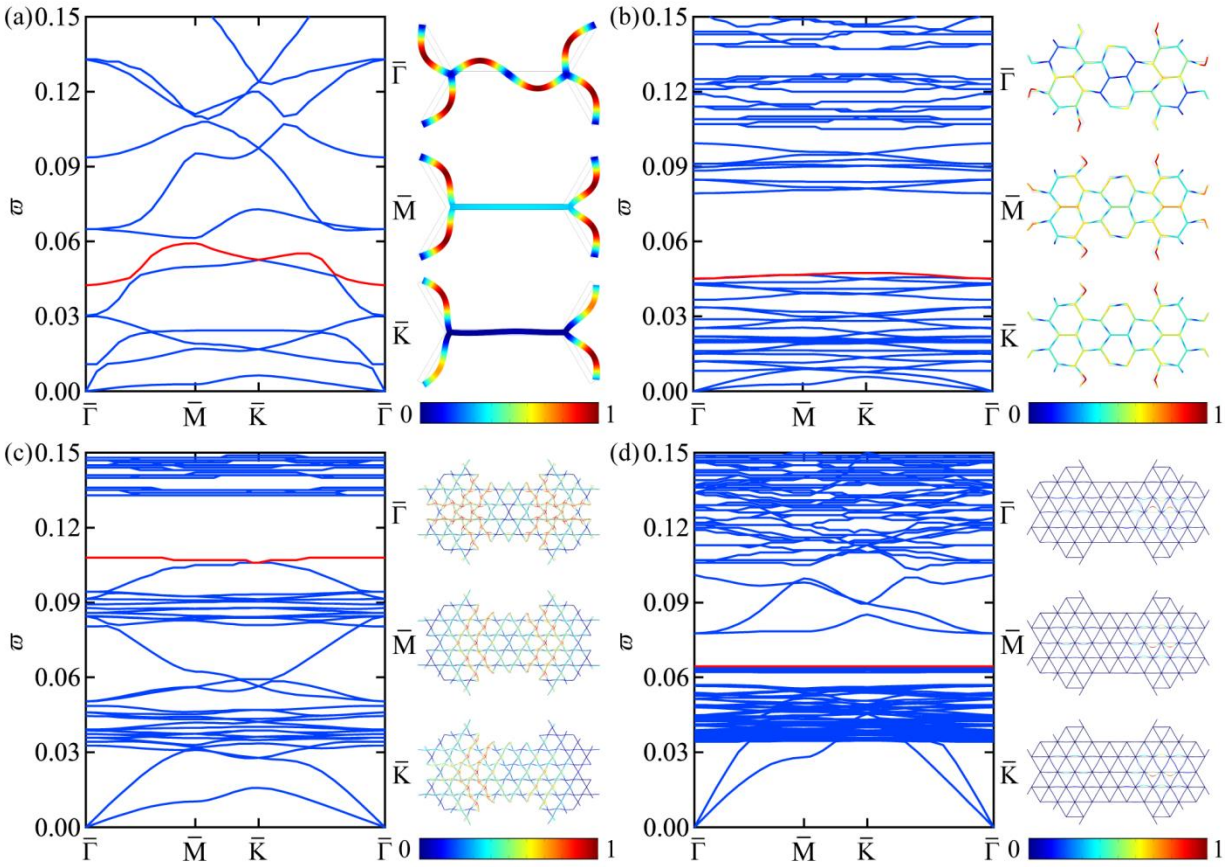

Figure 5.5 Phonon dispersion relations of regular and hierarchical honeycombs. (a) Regular honeycomb; (b)-(d) hexagonal, kagome, and triangular hierarchical honeycombs, respectively. Eigenmodes of the high-symmetry points $\bar{\Gamma}$, $\bar{\mathrm{M}}$, and $\bar{\mathrm{K}}$ at the lower band edges of the band gaps are also plotted. Here $\bar{\Gamma}$ = (0, 0), $\bar{\mathrm{M}}$ = ($2\pi/3l_0$, 0), and $\bar{\mathrm{K}}$ = ($2\pi/3l_0$, $2\sqrt{3}\pi/9l_0$). The normalized frequency is defined as $\varpi = \omega a/2\pi c_t$, where ω is frequency, a is the length of lattice constant, c_t is the transverse wave velocity of the constituent material. The legends indicate the amplitude of normalized displacement. Here γ=1/5, N=1, and relative density ρ/ρ_s=0.06.

Having demonstrated that the broadband and multiple band gaps are dictated by the slenderness ratio and coordination number, we now examine effects of two geometric parameters, γ and N, on the evolution of band gaps. Note that for a given relative density and a type of hierarchical

honeycomb, the slenderness ratio of the lattice is uniquely controlled by γ and *N*. Here we consider the case that the relative density ρ/ρ_s=0.16 for the hierarchical honeycombs to ensure that the cell walls of each lattice have considerable thickness at large *N*. To quantitatively evaluate the wave attenuation capability of the hierarchical honeycombs, we define two indicators to consider the broadband and multiband features: maximum relative band gaps, $(\Delta\omega/\omega_*)_{\max}$ and total relative band gaps, $\sum(\Delta\omega/\omega_*)$, where $\Delta\omega$ is band gap width and ω_* is the midgap frequency. As shown in Figure 5.6, both the maximum band gaps and total band gaps tend to diminish for $N>2$. On one hand, for a given relative density, larger *N* indicates more substructures and larger slenderness ratio. While for wave propagation in lattice structures, slenderness ratio is critical to the band gaps formation. [133] On the other hand, with the increase of *N*, the effect of structural hierarchy becomes weaker. At the maximum *N*, all hierarchical structures reduce into regular lattice materials, which don't have or only have small band gaps, depending on the slenderness ratio and node connectivity. [133, 134] For a given $N \le 2$, the maximum band gaps and total band gaps tend to decrease when the hierarchical length ratio decreases from 1/2 to 1/11. The maximum band gaps and total band gaps of regular honeycombs are also plotted in Figure 5.6 for the purpose of comparison (γ=1). We observe that hierarchical honeycombs with γ=1/2 exhibit comparable or larger maximum band gaps, whereas the total band gaps strongly depend on the shape of the lattice when compared with that of the regular honeycomb. These quantitative analyses not only support our conclusion concerning the mechanisms underlying the band gap formation but also provide clues to design phononic crystals with desired wave attenuation capability.

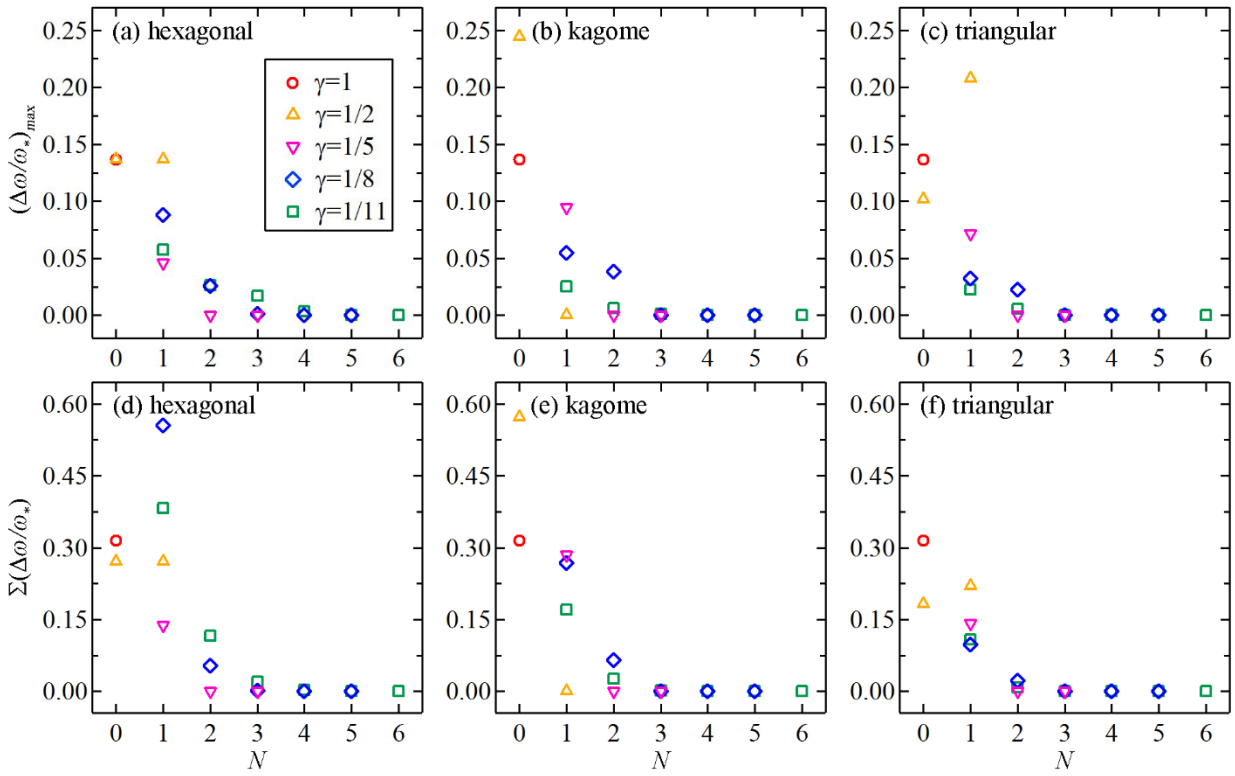

Figure 5.6 Effects of hierarchical length ratio and number of lattice on the evolution of maximum band gaps and total band gaps. (a)-(c) Maximum band gaps in hexagonal, kagome, and triangular hierarchical honeycombs, respectively; (d)-(f) total band gaps in hexagonal, kagome, and triangular hierarchical honeycombs, respectively. $\Delta\omega$ is band gap width and ω_* is the midgap frequency. Here the relative density is ρ/ρ_s =0.16.

To demonstrate the potential of designing lightweight phononic crystals, a quantitative investigation is carried out to examine the effect of relative density on the band gap evolution (Figure 5.7). Here we choose γ =1/5 and N=1, and ρ/ρ_s =0.06~0.32. Noticeably, both the maximum band gaps and total band gaps are inversely proportional to the relative density. For the maximum band gaps, hierarchical honeycombs show much smaller exponents than that of regular honeycombs, indicating that hierarchical honeycombs can be potentially designed with light

weight. For the total band gaps, we note that hexagonal and triangular hierarchical honeycombs exhibit smaller exponents. Although the exponent of kagome hierarchical honeycomb is larger than that of regular honeycomb, an inverse relation between total band gaps and relative density still can be observed.

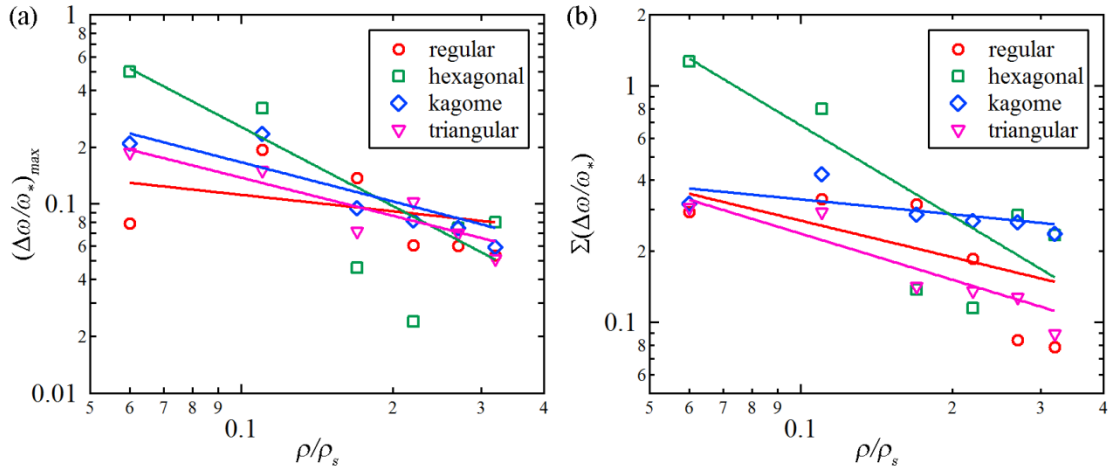

Figure 5.7 Effects of relative density on maximum band gaps and total band gaps. (a) Maximum band gaps and (b) total band gaps of regular and hierarchical honeycombs. Here γ=1/5 and N=1. The solid lines represent the numerical data fitting using scaling law.

5.4.2 Enhanced mechanical properties of hierarchical honeycombs

It has been demonstrated that hierarchal honeycombs can have improved mechanical properties. To further explore the possibility to design phononic crystals with relatively high stiffness, we numerically examine the mechanical response of the proposed hierarchical honeycombs under uniaxial compression. A constitutive stress-strain behavior of the glassy polymer SU-8 together with a periodic representative volume element of each regular and hierarchical honeycomb is employed to predict the mechanical response. [71, 128]

Figure 5.8 (a) reports the mechanical response of the hierarchical honeycombs with γ=1/5 and N =1, and ρ/ρ_s =0.06 under uniaxial compression up to 10% macroscopic strain. For the regular honeycomb, we observe a typical stress-strain relation including an initial linearly elastic regime and a following non-linear trend induced by plastic deformation. As compared to the regular honeycomb, hexagonal hierarchical honeycomb exhibits a very similar response, but a slightly lower stress-strain curve, indicating a comparable stiffness. For kagome and triangular hierarchical honeycombs, the stress increases rapidly with the strain followed by higher yield/buckling stress, indicating much higher stiffness. The highly nonlinear behavior of hierarchical honeycombs is dictated by local buckling of the cell walls together with the plastic deformation of SU-8. Importantly, these deformation mechanisms will endow hierarchical honeycombs with enhanced energy absorption capacity. It should be emphasized that hierarchical honeycombs can be constructed by replacing each vertex of regular honeycombs with a smaller self-similar hexagon. [135] In this case, broad and multiple band gaps can be retained, the stiffness, however, will be significantly sacrificed.

Figure 5. 8 (b) shows the stiffness of the hierarchical honeycombs at relative density range ρ/ρ_s =0.06~0.32. For the regular honeycombs, the simulated stiffness agrees well with predictions from linear elastic theory, [136] indicating that our numerical framework can accurately predict the mechanical response of the regular honeycombs. Hexagonal hierarchical honeycombs have comparable yet slightly lower stiffness than that of regular honeycomb. Notably, kagome and triangular hierarchical honeycombs show significantly improved stiffness. For example, at a low relative density (ρ/ρ_s=0.06), kagome and triangular hierarchical honeycombs exhibit an improved stiffness by nearly one and two orders of magnitude as compared to the regular honeycomb and the hexagonal hierarchical honeycomb, respectively. We fit the stiffness as a function of relative

density using a scaling law, $E_h/E_s = C(\rho/\rho_s)^n$, where E_h and E_s are the stiffness of hierarchical honeycombs and solid constituent material SU-8, respectively, C is geometry-dependent proportionality constant, and n is the scaling exponent. As a result, the scaling exponents for regular honeycomb, hexagonal, kagome, and triangular hierarchical honeycombs are 2.97, 2.69, 1.70, and 1.13, respectively, indicating that regular honeycomb and the hexagonal hierarchical honeycomb exhibit a bending-dominated deformation behavior, whereas kagome and triangular hierarchical honeycombs have a stretching-dominated deformation behavior. Intrinsically, the discrepancy between the bending-dominated and stretching-dominated behavior is governed by the geometric features of the lattice, i.e., slenderness ratio and coordinate numbers.

5.4.3 Design stiff and lightweight phononic crystals

By combing the simulated stiffness and band gaps of the hierarchical honeycombs with different relative densities, we obtain the Ashby-type plots of specific modulus versus maximum band gaps and total band gaps, as shown in Figure 5.8 (c) and (d), respectively. Compared with the regular honeycombs, hexagonal hierarchical honeycombs retains comparable specific modulus but broader and multiple band gaps. Remarkably, kagome and triangular hierarchical honeycombs can achieve specific stiffness that are 40~60 times higher while having similar maximum band gaps and total band gaps, compared with that of regular honeycombs. From a practical perspective, the proposed hierarchical honeycombs have great potential applications in areas where lightweight, wave attenuation, and load carrying capacity are simultaneously desired.

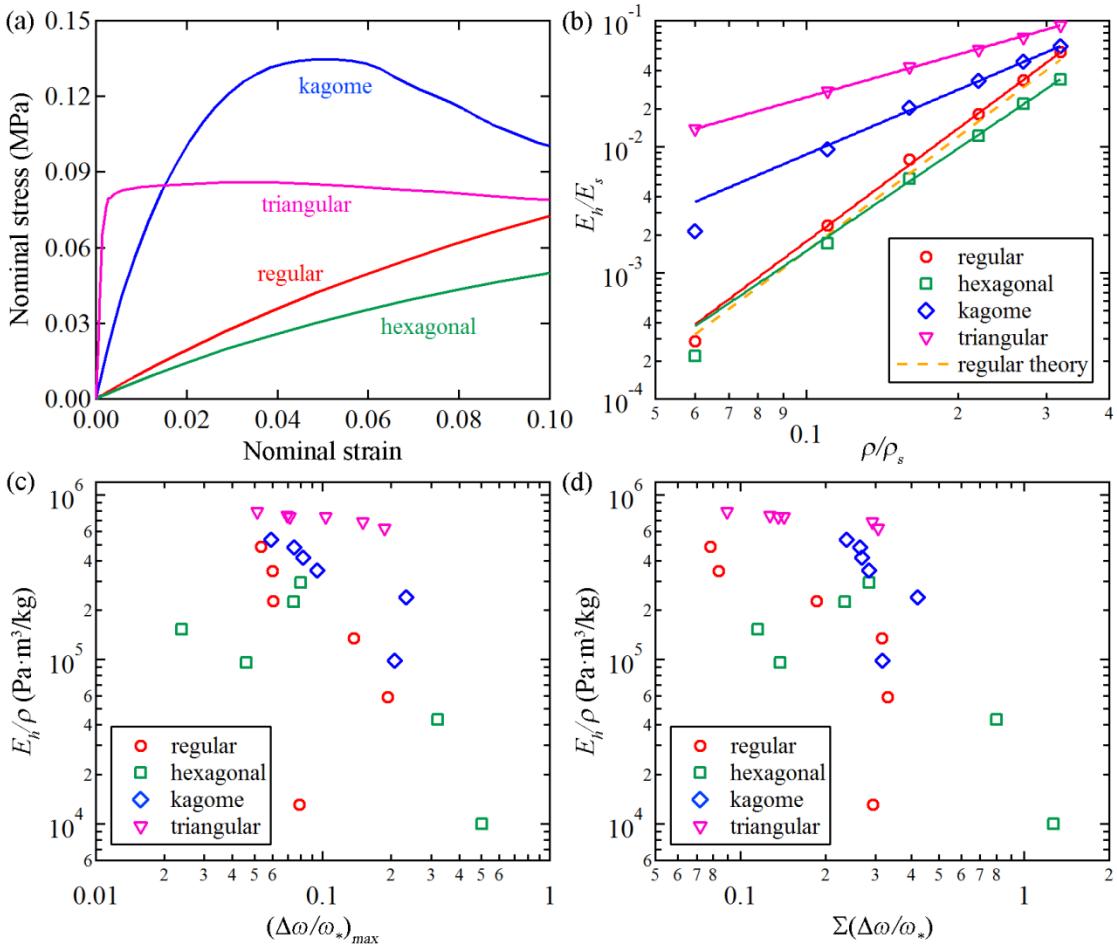

Figure 5.8 Mechanical response of the hierarchical honeycombs and their applications in multifunctional design. (a) Stress-strain relations of regular honeycomb and hierarchical honeycombs compressed along *y* direction; (b) Relations between stiffness and relative density of regular honeycomb and hierarchical honeycombs; (c) and (d): Ashby-type plots of specific modulus and maximum band gaps and total band gaps. E_h and E_s are Young's modulus of hierarchical honeycombs and constituent material SU-8, respectively. Here γ=1/5 and N=1.

5.5 Conclusions

In summary, the numerical analyses in this work provide insights into the effect of structural hierarchy on the wave attenuation and load-carrying capabilities. It has been demonstrated that

broad and multiple band gaps can be achieved in the proposed hierarchical honeycombs, providing that the geometric parameters are rationally selected. In addition, kagome and triangular hierarchical honeycombs exhibit improved specific stiffness compared with regular honeycombs. The achieved outstanding wave attenuation capability and enhanced mechanical properties are attributed to the introduction of the structural hierarchy. Thus the proposed hierarchical honeycombs can be termed a new type of metamaterials. The findings reported here will provide new opportunities to design lightweight and stiff phononic crystals for various applications including underwater wave mitigation in submarines and other structural vibration mitigation in defense, aerospace, and automotive industries.

CHAPTER 6. LATTICE METAMATERIALS WITH MECHANICALLY TUNABLE POISSON'S RATIO FOR VIBRATION CONTROL

6.1 Introduction

We have demonstrated that broadband and multiple band gaps can be achieved in architected composites and lattice metamaterials. These vibration control properties can be readily tuned by tailoring the geometric features, such as volume fraction, to control the vibration in the desired frequency ranges. However, this is impractical in engineering practice once the structures are installed and fixed. One of the possible solutions is to use external stimuli to dynamically tune the band gaps properties. In this chapter, a stretchable lattice metamaterial will be introduced. Broad and mechanically tunable phononic band gaps will be numerically demonstrated.

The proposed lattice materials are built by replacing at the local scale regular straight beams with sinusoidally shaped ones, which are highly stretchable under uniaxial tension. Numerical and experimental results indicate that the proposed lattices exhibit Poisson's ratios varying between -0.7 and 0.5 over large tensile deformations up to 50%. This large variation of Poisson's ratio values is attributed to the deformation pattern switching from bending to stretch within the sinusoidal struts. We also show that the proposed lattice materials exhibit broadband vibration mitigation capability, which can be dynamically tuned by an external mechanical stimulus. Because of these combined unusual properties, the proposed lattice materials show promise for various applications, ranging from tunable particle filters to noise and vibration control.

Metamaterials are rationally designed multiscale material systems whose unusual equivalent physical properties are dictated by their architectures rather than compositions. Metamaterials have

recently attracted significant interest within the research community because of the need to develop various classes of novel properties and broad ranges of potential applications. [63, 137-141] For example, metamaterials with artificially designed architectures can exhibit a negative refractive index that is unattainable for conventional materials. [142-144] The metamaterial concept has been rapidly extended from photonic systems to acoustic, [25, 31, 76, 145] and mechanical systems. [146-151] Among them, mechanical metamaterials having a negative Poisson's ratio (NPR) are of particular interest. [63, 152-157] Most materials (both isotropic and anisotropic) exhibit positive Poisson's ratios, however, the existence of negative Poisson's ratios is still permitted under the tenets of the classic theory of elasticity.

Materials with a negative Poisson's ratio that will contract (expand) transversally when they are axially compressed (stretched) are also called auxetics. [158-166] Auxetic behavior has been observed in a variety of natural systems, including cubic metals, [167] zeolites, [168, 169] natural layered ceramics, [170] silicon dioxides, [171] single-layer graphene, [172, 173] and 2D protein crystals. [174] Following the seminal work of Lakes, [161] a significant body of research work has been established to develop materials with a negative Poisson's ratio. For example, the auxetic behavior of materials provides a wrapping effect around a penetrating object when subjected to indentation, a feature that may be useful in protective and blast engineering applications. [41, 141, 175] Several microstructure architectures and deformation mechanisms have been developed to obtain the auxetic behavior. Between the various architectures, it is worth to note dimpled and perforated elastic sheets, [176] origami/Kirigami-based metamaterials, [152, 177, 178] hierarchical metamaterials with fractal cuts [179] and foams [180-184]. Auxetic materials and structures are intrinsically multifunctional because of the coupling originated between their unusual deformation mechanisms and their multiphysics behavior. For example, piezoresistive

sensors with a NPR substrate demonstrate a 300% improvement in piezoresistive sensitivity, making them capable of multimodal sensing. [184]

Most of the theoretical and experimental investigations related to NPR cellular materials are focused on microstructure configurations with straight ligament topologies. Recent numerical and experimental studies indicate that thin film materials with serpentine microstructures can have improved stretchability, owing to the introduced microstructure and small intrinsic strain in the materials. [185-188] A non-straight (corrugated) rib configuration for open cell polyurethane foams has also recently been considered as a likely explanation for the existence of an unusual blocked shape memory effect in auxetic open cell polyurethane foams. [189] Although it has been theoretically shown that the auxetic behavior can also be attained in hierarchically architected lattice materials with triangular topology, [186] a convincing experimental evidence of the auxetic behavior of these materials has not been reported yet. Moreover, no theoretical and numerical evidence exist about the performance of engineered auxetic metamaterial lattices with sinusoidally (non-straight) ligaments in their microstructure, especially at hierarchical level. The goal of this chapter is to investigate the auxetic behavior and vibration control capability of one of these materials.

6.2 Materials and methods

6.2.1 Description of geometric model

The architected lattice metamaterials were created by replacing the regular straight beams with beams of sinusoidal shape (Figure 6.1). The geometry is inspired by the observation of the buckling modes of a single beam under compression, where short-wavelength buckling mode is never preferred for regular lattice materials under macroscopic compression. Numerical and

experimental investigation will be performed to study the macroscopic auxetic response of the proposed lattice materials. Our results indicate that the Poisson's ratios can be effectively tuned from negative to positive, which is attributed to the deformation behavior of sinusoidal beams transiting from bending-dominated to stretching-dominated behavior. It will be further shown that this transition phenomenon can be controlled by tailoring the amplitude and wavelength of the sinusoidal beams. The proposed lattice metamaterials exhibit significant broad phononic band gaps when compared with regular square lattice materials. In particular, these band gaps can be dynamically tuned by applying an external mechanical stimulus, like uniaxial stretching in our case.

A schematic of our 2D lattice microstructure with auxetic behavior is illustrated in Figure 6.1 (a) – (c). The shape of the sinusoidal beams can be mathematically described as $y = A_n \sin\left(n\pi x/l\right)$, where A_n is the wave amplitude, n is the number of half wavelength, and l is the length of regular straight beams. The length of the sinusoidal beam is given by:

$$s = \int_0^l \sqrt{1+\left(y'\right)^2}\,dx = \int_0^l \sqrt{1+\left(\frac{A_n n\pi}{l}\cos\left(\frac{n\pi x}{l}\right)\right)^2}\,dx\,, \tag{6.1}$$

Under the mass equivalence assumption, the width of the sinusoidal beam can be calculated as

$$w = t\cdot l \Bigg/ \int_0^l \sqrt{1+\left(\frac{A_n n\pi}{l}\cos\left(\frac{n\pi x}{l}\right)\right)^2}\,dx\,. \tag{6.2}$$

where t is the width of regular beams. Then, for a given $A_n n/l$, the width of the sinusoidal beam is the same for any n. In this work, we focus on structures with volume fraction smaller than 0.1, where $l/t > 15$ for all cases.

The proposed lattice materials are fabricated using a multi-material 3D printer (Objet Connex260, Stratasys). To ensure the stretchability of the cellular configuration a rubber-like material, Shore 95, is taken as the constitutive (core) material for the sinusoidal beams. Figure 6.1 (d) shows the center area of the specimen, which consists of an array of 4×5 unit cells with $A_n n/l = 1/3$, n=1, $w/l = 1/20$ and a representative sequence of images taken at different tensile strains. By simple inspection it is evident that at a small initial strain the lattice material expands transversally, indicating, therefore, the presence of an auxetic behavior. However, when the macroscopic tensile strain increases to 30%, the lattice material starts to contract along the x direction. These phenomena suggest that the fabricated 2D lattice materials exhibit auxetic behavior and a strain-dependent Poisson's ratio.

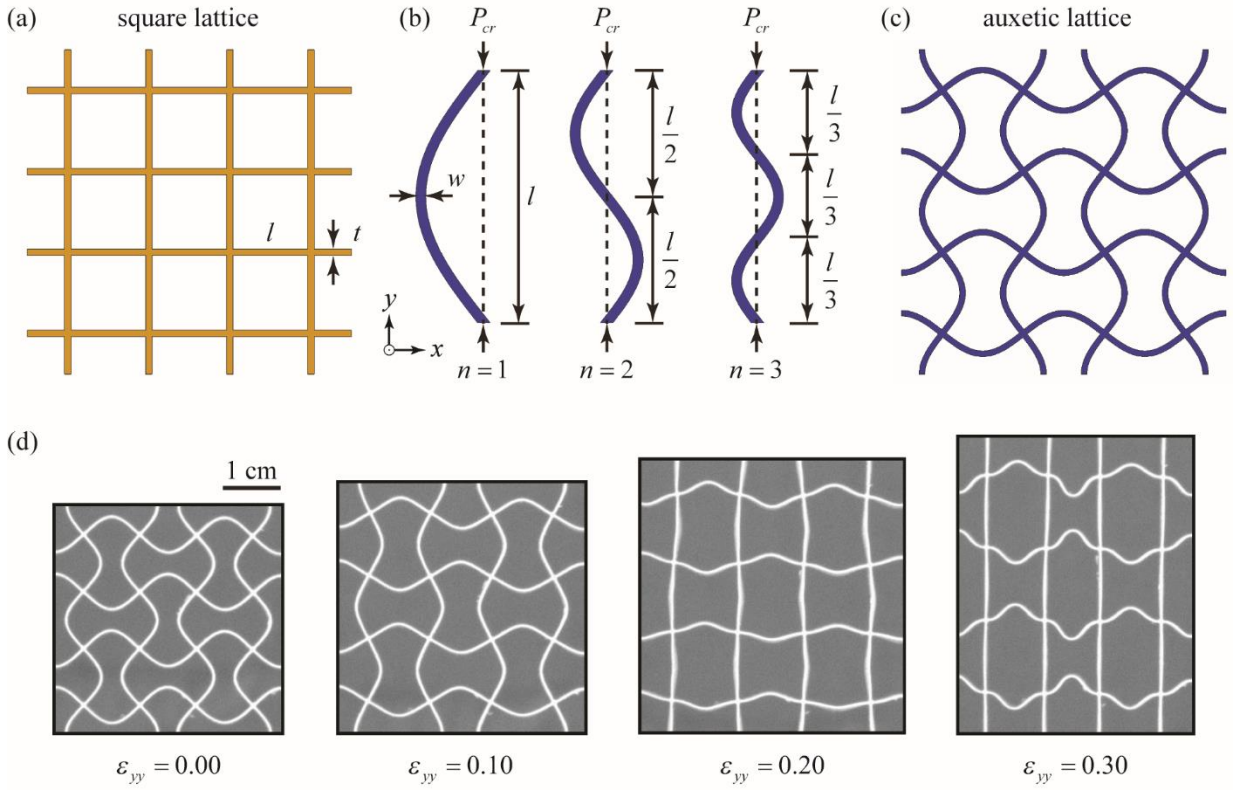

Figure 6.1 Schematics and deformation behavior of the sinusoidally architected lattice metamaterial. (a) Regular square lattice with 2×2 unit cells. Here t and l are the width and length

of regular beams. (b) Buckling modes of a single beam under compression. (c) Proposed architected lattice materials with 2×2 unit cells with n=1; (d) Deformation behavior of the center area consisting of 2×2 unit cells of the architected lattice material under uniaxial tension.

6.2.2 Mechanical testing

6.2.2.1 Specimen fabrication

Lattice materials were fabricated having overall dimensions of 80 mm×150 mm and being composed of 4×5 unit cells. Each beam ligament has a thickness of 405 ± 5 μm. Two beams were also added to the top and bottom of the lattice structures to improve the connection alignment. More details concerning 3D printing can be found in Chapter 2.

6.2.2.2 Tensile testing of the dogbone and lattice specimens

The experimental setup of the tensile testing is shown in Figure 6.2 (a). Detailed method can be found in Chapter 2.

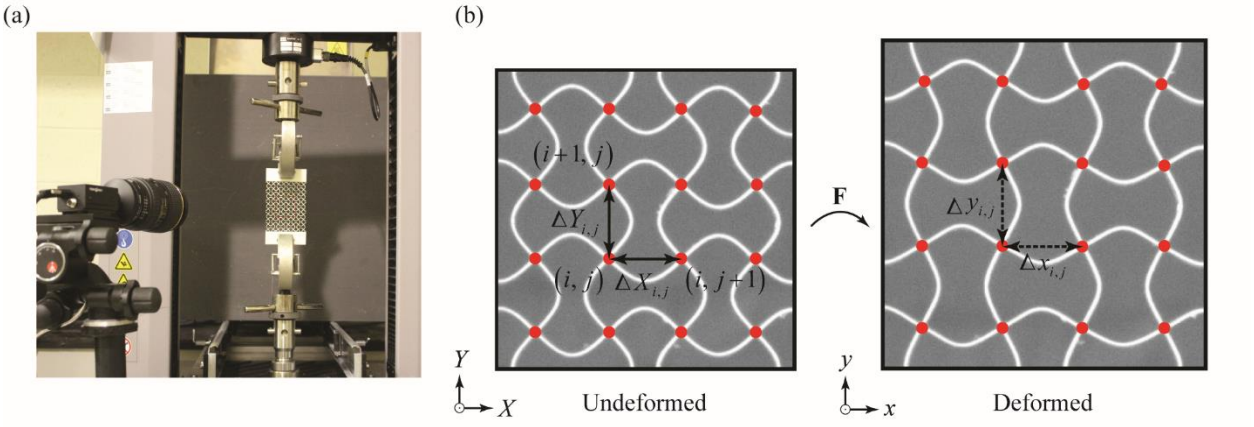

Figure 6.2 Experimental setup of uniaxial tension test. (a) Lattice specimen under uniaxial tension. (b) Calculation of Poisson's ratio.

6.2.2.3 Mechanical properties of constitutive material

The material properties of the Shore 95 rubber-like material were obtained by measuring the mechanical response of the 3D printed dogbone specimens. The experimental setup is shown in Figure 6.3 (a). Figure 6.3 (b) shows the measured stress-strain curves (true and engineering strain) under uniaxial tension. According to ASTM 412, the basic properties of Shore 95 are characterized by Young's modulus of E=5.5 MPa, Poisson's ratio ν=0.37, and density ρ=1157 kg/m^3. Here Young's modulus is obtained from the measured stress-strain curve of dogbone specimen. The density is obtained by averaging the densities of five dogbone specimens.

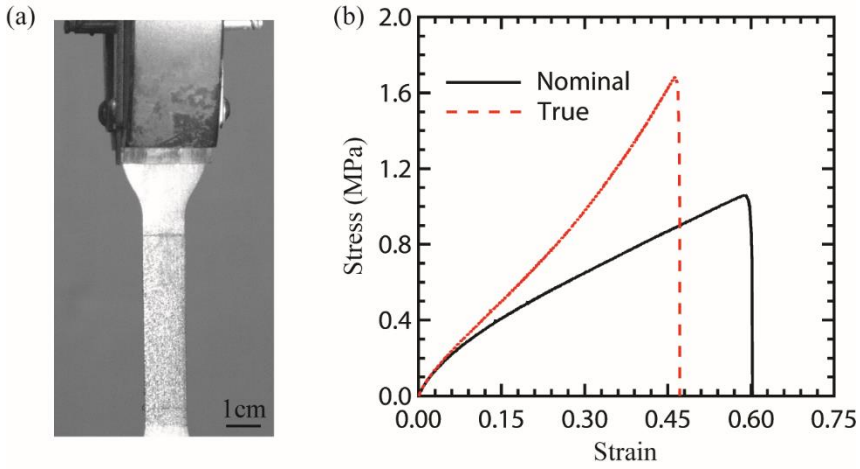

Figure 6.3 Material properties of the composition in 3D printing. (a) 3D printed dogbone specimen under uniaxial tension, (b) Measured stress-strain relation of the dogbone specimen.

6.2.2.4 Calculation of Poisson's ratio

To quantify the deformation taking place in the lattice materials during the experiments, an image processing software (ImageJ 1.49q) was used to determine the intersection points in the specimen. The deformation near the four edges of the specimen was affected by boundary conditions. Therefore we focused on the behavior of nine unit cells in the central part of the specimens to

avoid Saint Venant effects from the edges. The intersection points at the corners of the chosen unit cells were determined as $\left(X_{i,j}, Y_{i,j}\right)$ in the undeformed and $\left(x_{i,j}, y_{i,j}\right)$ in the deformed state, respectively. The row and the column indices vary between $1 < i < 4$ and $1 < j < 4$. For each unit cell, the horizontal and vertical distances were calculated from the coordinates $\left(x_{i,j}, y_{i,j}\right)$, i.e., $\Delta x_{i,j} = x_{i,j+1} - x_{i,j}$ and $\Delta y_{i,j} = y_{i+1,j} - y_{i,j}$. Prior to the application of the tensile loading, we assessed the deformations in the undeformed state, i.e., $\Delta X_{i,j} = X_{i,j+1} - X_{i,j}$ and $\Delta Y_{i,j} = Y_{i+1,j} - Y_{i,j}$. A schematic diagram of the central region of the lattice structure under consideration with the definitions of $\Delta x_{i,j}$, $\Delta y_{i,j}$, $\Delta X_{i,j}$ and $\Delta Y_{i,j}$ is shown in Figure 6.2 (b). The local homogenized values of the engineering strain for each unit cell were determined as:

$$\varepsilon_{xx,i,j} = \Delta x_{i,j} / \Delta X_{i,j} - 1 \text{ and } \varepsilon_{yy,i,j} = \Delta y_{i,j} / \Delta Y_{i,j} - 1, \tag{6.3}$$

The local values of the engineering strain were then used to calculate local values of the incremental Poisson's ratio as:

$$\nu_{i,j} = -\frac{\varepsilon_{xx,i,j}}{\varepsilon_{yy,i,j}}. \tag{6.4}$$

Finally, the ensemble average incremental Poisson's ratio of the nine central unit cells under consideration was computed as $\nu_{yx} = \left\langle \nu_{i,j} \right\rangle$.

6.2.3 Numerical modeling

6.2.3.1 Mechanical response simulation

The numerical simulations related to the mechanical response of the lattice materials are conducted using commercial FE package COMSOL Multiphysics. FE models with a finite number of unit

cells are investigated in this study. After trade-off studies between CPU costs and edge effects provided by the finite number of unit cells, we have used models with 4×5 unit cells in all the simulations (Figure 6.4 (a)). To provide a more uniform tensile displacement distribution we have intentionally added a rectangular beam-like section with 5 mm width on the top and bottom of the finite-size models. Plane strain condition is assumed during the simulations. The models are meshed with 6-node triangular elements and 6 elements are generated along the width of the beam after a convergence test.

During all of the simulations, the mechanical response of the constitutive material is modeled as nonlinear elastic. We did not specifically fit the experimentally measured data using hyperelastic models and did not discriminate between elastic and plastic behavior. Instead, the true stress-strain relation from the dogbone is directly exported to COMSOL Multiphysics and implemented as the constitutive equation for the core material. In addition, geometric nonlinearity is considered to represent the large deformation of the structure. During the simulations, a uniaxial displacement loading is applied on the top of the beam, while the bottom is fixed along both the *x* and *y* directions (Figure 6.4 (a)).

The postprocessing of the results was focused on the unit cell in the central region only to avoid finite size and boundary conditions effects (Figure 6.4). The Poisson's ratio can be calculated from the ratio of the nominal strain in the horizontal edge and vertical edge of the rectangular unit cell. Specifically, we first calculated the average displacement components of the four edges, from which the strain along horizontal and vertical directions can be calculated as:

$$\varepsilon_x = \frac{\bar{u}^R - \bar{u}^L}{2l} \text{ and } \varepsilon_y = \frac{\bar{v}^T - \bar{v}^B}{2l}, \tag{6.5}$$

In equation (3) $\bar{u}$ and $\bar{v}$ indicate the averaged horizontal and vertical displacement components respectively; *R*, *L*, *T*, and *B* denote the right, left, top, and bottom edges of the unit cell, (Figure 6.4 (b)). Finally, the incremental Poisson's ratio is calculated as:

$$v_{yx} = -\frac{\varepsilon_x}{\varepsilon_y}. \tag{6.6}$$

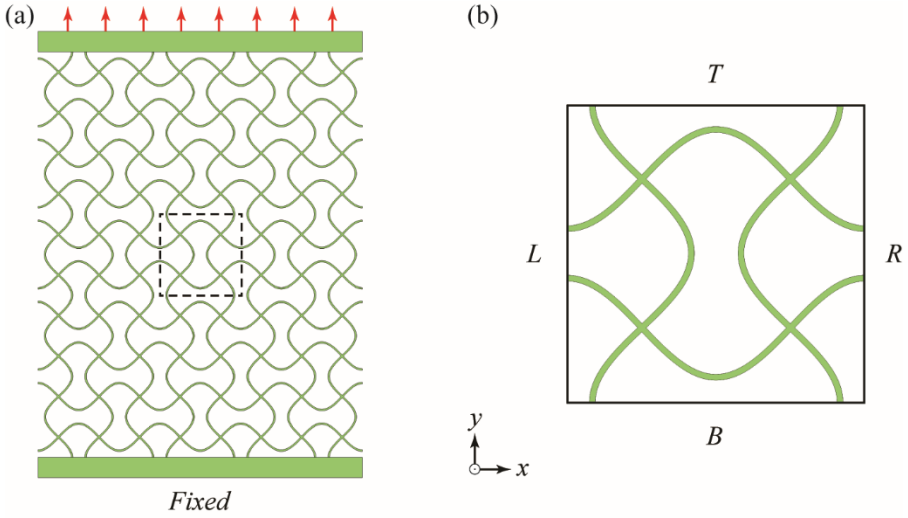

Figure 6.4 FE model for mechanical response simulation. (a) FE model with 4×5 unit cells and (b) Rectangular unit cell in the central area of FE model for the calculation of Poisson's ratio.

6.2.3.2 Low amplitude wave propagation simulation

The analysis of the effect of external mechanical stimuli on the vibration mitigation capability consists of the following two steps. First, the global structure is uniaxially stretched to the desired level of deformation. Still focusing on the central unit cell of the whole lattice as the representative unit cell for the corresponding infinitely periodic structure, we have then isolated the deformed geometry of this representative unit cell for the wave propagation analysis. Since our focus is on the topology of the metamaterial design, the residual stresses in the deformed structure are neglected. Secondly, we have conducted the Bloch wave analysis on the deformed unit cell at each

level of stretching strain. The wave propagation analysis procedure is the same as that for the initial unit cell, except that the first irreducible Brillouin zone needs to be updated for each deformed unit cell.

6.3 Results and discussion

6.3.1 Auxetic behavior of lattice materials

Figure 6.5 (a) shows the macroscopic stress-strain relations of three selected specimens under uniaxial tension. The Arruda-Boyce hyperelastic model can accurately capture the mechanical behavior of the lattice metamaterials. At high strain level, numerical predictions slightly deviate from the experimentally measured data. The discrepancy between numerical and experimental data is mainly due to the failure of some beam ligaments. When the applied strain is higher than 0.35, some beams starts to break, leading to the drop in the stress-strain curves. Since the specimens are fabricated layer-by-layer in the 3D printer, anisotropy, porosity, and imperfections are introduced during 3D printing, [190, 191] which also play a role. These specific aspects are not taken into consideration in our model.

We find that these structures exhibit J-shaped stress-strain curves, which are very similar to the mechanical response of bioinspired soft network composite materials and other stretchable electronics. [185-188] However, the stress-strain behavior is different from that of plates with rectangular auxetic perforations, which exhibit a softening phenomenon in the tensile stress- strain curve for an increasing magnitude of Poisson's ratio. [175] Apparently, at small strains the structure has an auxetic behavior, moving from a more anti-rubber behavior (n = 1) to be marginally auxetic (n = 3, $\nu_{yx} \sim 0$). The lowest stiffness at small and medium strains (up to ~ 0.20) belongs to the specimens with the most negative ν_{xy}. That means that under tensile loading the

cross section of the specimen increases, and therefore for a given tensile force the equivalent stress is lower. Close to a critical strain (i.e., when $\nu_{yx} \sim 0$), the lattice tends to provide an equivalent constant cross section for increasing strains. Densification is apparent at strains close to 0.22 – 0.25, when the Poisson's ratio tends to change dramatically and decrease its magnitude, coming close to be marginally auxetic or even slightly PPR, depending on the sinusoidal order adopted. This unique deformation behavior is intrinsically dictated by the sinusoidal architecture of the artificially designed ligaments. The pre-set configuration of the sinusoidally shaped ligaments enables switching deformation mechanisms between bending and stretching of the ligaments. [192] In conventional lattice materials with straight beams, this deformation transformation is not envisioned.

The numerical and experimental results of the Poisson's ratio of the lattice metamaterials as a function of the tensile strain are presented in Figure 6.5 (b). For tensile strains below 0.20, the numerical predictions tend to slightly overestimate the experimental results for n=1 and 2. Note that since the lattice metamaterials are soft, unavoidable misalignments in the test setup can influence the measurement of the Poisson's ratios. Furthermore, when calculating the Poisson's ratio by means of digital image correlation, minor errors can be introduced in the processing. We also note that over this range of strain, the proposed square lattice metamaterials exhibit a nearly constant negative Poisson's ratio. This is because vertical and horizontal beams are both subjected to bending at macroscopic strains below 0.2 (Figure 6.5 (c)). At this small strain range, the magnitudes of the vertical and horizontal strain increments are changing in a similar manner. As a result, the Poisson ratio is nearly constant. With the increase of the stretching, the Poisson's ratio gradually turns from negative to marginally positive. To elucidate the mechanisms responsible for the transition of the Poisson's ratio we present the mechanical response of a representative unit

cell taken from the central area of the specimen under different tensile strains (Figure 6.5 (c)). Here we only show the mechanical behavior of the lattice metamaterials with n=1 and 3. Again, one can notice an excellent agreement between the numerical and the experimental deformations. At strains below ~0.20, the deformation response of the vertical beams is clearly bending-dominated due to the initial curvature of sinusoidal architecture. With the increase of macroscopic stretching, the sinusoidal architecture will be stretched to an approximately straight beam. As a result, the deformation behavior will become stretching-dominated and very similar to regular materials, which typically exhibit a positive or zero Poisson's ratio. Here the numerical and experimental results demonstrate that a mechanically tunable negative Poisson's ratio can be achieved by introducing curved sinusoidal beams in regular lattice structures. The evolution of the Poisson' ratio strongly depends on the coupled deformation behavior of vertical and horizontal beams.

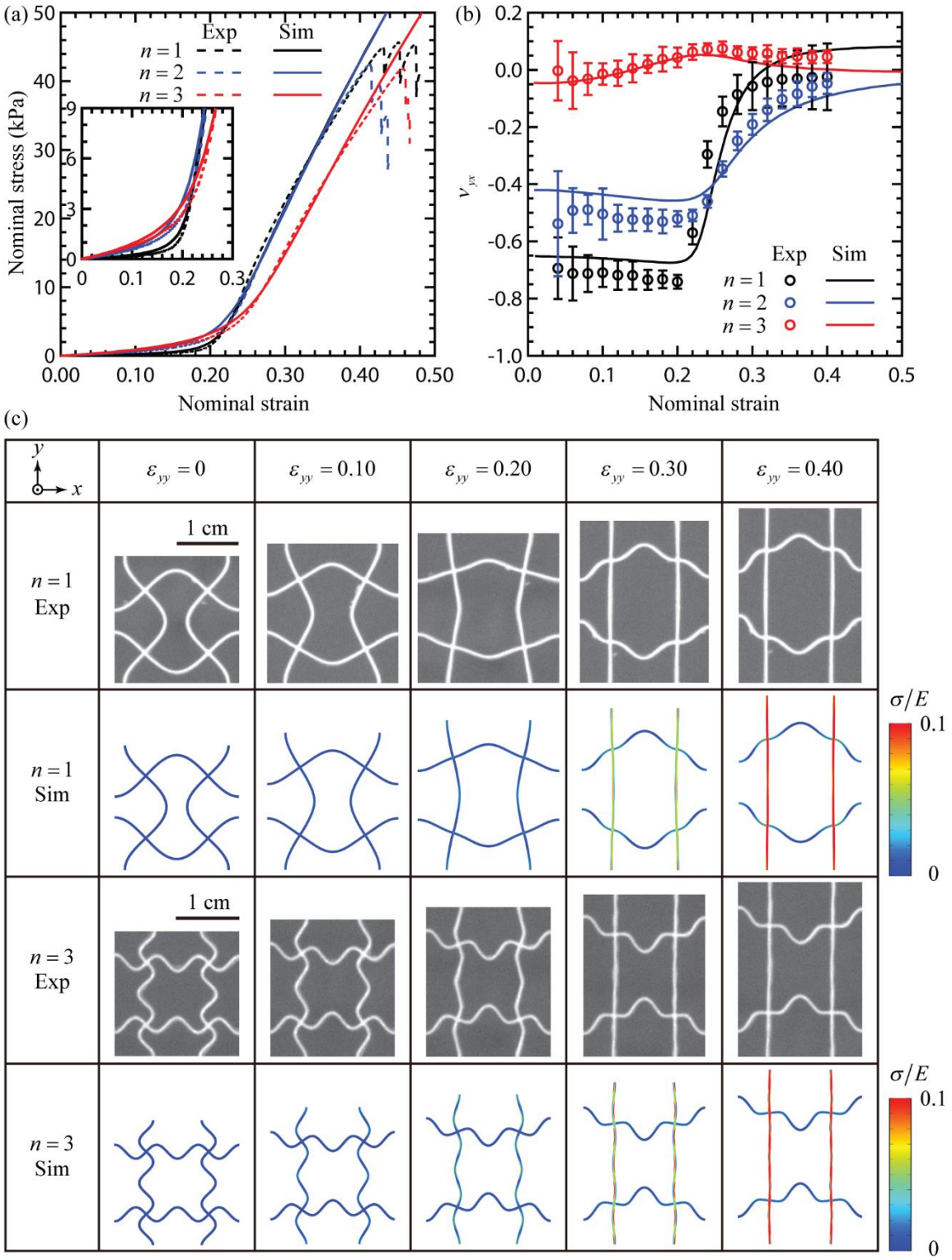

Figure 6.5 Mechanical response of lattice metamaterials under uniaxial stretching. (a) Stress-strain relations of the architected lattice metamaterials. (b) Evolution of the Poisson's ratios as a function

of the applied tensile strain. (c) Deformed configuration at different macroscopic strains. The von Mises stresses are normalized with respect to the Young's modulus of the constitutive materials. Here $A_n n/l = 1/3$.

6.3.2 Mechanically tunable Poisson's ratios

Having demonstrated that the sinusoidally architected lattice metamaterials exhibit auxetic behavior under uniaxial tension at specific strain ranges, we now systematically investigate the effects of amplitude $A_n n/l$ and half wavelength *n* on the mechanical response and the Poisson's ratios. Figure 6.6 (a) shows the stress-strain relations of the lattice metamaterials with different $A_n n/l$ and *n*. Each structure exhibits a J-shaped stress-strain curve, which is similar to our previous experimental observation. For a given amplitude a short wavelength (i.e., a large *n*) gives rise to a higher stress-strain curve, indicating the presence of a significantly stiffer mechanical response. For a given value of *n* a smaller wave amplitude (i.e., a smaller curvature but with a larger beam width) however, leads to a higher stress-strain curve within the small strains range. These mechanical responses are intrinsically controlled by the bending stiffness of the sinusoidal curved beams, which is defined as $S = CE\kappa w^3$, where *C* is the geometric constant, *E* is the Young's modulus of the beam, κ is the curvature, and *w* is the width of the beam. The effective stiffness of the lattice metamaterials as a function of $A_n n/l$ and *n* are summarized in Figure 6.7 (a). We further note that for a given wave amplitude a significant auxetic behavior can be observed for *n*=1, 2 (Figure 6.6 (b)). Interestingly, the transition strain for the in-plane Poisson's ratio is proportional to the wave amplitude because large macroscopic stretching is needed to make straight vertical beams with larger wave amplitudes. The minimum Poisson's ratios as a function of $A_n n/l$ and *n* are summarized in Figure 6.7 (b).

We have numerically demonstrated that the geometric parameters of the sinusoidally curved beams have a great impact on the evolution of the Poisson's ratio. Among these, the number of half wavelength *n* is critical to the existence of the auxetic behavior. For a smaller *n*, strong synergistic deformation behavior exists between horizontal behavior and vertical behavior. As a result, the pre-existing deformation can be harnessed to generate an auxetic behavior. However, with the increase of *n*, this synergistic deformation between vertical and horizontal beams becomes week. For a given *n*, the wave amplitude is crucial to the transition between negative Poisson' ratio and positive Poisson's ratio.

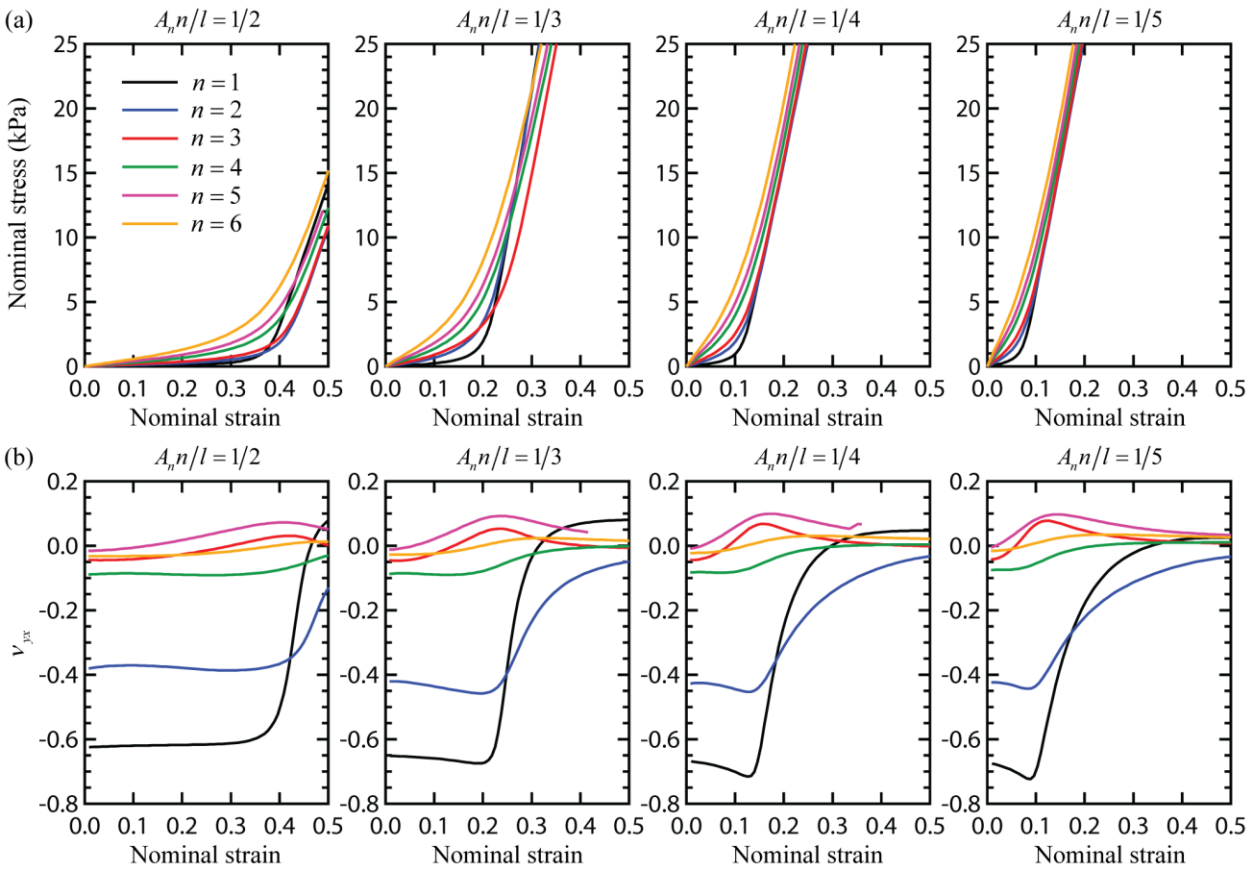

Figure 6.6 Effects of geometric features of the ligament on the mechanical response. (a) Effect of amplitude, $A_n n/l$ and (b) number of half wavelength, *n*, on the stress-strain relation and Poisson' ratio. Here $w/l = 1/20$ for all of the simulations.

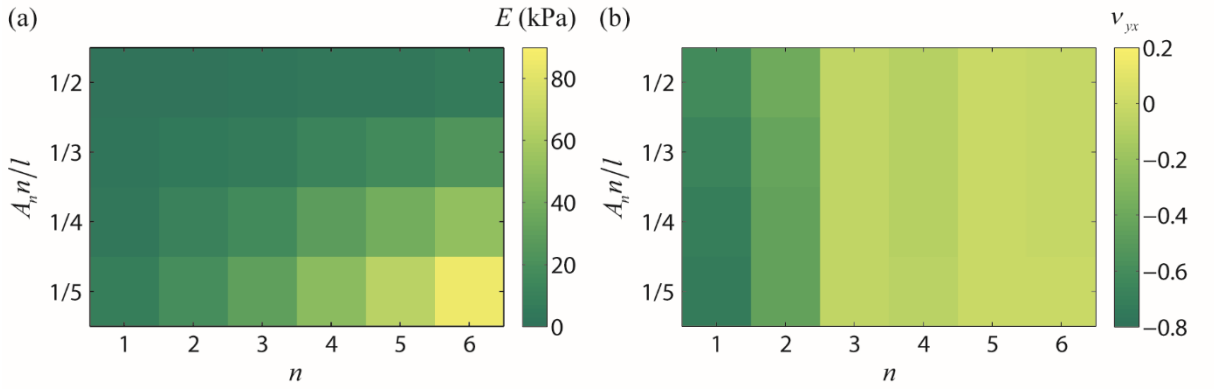

Figure 6.7 Effects of geometric features of the ligament on stiffness and Poisson's ratio. Effect of amplitude, $A_n n/l$ and the number of half wavelength, *n*, on the (a) effective stiffness and (b) Poisson' ratio of the proposed lattice metamaterials.

Another geometric parameter with a significant impact on the mechanical response and in-plane Poisson's ratios is the slenderness ratio w/l. To demonstrate this, we examine the mechanical response and the auxetic behavior of the lattice material with $A_n n/l = 1/3$ and *n*=1, 2. Highly nonlinear stress-strain curves arise in those cases for a small strain range (Figure 6.8(a)) because the mechanical response of the sinusoidally curved beam is bending-dominated, with the bending stiffness being proportional to w^3. Therefore, large slenderness ratio will give rise to higher stiffness. At large strains the mechanical response of sinusoidally curved beam becomes stretching-dominated and a nearly linear response can be observed in the stress-strain curves.

The bending-dominated and stretching-dominated behaviors at different strains have also a significant impact on the Poisson's ratios (Figure 6.8 (b)). At strains below 0.20, the lattice

metamaterials with n=1 and 2 have a nearly constant negative Poisson's ratio of ~ -0.65 and ~ -0.45, respectively. This phenomenon indicates that the Poisson's ratio is almost independent of the slenderness ratio when the sinusoidally curved beams are highly bending-dominated. By contrast, at large stretching strain, the Poisson's ratio rapidly changes from negative to positive for both cases. The transition is much sharper for a smaller slenderness ratio, since the nearly straight beam is, in this case, more compliant.

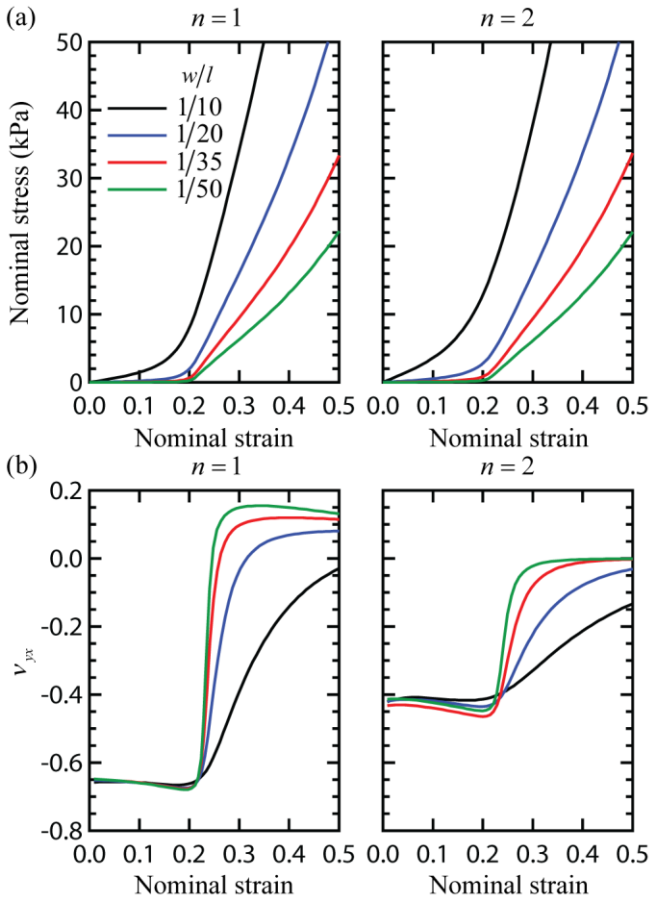

Figure 6.8 Effect of slenderness on the stress-strain relation and Poisson's ratios of the proposed lattice metamaterials. (a) Evolution of stress-strain relation and (b) Poisson's ratio. Here $A_n n/l = 1/3$.

6.3.3 Effect of the lattice topology

Having shown that the mechanical response and the Poisson's ratios can be tuned by tailoring the geometric features of the sinusoidally curved beams, we now proceed to examine the effect of the lattice topology on the auxetic behavior from a numerical and experimental standpoint. Four types of sinusoidally architected lattice metamaterials with hexagonal, Kagome, square, and triangular topology are fabricated using 3D printing (Figure 6.9 (a)). Here we use as geometry parameters $A_n n/l = 1/3$ and n=2. The specific lattice topology has a significant impact on the overall mechanical response of the lattice metamaterials under tension (Figure 6.9 (b)). The triangular lattice has (as expected) the largest stiffness, while the hexagonal tessellation is the more compliant. [136] Experimental and numerical results related to the Poisson's ratios for the four types of topology are presented in Figure 6.9 (c), and they all show a good agreement. In contrast to the negative Poisson's ratio of square lattice metamaterials, both hexagonal and kagome lattice configurations exhibit a positive Poisson's ratio below 0.40 tensile strains. The evolution of the Poisson's ratio of the triangular lattice is however strongly strain-dependent and there is a switch between NPR and PPR at a critical strain of 24%.

This metamaterial design concept can be extended to other lattice topologies, thereby offering new deformation behaviors and mechanical responses. For example, it is well known that regular beams in hexagonal lattices are bending-dominated, while the introduction of sinusoidally curved beams enables the coexisting of bending and stretching behavior. The study of the effect of lattice topology not only provides new opportunities to tailor the auxetic behavior but also provides us a better understanding of the coupling deformation behavior in new lattice metamaterials. It is anticipated that topologies along with sinusoidal architecture can be used to explore new mechanical properties and other functionalities.

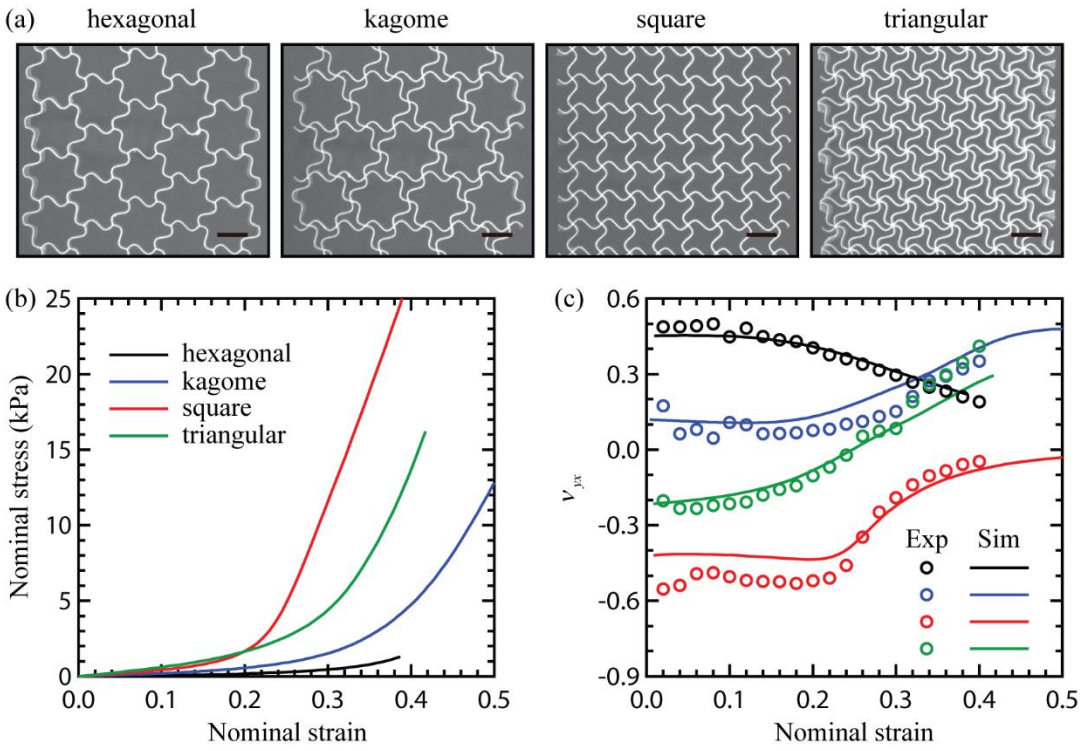

Figure 6.9 Effect of the topology on the stress-strain curves and Poisson's ratio. (a) 3D printed specimens with hexagonal, Kagome, square, and triangular topology. (b) Stress-strain relations and (c) Evolution of Poisson's ratio as a function of the strain. The legend is the same as that in (b). Here $A_n n/l = 1/3$, n=2, and $w/l = 1/20$. Scale bar: 1cm.

6.3.4 Broad and multiple phononic band gaps

We have demonstrated that the proposed sinusoidally architected lattice metamaterials exhibit tunable Poisson's ratios over a large tensile strain range. The evolution of Poisson's ratio strongly depends on the geometric features of the sinusoidal architecture as well as the global topology of the lattice metamaterials. From a metamaterial design perspective, the interplay between Poisson's ratios and the intrinsic architecture can guide us to explore other functionalities arising from the use of these architected materials. In this section, we investigate the elastic wave propagation

occurring within these lattice metamaterials and explore their capability in providing a dynamic tunability for vibration alleviation using an external mechanical stimulus.

We start by examining the phononic dispersion relations and the transmission spectra of the lattice metamaterials. [24, 59-62, 193] In our case, the normalized frequency is defined as $\Omega = \omega/\omega_1$, where ω is the frequency of the elastic wave obtained by solving the Bloch eigenvalue problem and $\omega_1 = \pi^2\sqrt{Et^2/12\rho l^4}$ is the first pinned-pinned flexural resonance frequency of a lattice beam. [133] For the material and structures studied in this work $\omega_1 = 982$.

Figure 6.10 (a)-(d) show the phononic dispersion relations and the associated transmission spectra of a regular lattice material (*A*=0, *n*=0) and configurations with $A_n n/l = 1/3$ and *n*=1, 3, 5. The simulated transmission spectrum for each lattice material agrees extremely well with the presence of the partial band gaps along the M-K direction found via the Bloch wave analysis. No band gaps exist in the regular lattice material, however, five complete band gaps can be observed for the sinusoidally architected lattice material with *n*=1. Within the observed band gaps, the largest one lies within Ω=1.12-1.36. Both multiple and broad phononic band gaps arise for *n*=3 and 5. More specifically, five and six complete band gaps emerge for *n*=3 and 5, and the maximum band gaps for *n*=3 and 5 lies within Ω=3.25-3.59 and Ω=0.79-1.26, respectively. A direct comparison between the geometric features of the regular and proposed lattice metamaterials shows that mechanism associated with the broad and multiple band gaps formation are intrinsically dictated by the wave amplitude and wavelength of the sinusoidally curved beams, leading to the coupling of axial and bending motion. [194] The formation of complete wave band gaps can be due to Bragg scattering and/or local resonances. For our lattice metamaterials, both effects can be observed in the phononic dispersion diagram. For example, for *n*=5, local resonances are

responsible for the first two band gaps, as evidenced by the flat bands between these two band gaps (Figure 6.10 (d)). Other band gaps are attributed to Bragg scattering at both the microstructural level of the sinusoidally curved beam as well as the macroscopic level of lattice topology.

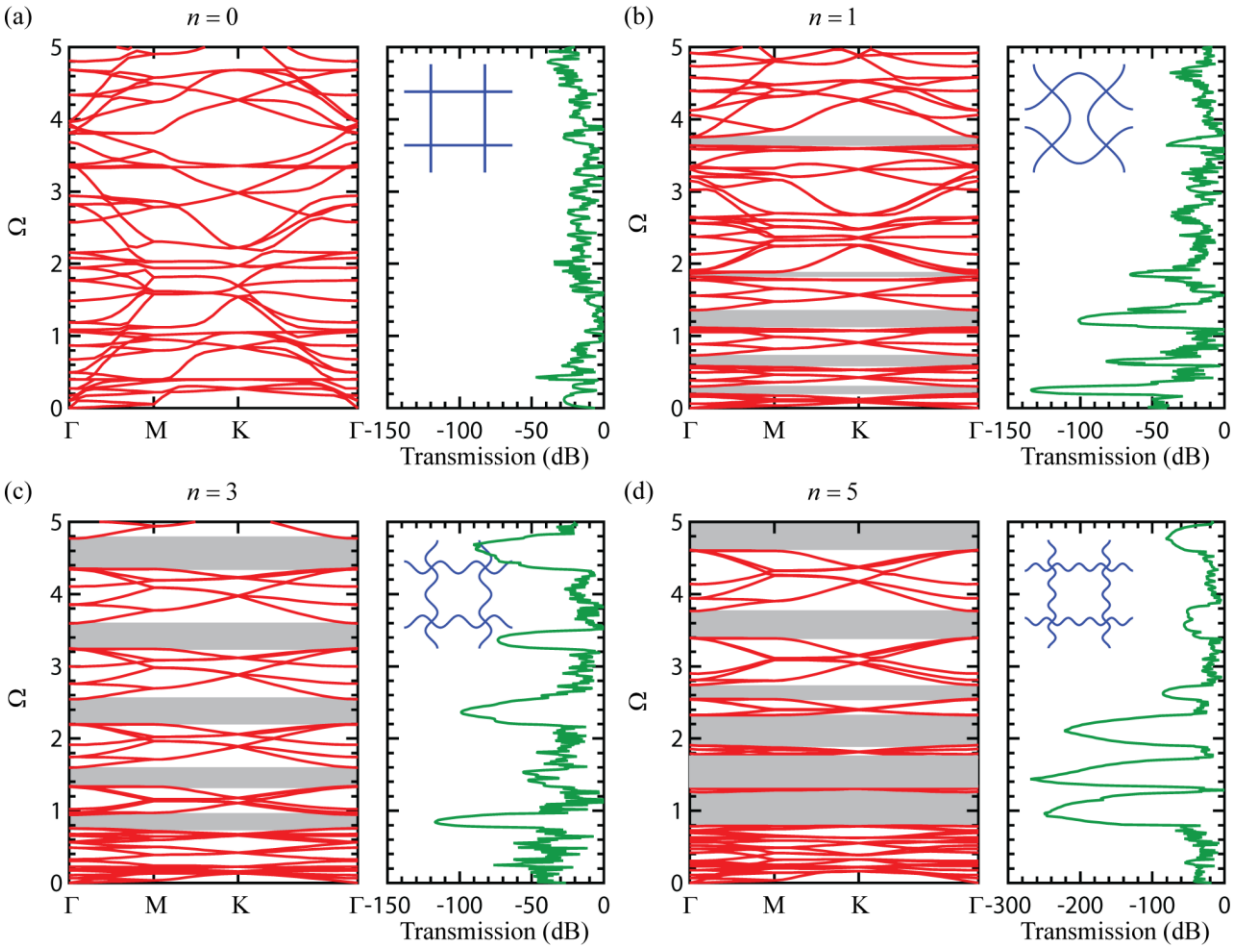

Figure 6.10 Phononic dispersion relations and transmission spectra of the architected lattice metamaterials. (a) $A=0$, $n=0$; (b) $A_n n/l=1/3$, $n=1$; (c) $A_n n/l=1/3$, $n=3$;(d) $A_n n/l=1/3$, $n=5$. Here $w/l=1/20$ for all of the simulations.

6.3.5 Mechanically tunable phononic band gaps

We have shown that by introducing a sinusoidal architecture into regular lattice metamaterials broad and multiple phononic band gaps can arise. It is obvious that these band gaps can be tuned

by tailoring the geometric features of the ligaments (beams) of the lattice metamaterials. Here, we explore the dynamic tunability of the phononic band gaps using now an external mechanical stimulus, i.e., a uniaxial tensile deformation. Figure 6.11 (a) and (b) show the phononic dispersion relations at different stretching strains for n=4 and 6, respectively. We note that most of the initial band gaps will close for n=4, while the band gaps tend to shrink for n=6 with the increase of the applied stretching. To better understand the effect provided by the applied tensile strain we plot the evolution of the band gaps as a function of ε_{yy} for n=2, 4, 6 (Figure 6.11 (c)). It is interesting to note that for n=2 all of the band gaps are suppressed when stretching the lattice material by 30%. For n=4 and 6 the band gaps will partially close, while new band gaps will arise with the increase of the applied tensile strain. The sinusoidal architecture of the beams not only gives rise to broad and multiple phononic band gaps but also allows to tune dynamically the same band gaps by virtue of the beam compliance. From a geometric perspective, this prominent vibration control capability of the proposed lattice material is intrinsically associated with the introduced sinusoidally corrugated ligaments and its peculiar deformation behavior. These phenomena suggest that the application of a uniaxial stretching can be viewed as a new tool to control the vibration mitigation and suppression for the proposed lattice metamaterials, which therefore can be used as programmable devices for wave filtering and waveguiding.

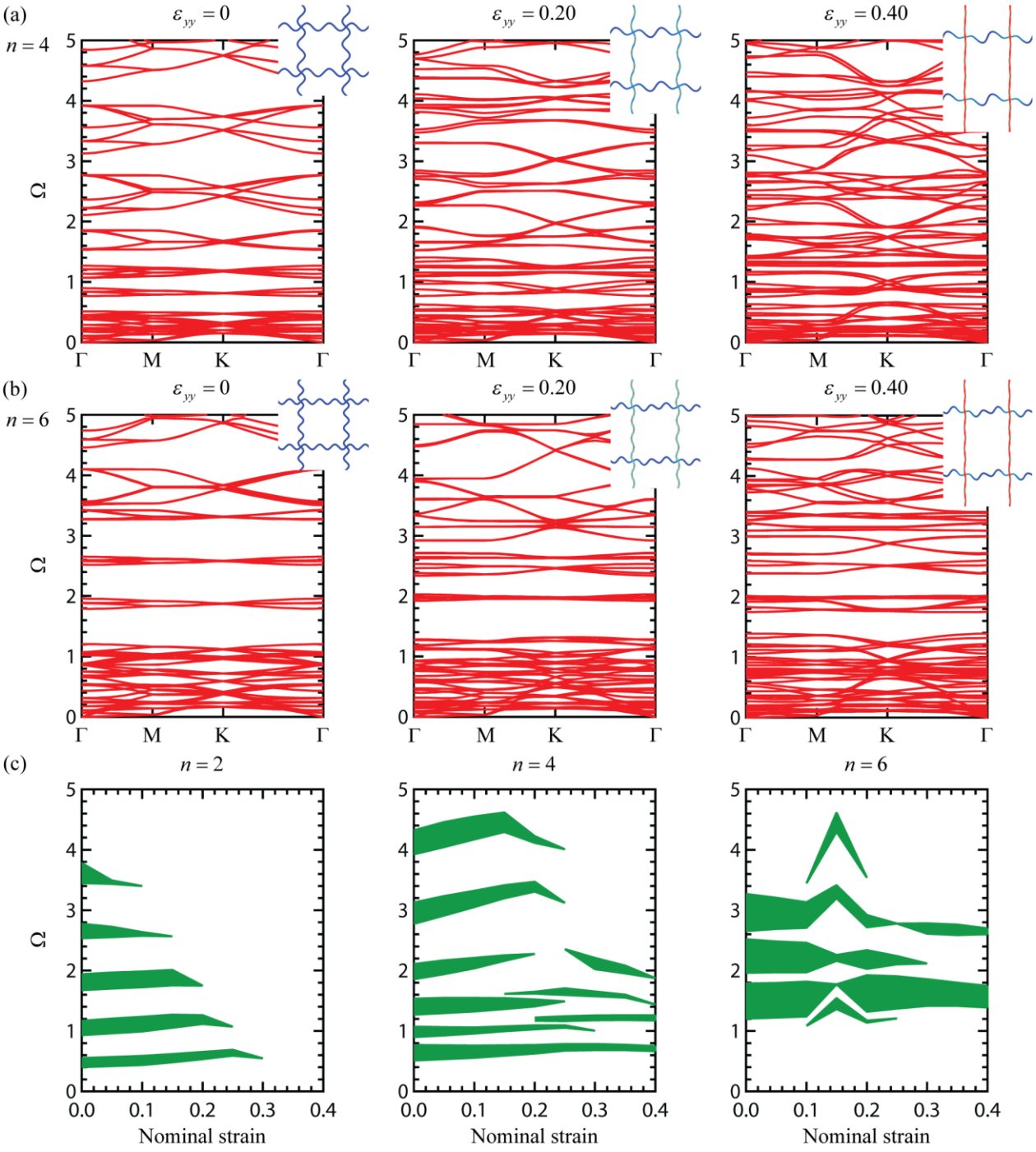

Figure 6.11 Mechanically tunable band gaps for the architected lattice metamaterials. Phononic dispersion relations as a function of stretching strain for (a) $n = 4$ and (b) $n = 6$; (c) Evolution of band gaps as a function of strain for $n = 2$, $n = 4$, and $n = 6$. Here $A_n n/l = 1/3$ and $w/l = 1/20$ for all simulations. The insets show the deformation of the unit cell at each stretching strain.

6.4 Conclusions

A novel class of lattice metamaterials with sinusoidally architected beams has been proposed in this chapter. Mechanical response and wave propagation performances were systematically investigated. Under uniaxial tension, the proposed sinusoidal architecture in the lattice beams provides an intrinsic deformation mechanism to switch from bending-dominated to stretching-dominated behavior. This transition of deformation mechanisms allows obtaining tunable Poisson's ratios over a large tensile strain range. Our experimental and numerical results show a very good agreement in terms of overall stress-strain relations, Poisson's ratios, and deformation patterns exhibited by these lattices. The investigation into the interplay between the multiscale (ligament and cell) architecture and wave propagation shows that broad and multiple phononic band gaps can be achieved in these lattice materials. Quite importantly, this significant vibration mitigation capability can be dynamically tuned by an external mechanical stimulus, i.e., a uniaxial stretching. The deformation behavior of the proposed metamaterials, together with their vibration mitigation capability makes them particularly suitable for the design of programmable mechanical metamaterials. The findings presented here provide new insights into the development of architected metamaterials with unusual physical properties and a broad range of potential applications, such as tunable particle filters and adjustable acoustic metamaterials for vibration control.

CHAPTER 7. ENGINEERING LATTICE METAMATERIALS FOR BROADBAND AND MULTIBAND VIBRATION MITIGATION

7.1 Introduction

We have numerically demonstrated that architected lattice metamaterials with sinusoidally-shaped ligaments exhibit auxetic behavior, which can be further harnessed to tune the phononic band gaps. In this Chapter, we will demonstrate from numerical and experimental standpoints that broad and multiple phononic band gaps can be achieved these lattice metamaterials. Our metamaterials are created by replacing straight ligaments in conventional lattices with sinusoidally-shaped ligaments (Figure 7.1). This metamaterial design concept is motivated by the observation that buckled-shape structures can be exploited to create tunable phononic band gaps. [195, 196] Note that here we do not create the desired buckled lattice metamaterials using an external mechanical loading because short-wavelength buckling mode is never preferred for regular lattice metamaterials under macroscopic compression. [197, 198] We will first investigate the band gaps properties of the proposed lattice metamaterials by performing Bloch wave analysis in an infinitely periodic system. Low amplitude wave transmission tests will be conducted on 3D printed samples to validate our model predictions. We show that the proposed metamaterial design concept is robust and efficient to generate broad and multiple band gaps. The metamaterial can be extended to curved ligaments with different amplitudes, wavelengths, aspect ratios, and other topologies.

7.2 Characterization of the lattice metamaterials

We begin by characterizing the proposed lattice metamaterial with a square topology, as schematically shown in Figure 7.1 (a)-(c). The sinusoidally-shaped ligament can be mathematically described as:

$$y = A_n \sin\left(n\pi x/l\right), \tag{7.1}$$

where A_n is the wave amplitude, n is the number of half sinusoid and l is the length of a regular straight beam. The length of the sinusoidally-shaped ligament is:

$$s = \int_0^l \sqrt{1+\left(\frac{A_n n\pi}{l}\cos\left(\frac{n\pi x}{l}\right)\right)^2}\,dx, \tag{7.2}$$

Under the mass equivalence assumption, the width of the curved ligament beam can be calculated as

$$w = t\cdot l \Big/ \int_0^l \sqrt{1+\left(\frac{A_n n\pi}{l}\cos\left(\frac{n\pi x}{l}\right)\right)^2}\,dx, \tag{7.3}$$

where t is the thickness of a regular ligament. For a given parameter $A_n n/l$ the width of the curved ligament is the same for any n. We, therefore, define two parameters to describe the curved ligament: the normalized wave amplitude $A_n n/l$ and normalized wavelength $1/n$. The shape of the unit cell in the parameters space is illustrated in Figure 7.1(d).

For the following simulations and tests, the length and thickness of a regular ligament are l =2.25 cm and t =0.1125 cm ($l/t = 20$) respectively unless otherwise specified. The out-of-the-

plane thickness of each lattice metamaterial is t_0=2.5 cm. The lattice metamaterials are made of Verowhite (Stratasys, Ltd) with measured Young's modulus E=1.6 GPa, Poisson's ratio ν=0.33, and density of ρ=1174 kg m^{-3}.

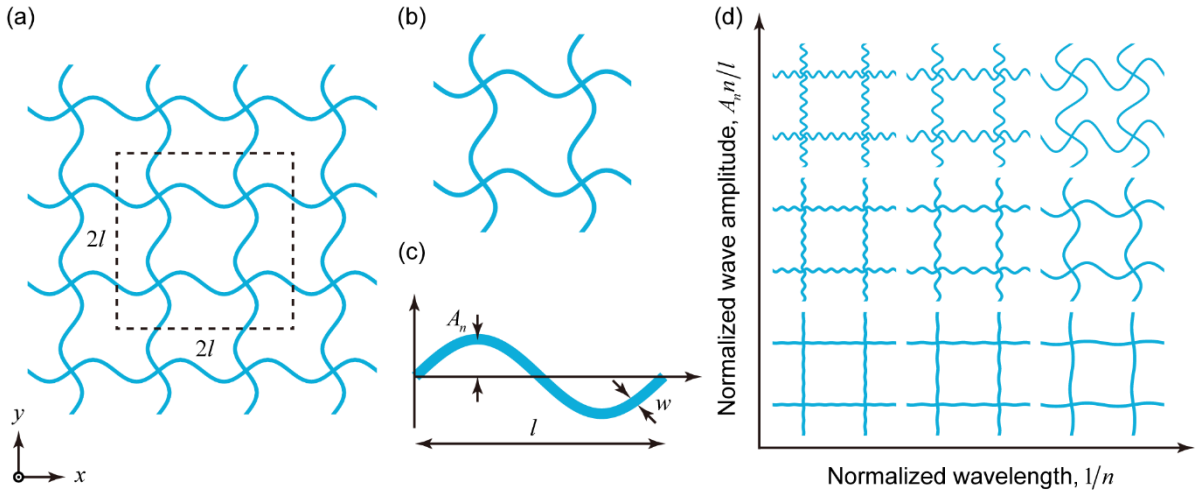

Figure 7.1 Schematics of the proposed lattice metamaterials with curved ligaments. (a) Schematics of the lattice metamaterials. (b) Unit cell. (c) Sinusoidally-shaped ligament, and (d) different unit cells in the ($1/n$, A_n/l) parameter space.

All specimens including cylinders and lattice specimens used in the study have been printed by using an Objet Connex260 multi-material 3D printer (Stratasys, Ltd). Verowhite is the constitutive material used during the 3D printing. The chemistry of these materials is proprietary to Stratasys. The dimensions of the cylinder comply with the ones prescribed by the ASTM D695 standard.

The material properties of the Verowhite were obtained by measuring the mechanical response of the 3D printed cylinder specimens. Figure 7.2 shows the measured stress-strain curves (true and engineering strain) under uniaxial compression. According to ASTM D695, the basic properties of Verowhite are characterized by Young's modulus E=1.6 $\pm$ 0.1 GPa, Poisson's ratio ν=0.33,

and density of ρ =1174 kg m^{-3}. Here Young's modulus has been obtained from the measured stress-strain curve of the cylinder specimen. The density is obtained by averaging the densities of five cylinder specimens.

Lattice metamaterials with different ligament wavelengths have an overall dimension of 229.5 mm ×90 mm ×25 mm and are composed of 5 ×2 unit cells (Figure 7.3). The lattice metamaterials with different topologies have an overall dimension of 234 mm ×160 mm ×25 mm (Figure 7.4). Two beams were also added to the top and bottom of the lattice structures to improve the alignment of the connection. Within the limitation of 3D printing technology, the layer orientation was found to influence the mechanical properties of the material; therefore, all the specimens were printed along the same orientation on the printer build platform. The as-fabricated specimens were kept at room temperature for 7 days to allow for the saturation of the curing.

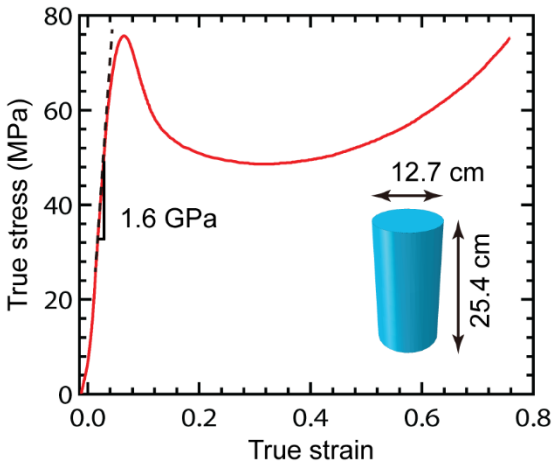

Figure 7.2 Measured stress-strain relation for Verowhite. The inset shows the dimensions of the 3D printed cylinder specimen under uniaxial compression.

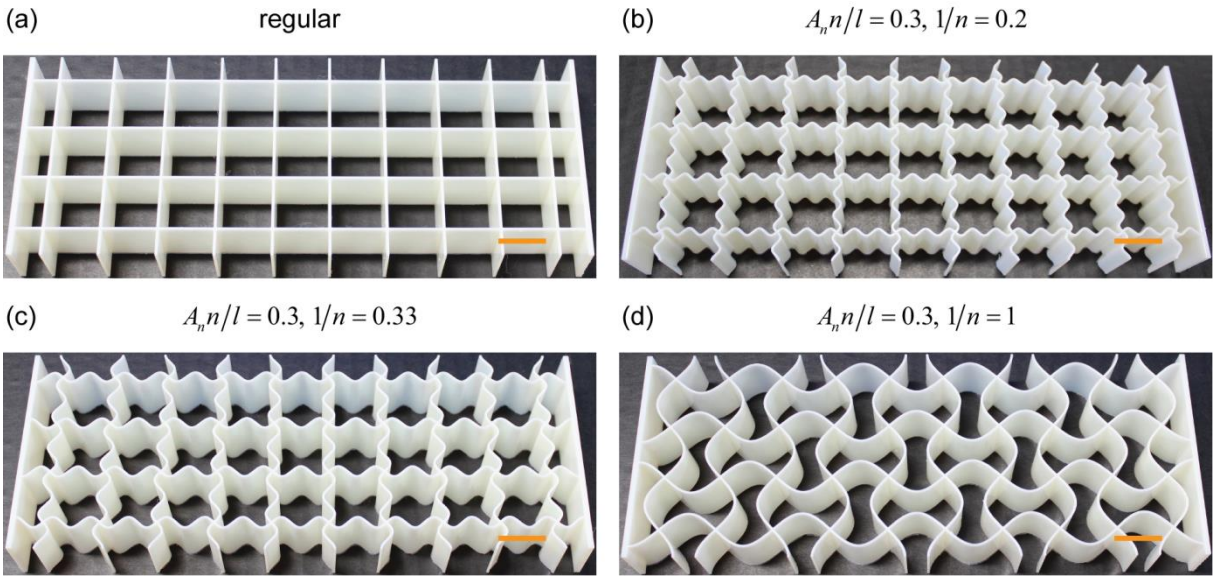

Figure 7.3 3D printed samples with different same ligament wave amplitude but different wavelengths. (a) regular lattice materials, (b) $A_n n/l = 0.30$, $1/n$=0.2, (c) $A_n n/l = 0.30$, $1/n$=0.33, and (d) $A_n n/l = 0.30$, $1/n$=1. The out-of-the-plane thickness is 2.5 cm. Scale bar: 2 cm.

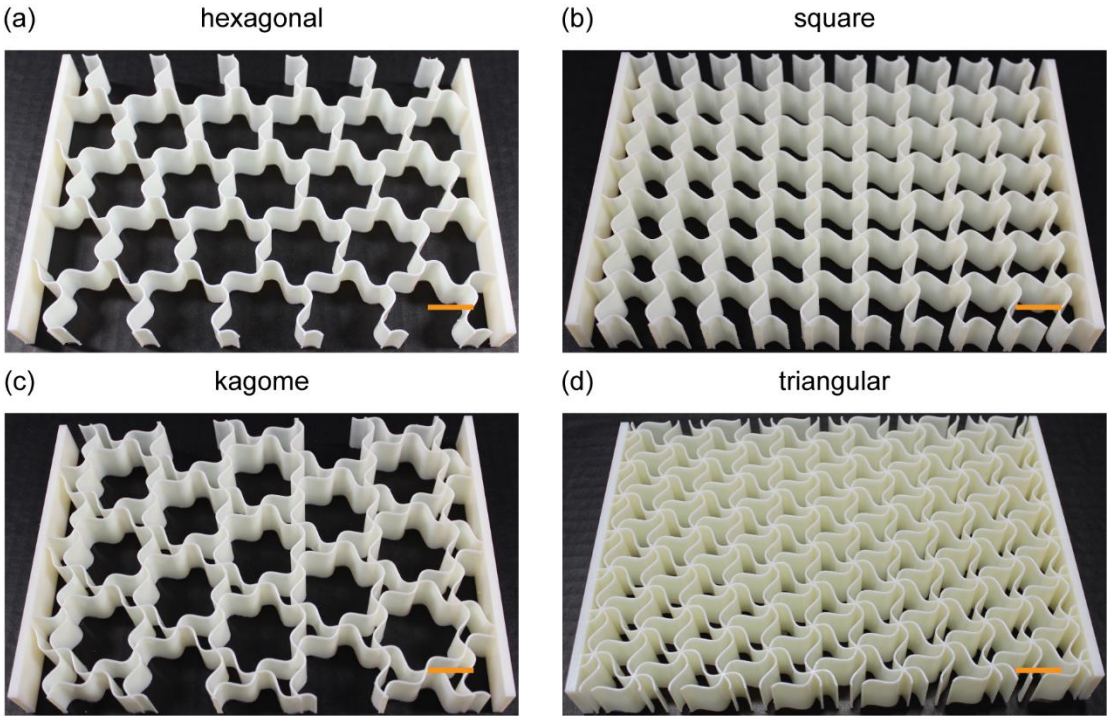

Figure 7.4 3D printed samples with different topologies. (a) Hexagonal, (b) square, (c) kagome, and (d) triangular. Here each ligament has a wave amplitude of $A_n n/l = 0.30$ and a wavelength of $1/n = 0.5$. The out-of-the-plane thickness is 2.5 cm. Scale bar: 2 cm.

7.3 Results and discussions

7.3.1 Broadband and multiband features of lattice metamaterials

We first focus on lattice metamaterials with a square topology and investigate the effect of the ligament wavelength on the dispersion relations by using the commercial finite element package COMSOL Multiphysics (See Chapter 2 for details about the numerical simulation) [59, 60, 199]. Figure 7.5 (a) displays the phononic dispersion relations for a regular lattice material and lattice metamaterials with the same ligament amplitude ($A_n n/l = 0.3$) but different ligament wavelengths ($1/n$ =0.2 and 1). For the regular lattice material, no phononic band gaps can be observed, indicating that the elastic wave can freely propagate through the medium. These results agree with previous studies on wave propagation in conventional lattice materials. [133] By contrast, five complete band gaps emerge in the lattice metamaterial with a wavelength $1/n = 0.2$. When the ligament wavelength increases to $1/n = 1$, the width of the observed band gaps become smaller, or even tend to disappear – but still, three complete wave band gaps exist.

From a physical point of view, the formation of phononic band gaps can be attributed to Bragg scatterings and/or local resonances. [22, 200-202] To gain insight into the fundamental mechanisms that govern the formation of the band gaps, we report in Figure 7.5 (b) the Bloch mode shapes at the high symmetry points **M** and **K** of the band edge (red line). In the case of a regular lattice material, the eigenmodes assume a global mode behavior that facilitates the travel

of the phonons through the structure. By contrast, the eigenmodes corresponding to the lattice metamaterial with $1/n$ =0.2 and 1 being invested by wavenumber vectors directed to the **M** and **K** points show a strong localization behavior around the nodes. As a result, the energy associated with the propagating wave is trapped and localized in the lattice metamaterials, suggesting that broad omnidirectional band gaps are induced by local resonances. Further evidence of this omnidirectional band gap presence is also highlighted by the flatness of the red band edge, which indicates a nearly zero group velocity. [78, 203, 204]

Low-frequency band gaps can be also be observed in the lattice metamaterial with $1/n$ =1. To quantitatively understand the mechanisms responsible for these band gaps formation, we compare the effective wavelength with its structural periodicity. The effective Young's modulus and Poisson's ratio for the lattice metamaterials with $1/n$ =1 can be obtained by following a finite element procedure, [205] which are 0.469 MPa and -0.65, respectively. Then, the transverse wave velocity for this lattice metamaterial can be calculated as $c_t = \sqrt{\mu^*/\rho^*}$, where μ^* and ρ^* are the effective shear modulus and effective density, respectively. As a result, the estimated transverse velocities for $1/n$ = 1 is 76.2 m s^{-1}. At the middle frequency of the lowest band gap, the effective wavelength is 3.75 cm, which is the same magnitude as the structural periodicity 4.5 cm. That means Bragg scattering is responsible for the low-frequency band gaps of lattice metamaterial with $1/n$ = 1.

Our simulations and analyses indicate that the broadband and multiband features are due to the coexisting of two different mechanisms, i.e., local resonances and Bragg scattering. Intrinsically, the broad and multiple band gaps in the lattice metamaterials are dictated by the rational design of the ligament, which favors the coupling of the axial and bending motion. [206]

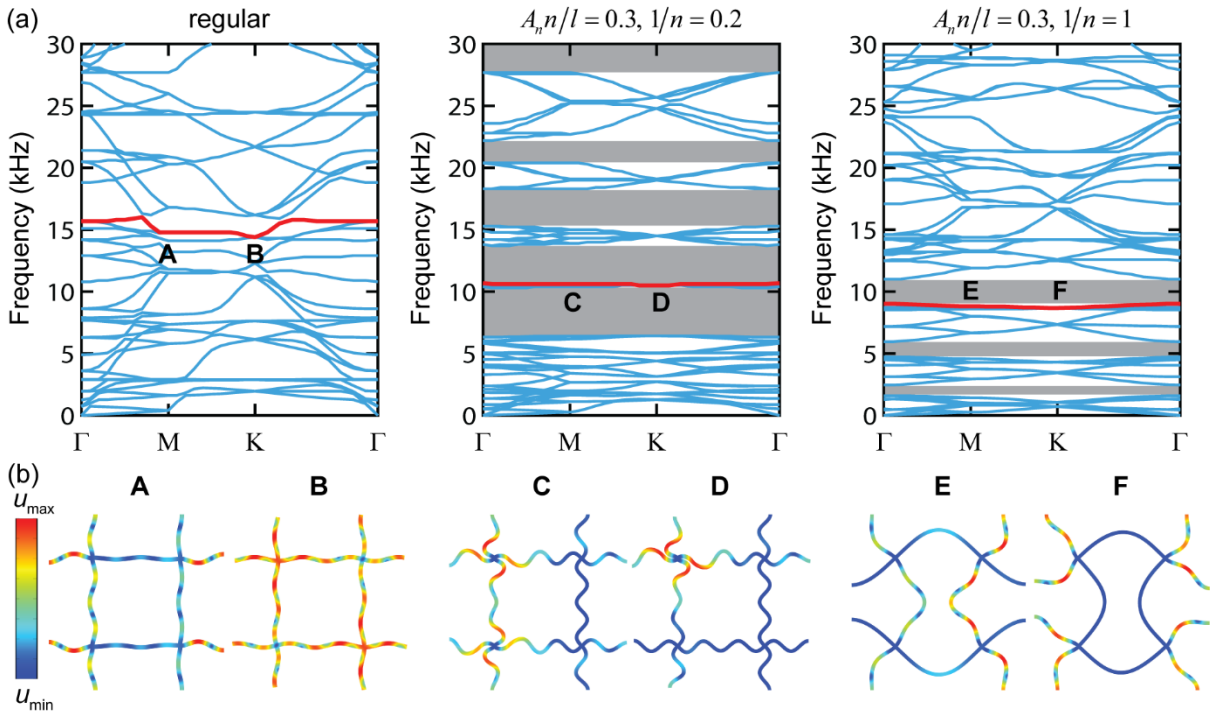

Figure 7.5 Dispersion relations and eigenmodes of regular lattices and the proposed lattice metamaterials. (a) Dispersion relations for regular lattice material and lattice metamaterials with $A_n n/l = 0.3$, $1/n$ =0.2 and 1. (b) Eigenmodes at high-symmetry points of the first irreducible Brillouin zone. The gray-shaded regions indicate the phononic band gaps.

7.3.2 Low amplitude wave transmission test

* *This experiment was conducted by my collaborator Feng Qian in Prof. Lei Zuo's lab at VT*

To validate the predictions of our models we have fabricated by 3D printing both regular lattices and lattice metamaterials with ligament amplitude $A_n n/l = 0.3$ and wavelength $1/n$ =0.2, 0.33 and 1 (Figure 7.3 and Figure 7.6 (a)). Each sample consisted of 2×5 unit cells and was made of Verowhite (Stratasys, Ltd). We have then performed low amplitude elastic wave transmission tests by exciting the 3D printed samples with an impact hammer (Figure 7.6 (b)-(c)). For details about the fabrication and experimental activity, the reader is referred to Chapter 2. The transmission is

computed as the ratio of output acceleration amplitude (*a*) to the input force amplitude (*F*). For the purpose of comparison, similar frequency domain analyses are also performed via numerical simulation to represent the wave propagation in finite-size structures (See Chapter 2 for details of the numerical simulation). [62, 203]

Figure 7.6 (d)-(g) Transmission spectra of regular lattice material and lattice metamaterials with $1/n = 0.2$, 0.33, and 1, respectively. In the simulated transmission spectrum of the regular lattice material, one can observe several transmission dips that correspond to partial band gaps along **M**-**K** direction (Figure 7.5 (a)). In the transmission spectra of the lattice metamaterials, we notice the presence of attenuation zones that agree extremely well with the simulated phononic band gaps in the dispersion relations (Figure 7.5 (a)). By comparing the measured transmission spectra with the predictions from the model we notice that simulated attenuation zones can be identified within the measured transmission spectra. For lattice metamaterials with $1/n = 1$, a quantitative agreement for the transmissibility values can be observed for the partial band gaps within 1.44 kHz - 2.94 kHz. A predicted partial band gap between 15 kHz and 19 kHz (along **M**-**K** direction, gray-shaded region) can be clearly seen for lattice metamaterials with $1/n = 0.2$. To better understand the wave propagation in the lattice metamaterials we plot in Figure 7.7 the dynamic response of the metamaterials under harmonic excitation inside and outside the band gaps. For both lattice metamaterials, the incident plane waves inside the band gaps decay rapidly, whereas incident waves can travel through the metamaterials when the excitation frequency lies outside the band gaps.

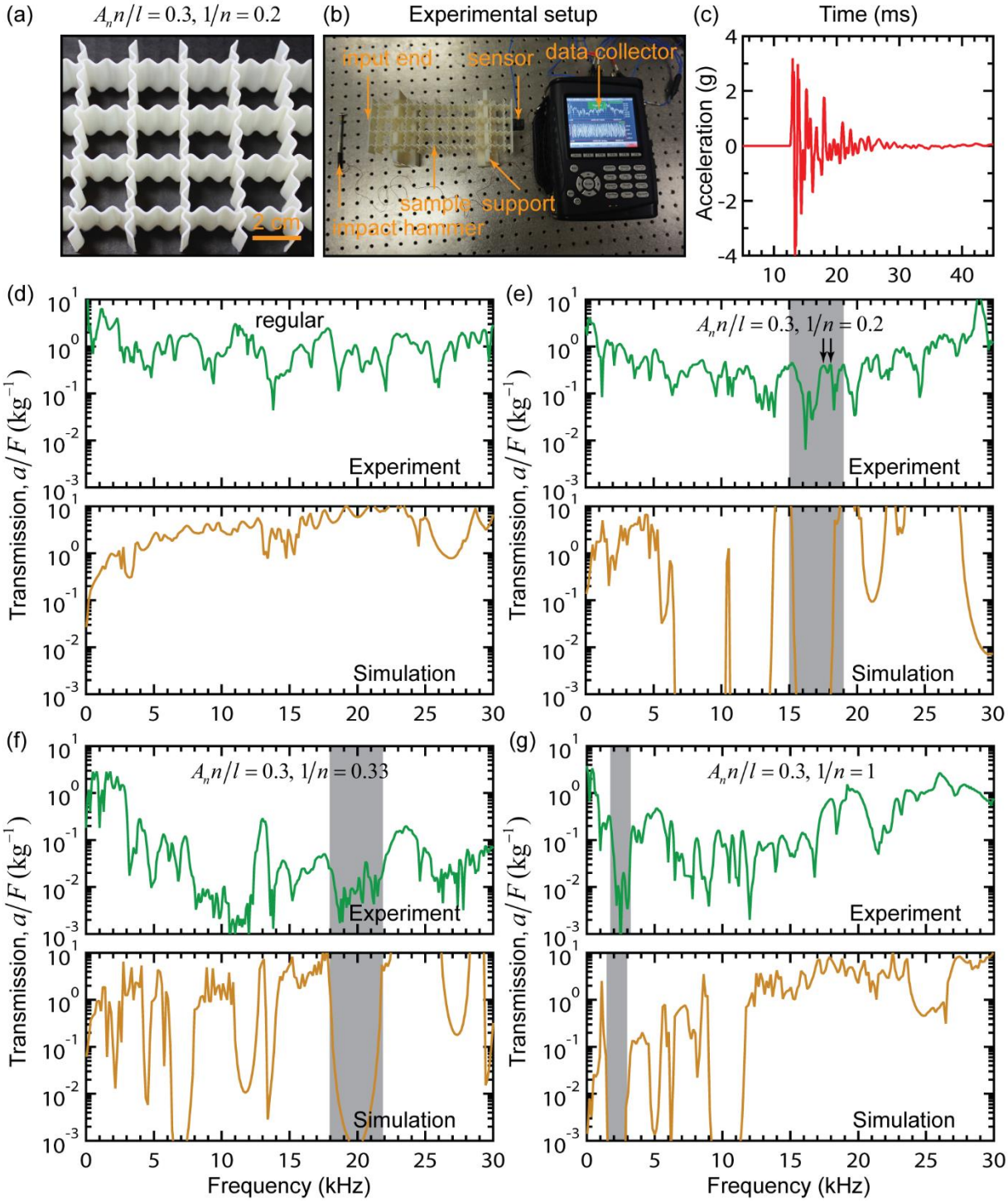

Figure 7.6 Low amplitude wave transmission test of the lattice metamaterials along the **M-K** direction. (a) 3D printed samples with $A_n n/l = 0.3$, $1/n = 0.2$. (b) Experimental setup of the transmission test. (c) Measured acceleration time curve for 3D printed samples with $A_n n/l = 0.3$,

$1/n = 0.2$. (d)-(g) Comparison between measured and simulated transmission spectra for lattice metamaterials with different wavelengths.

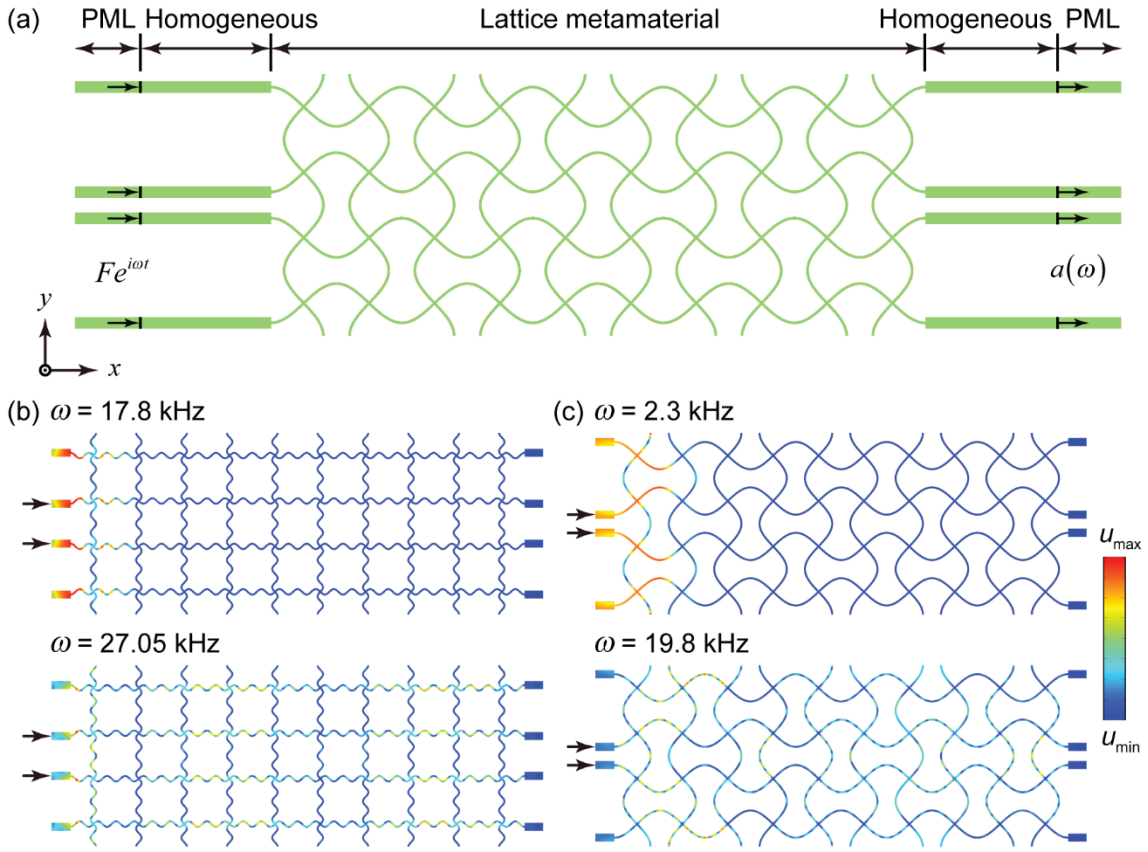

Figure 7.7 Frequency domain analysis for low amplitude wave transmission. (a) FE model (See Chapter 2 for details). (b)-(c) Dynamic response of the lattice metamaterials at a frequency inside and outside the band gaps for lattice metamaterials with $A_n n/l = 0.3$, $1/n = 0.2$ and $A_n n/l = 0.3$, $1/n = 1$.

It is noticeable that the simulated partial band gaps over the whole sweeping frequency range cannot be perfectly captured using the transmission test. For example, the simulated partial band gap for the lattice metamaterial with $1/n = 0.2$ is between 15 kHz and 19 kHz, while transmission peaks arise in the measured transmission spectra for the same frequency range (black arrows). This

discrepancy could be associated with one, or a combination of the following factors: 1) Boundary conditions. In the simulation, we use perfectly matched layers to prevent reflections by the scattering waves from the domain boundaries, while this virtual boundary condition cannot be realized in a lab environment. 2) Out-of-the-plane vibration. In our simulations, the plane strain condition is adopted for the lattice metamaterials. Out-of-the-plane vibration could, however, exist in the finite-thickness lattice metamaterials. 3) Damping effect. Most of the polymers for 3D printing have a significant damping effect, [207] which could attenuate the response and minimize the effect of the phononic band gaps. Our modeling neglects the presence of the viscoelasticity of the polymer and the adoption of structural and hysteretic damping. Notwithstanding these limitations, the low amplitude wave transmission test of the finite-size lattice metamaterials is able to indicate the presence of the broadband and multiband absorption feature.

7.3.3 Effects of the ligament geometry on the vibration control

We have numerically and experimentally demonstrated that broad and multiple band gaps can be obtained in the proposed lattice metamaterials. This remarkable vibration control capability is intrinsically dictated by the artificially architected ligament with a curved shape. We then systematically investigate the effects of the geometric features of the curved beam, i.e., $A_n n/l$ and $1/n$, over the band gap properties. To this end, we define two indicators to characterize the broadband and multiband features: the maximum relative band gaps $\left(\Delta\omega/\omega_*\right)_{\max}$ and the total relative band gaps $\sum\left(\Delta\omega/\omega_*\right)$. The two metrics are defined by $\Delta\omega$ (band gap width) and the midgap frequency ω_*. [199] Figures 7.8 (a) and (b) show the evolution of the maximum band gap and total band gaps as a function of the geometric features. For a given ligament wavelength both broad and multiple band gaps increase proportionally to the ligament wave amplitude. For

extremely small ligament amplitudes ($A_n n/l = 0.05$), no complete band gaps can be observed (Figure 7.8 (c)). This is expected since no complete band gaps exist in regular lattice materials with square topology. It is also noticeable that the broad and multiple band gaps arise in lattice metamaterials with the largest wave amplitude and a wavelength range from 0.4 to 0.8 (Figure 7.8 (d)).

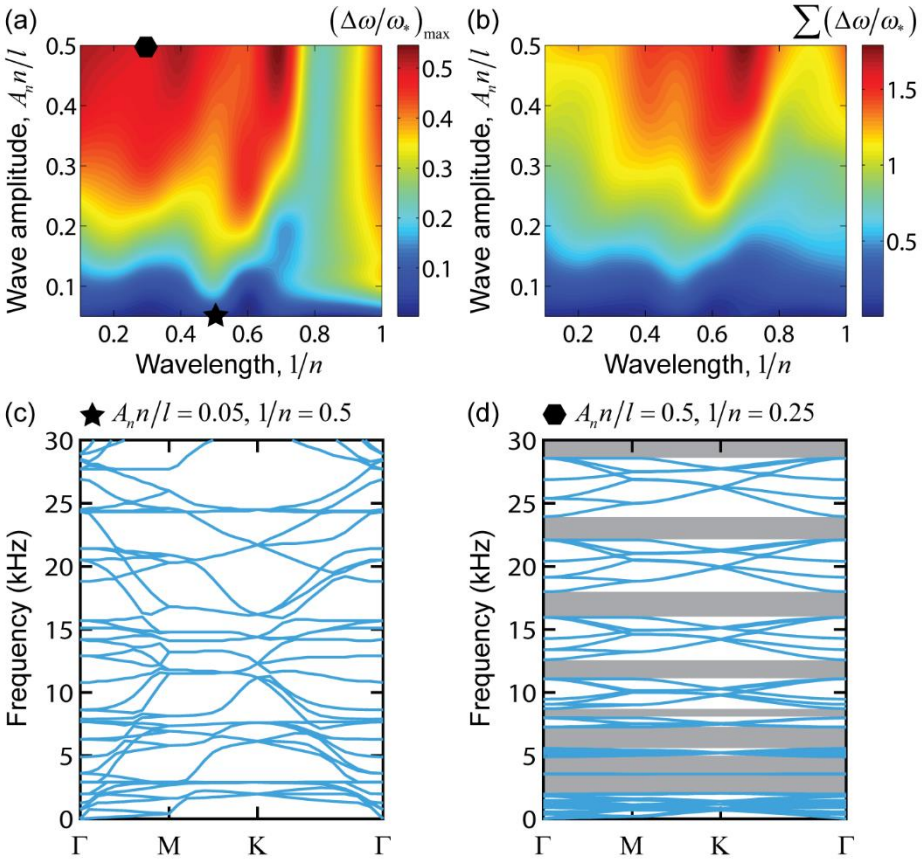

Figure 7.8 Effects of the ligament geometry on the phononic band gaps. (a)-(b) Effects of the wavelength and wave amplitude on the evolution of the maximum and full band gaps. (c)-(d) Dispersion relations for the lattice metamaterials with two extreme ligament amplitudes, $A_n n/l = 0.05$, $1/n = 0.5$ and $A_n n/l = 0.5$, $1/n = 0.25$.

Another geometric parameter of interest is the beam slenderness ratio, which dictates the deformation behavior of the ligament. Here for simplicity, we use l/t to examine the effect of slenderness ratio on the band gap property. Figure 7.9 (a)-(b) show the evolution of the maximum and total band gaps as a function of l/t for lattice metamaterials with $1/n = 0.25$ and $1/n = 0.5$. For the purpose of the comparison, the evolution of the band gaps related to regular lattice materials with different slenderness ratios is also presented. As expected, no complete or small band gaps can be observed in the regular lattice materials. By contrast, for lattice metamaterials with different wavelengths, broad and multiple band gaps can be observed. Specifically, for the lattice metamaterial with $1/n = 0.25$, an optimal maximum band gap is observed for a $l/t = 10$, while for lattice metamaterials with $1/n = 0.5$, the maximum band gap is proportional to l/t (Figure 7.9 (c) and (d)). It is also interesting to notice that the higher the waviness, the higher is the maximum band gap, especially for *l/t* lower than 30. High waviness (1/*n*=0.25 in this case) allows obtaining maximum band gaps even at relatively low slenderness ratios, for which shear deformation of the cross section becomes more important. On the contrary, lower waviness metamaterials tend to feature low maximum band gaps for thicker ligaments. In the case of the total band gaps, it is evident the direct proportionality with increasing values of *l/t*, although the amount of the total band gap tend to plateau for very high ligaments slenderness. The relative density of lattice materials is inversely proportional to the slenderness ratio, [208] and this indicates that the proposed lattice metamaterials not only exhibit broad and multiple band gap features but are also lightweight.

These systematic investigations reveal that the geometric features of the curved ligaments (amplitude, wavelength, and slenderness ratio) are critical to the formation of band gaps. Although

we have not built any analytical relation between these geometric features with the band gap properties of the lattice metamaterials, it is evident that the geometry uniquely dictates the deformation behavior and the vibrational modes of the artificially designed ligament. Quite importantly, these parameters can be tailored to design lattice metamaterials with desired or optimized vibration control capability.

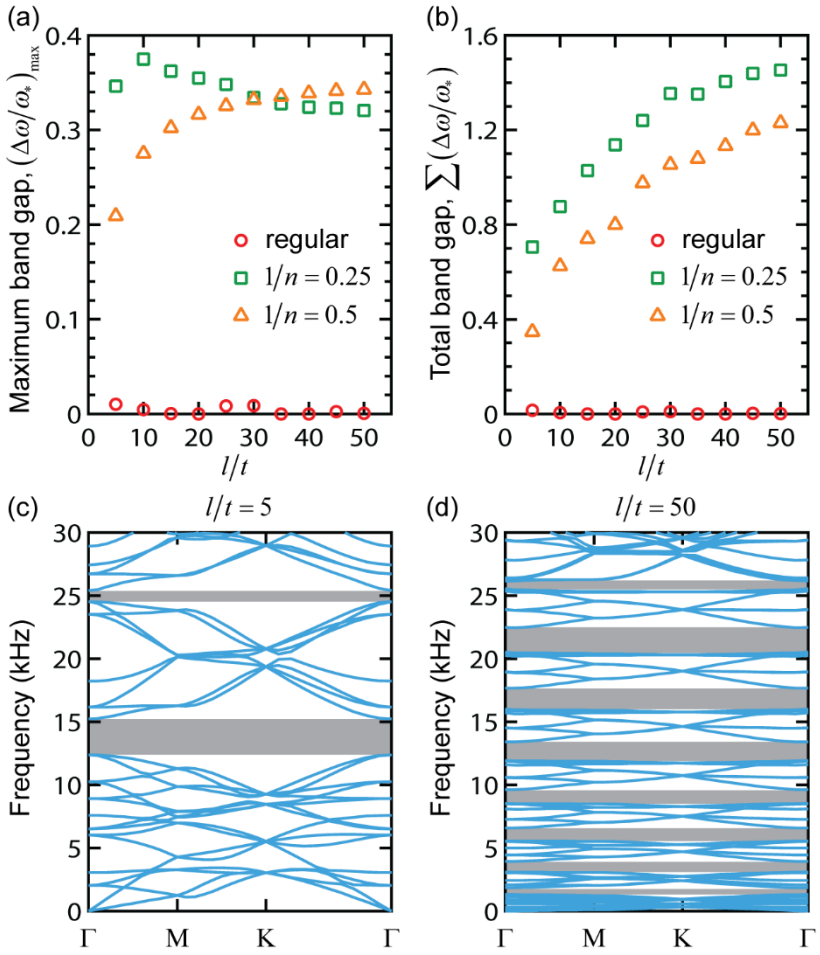

Figure 7.9 Effect of the slenderness of the ligament on the evolution of the phononic band gaps. (a)-(b) Evolution of the maximum and total band gaps with respect to the ligament slenderness l/t. (c)-(d) Dispersion relations for the lattice metamaterials with extreme slenderness, $l/t = 5$ and $l/t = 50$. Here $A_n/l = 0.30$ and $1/n = 0.5$.

7.3.4 Metamaterial design concept for other topologies

While the results reported so far are focused on lattice metamaterials with a square topology, we now proceed to demonstrate that the proposed lattice metamaterial design is not restricted to this specific topology only, and can be extended to lattice metamaterials with other shapes. Due to the geometric constraints in triangular lattice metamaterials and for the purpose of comparison, here we focus on lattice metamaterials with even numbers of half sinusoid, i.e., n=2 and 4. We first report the simulated dispersion relations for lattice metamaterials with different topologies on the left-hand side of Figure 7.10 (a)-(b). As expected, broad and multiple band gaps persist in each lattice metamaterials defined by different topologies, giving evidence that this design concept is general and robust. We further compare the maximum and total band gaps for lattice metamaterials with different topologies and different wavelengths (Figure 7.10 (c)-(d)). It can be seen that both maximum and total band gaps for lattice metamaterials are larger than those of regular lattice materials.

To validate the numerical predictions, low amplitude wave transmission tests along the **M**-**K** direction are performed on 3D printed lattice metamaterials with hexagonal, square, kagome, and triangular topologies (Figure 7.11 (a) and Figure 7.4). It is worth noticing the very good agreement with the measured transmission spectra, especially at low frequencies. By using the sinusoidally-shaped ligament microstructure topology one can seize new opportunities to design metamaterial systems that can integrate geometric features at different microstructural levels, i.e., the architecture of the ligament and the topology of the lattice metamaterials.

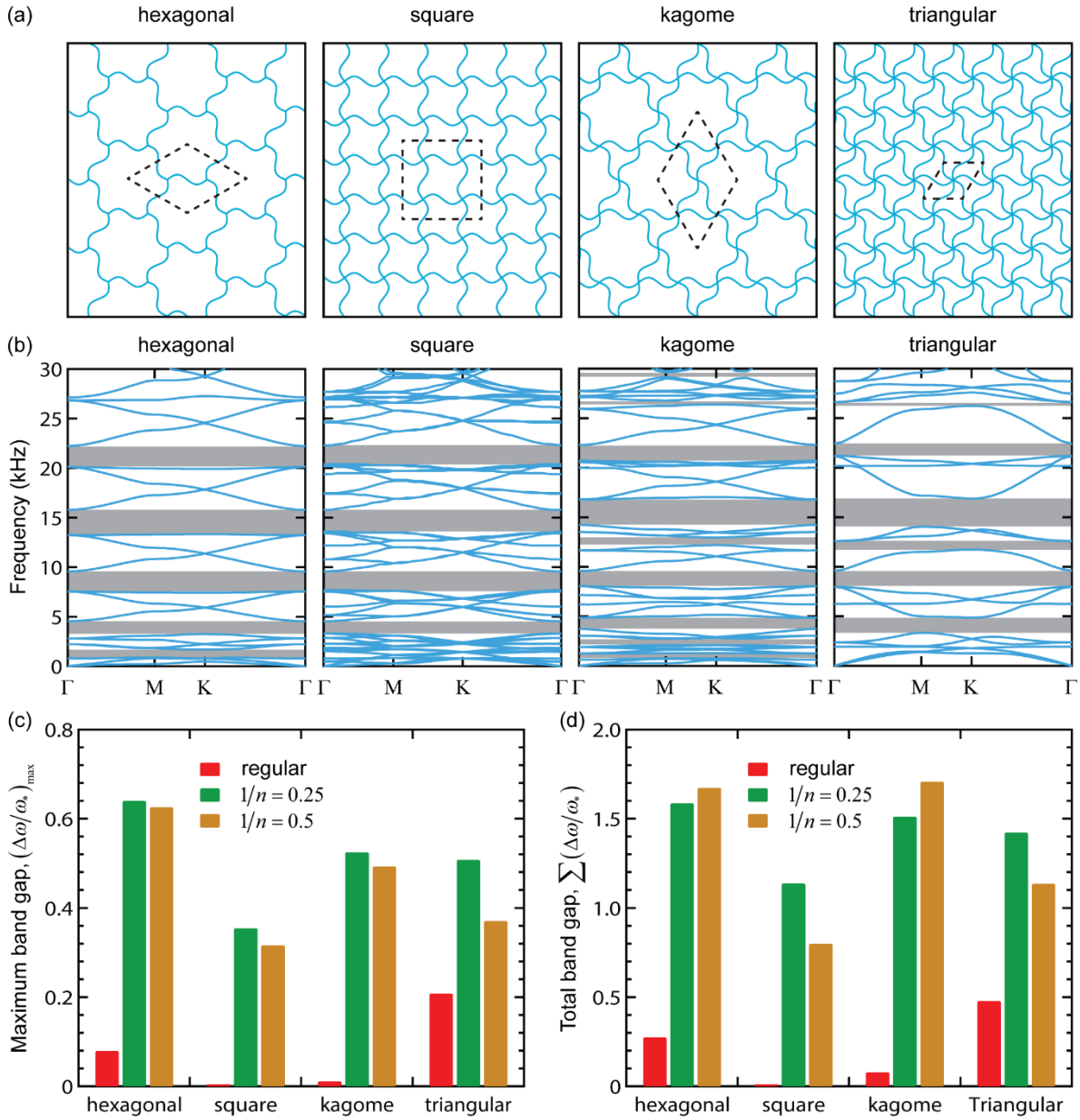

Figure 7.10 Effect of lattice topology on phononic band gaps. (a) Schematics of lattice metamaterials with hexagonal, square, kagome, and triangular topologies, respectively. The area surrounded by the dash lines is the representative unit cell for each topology. (b) Dispersion relations for lattice metamaterials with hexagonal, square, kagome, and triangular topologies. Here each ligament has a wave amplitude of $A_n/l = 0.30$ and wavelength of $1/n = 0.5$. (c)-(d) Maximum band gap and total band gaps for lattice metamaterials with hexagonal, square, kagome,

and triangular topologies. Here each ligament has a wave amplitude of $A_n n/l = 0.30$ but different wavelengths.

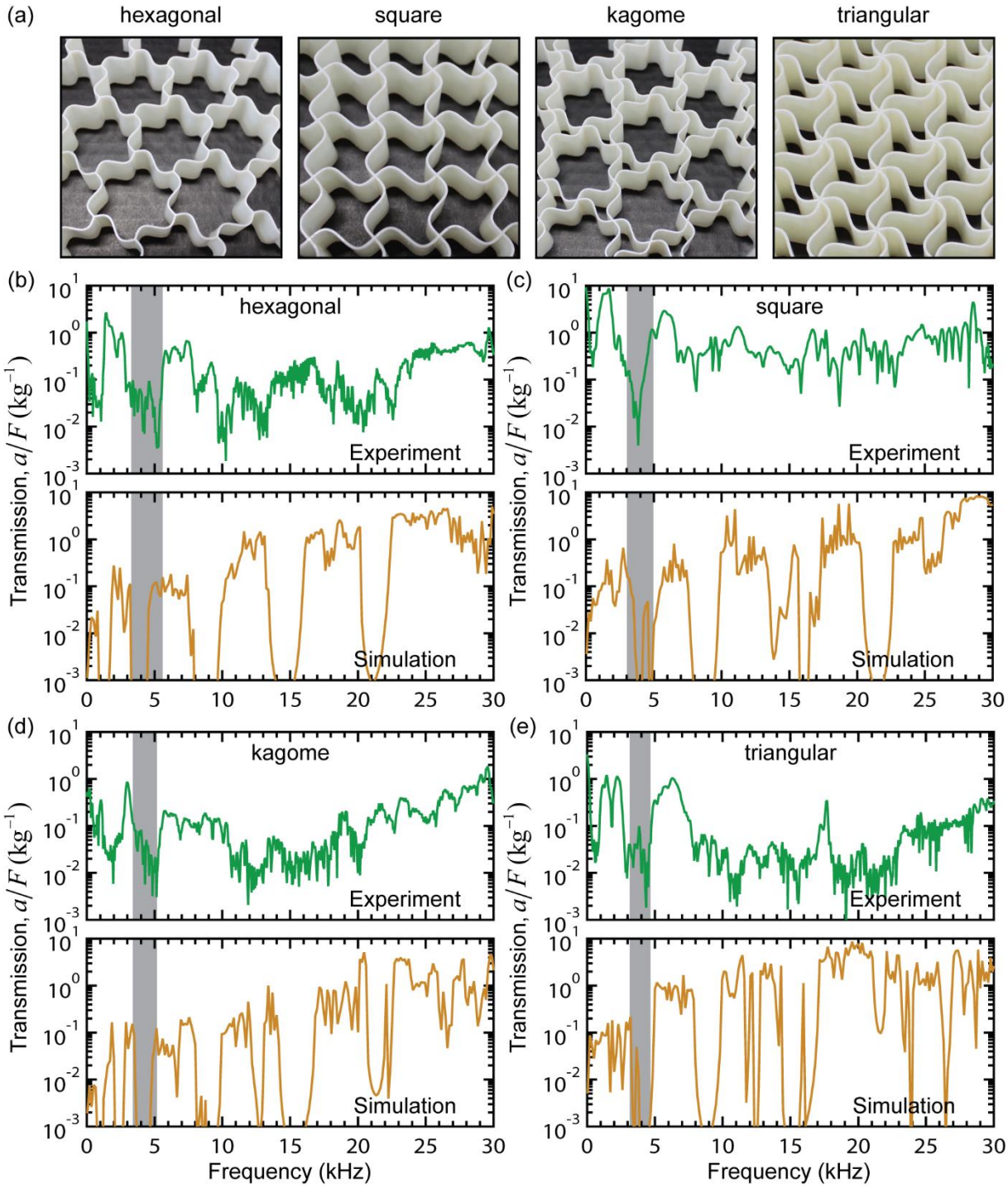

Figure 7.11 Wave transmission test of the lattice metamaterials with different topologies along the **M-K** direction. (a) 3D printed lattice metamaterials with hexagonal, square, kagome, and triangular topologies. (b)-(e) Comparison between measured and simulated transmission spectra for lattice metamaterials with different topologies. Here each ligament has a wave amplitude of $A_n n/l = 0.30$ and wavelength of $1/n = 0.5$ The out-of-the-plane thickness of each lattice metamaterial is 2.5 cm.

7.4 Conclusions

We have proposed and demonstrated the existence of a new class of lattice metamaterials consisting of curved ligaments that possess both broad and multiple phononic band gaps. These remarkable band gap properties are intrinsically controlled by the unique vibration behavior of the artificially designed ligaments. Moreover, our results indicate that the proposed metamaterial design concept not only works for a wide range of geometric parameters of the curved ligaments, but can also be extended to other topologies. Unlike conventional phononic crystals with multiple elastic phases, the broad and multiple band gap properties of the lattice metamaterials proposed in this work are material-independent, which indicates that a coupled material-architecture design strategy is not essential. Furthermore, the proposed metamaterial design concept is scale-independent and can be applied to various length scales. Due to the frequency range limitation of our vibration transmissibility test, we have fabricated samples with a ligament length of 2.25 cm and made of Verowhite polymer as demonstrators. Similar phononic band gap properties within different frequency ranges can be however envisioned for lattice metamaterials at various length scales. Finally, the pre-registered deformation in the architected ligaments can be harnessed to tailor the band gap properties. The curved ligaments have excellent stretchability under tension because the local strain is much smaller than the macroscopic one when the lattice metamaterials

are subjected to uniaxial stretching. As a result, the external mechanical stimulus of low magnitude could be further imposed to dynamically tune the band gaps. The metamaterial design concept proposed here provide new insights into the development of architected metamaterials with a broad range of potential applications, such as wave filtering, waveguiding, programmable acoustic metamaterials, vibration isolation, as well as stretchable electronics.

CHAPTER 8. CONCLUSIONS

8.1 Main contributions

The research work presented from Chapter 2 to 7 are focused on designing, modeling, 3D printing, and mechanical testing of architected metamaterials. The objective is to achieve broadband and multiband wave filtering and waveguiding capabilities by rationally designing the architectures of metamaterials. In addition, tunability of the vibration mitigation using external stimuli is also investigated. Besides the prominent wave control capability, the proposed architected metamaterials also exhibit excellent mechanical performance. The key scientific contributions are summarized as follows:

(1) Discovered the overlapping of Bragg scattering and local resonance band gaps in 3D co-continuous metamaterials. Conventionally, the complete wave band gaps formation are attributed to Bragg scattering or local resonances. However, in Chapter 3, it is numerically demonstrated that these two different mechanisms can overlap with each other. As a result, a relative large complete wave band gaps can be achieved, compared with pure locally resonant band gaps. This mechanism can be employed to design phononic crystals and acoustic metamaterials with improved wave filtering capability. In addition to the novel physical mechanism, the co-continuous metamaterials reported in Chapter 3 also have excellent mechanical properties, such as enhanced strength, stiffness, energy absorption, and fracture toughness. This is due to the mutual constrain between two phases in the co-continuous architectures when subjected to external loading. The 3D co-continuous metamaterials reported here will be particular useful in mechanically challenging environments where vibration mitigation and mechanical robustness are

simultaneously pursued. For example, the anechoic tiles of submarine are often damaged after years of service in mechanically challenging environments. This causes significant adverse economic consequence. With the development of high performance multifunctional metamaterials, such as the co-continuous composites proposed in this work, it is anticipated that the simultaneous load-carrying capability and vibration control capability can be achieved.

(2) Developed 2D bioinspired composites for broadband and multiband vibration control. Mechanical performance of nacreous composites under static loading conditions has been studied extensively. For example, it has been numerically and experimentally demonstrated that nacreous composites with brick-and-mortar-like microstructure enable an unusual combination of strength, stiffness, and fracture toughness. However, little attention has been paid to their mechanical response under dynamic loading conditions. In Chapter 4, the vibration mitigation capability is numerically demonstrated in 2D bioinspired composites. The broadband and multiband wave filtering capabilities in the proposed architected metamaterials are due to the coexisting of Bragg-type band gaps and locally resonant band gaps. In addition to the brick-and-mortar-like microstructure in nacreous biological composites, other geometric properties such as hierarchy and heterogeneity also play a significant role in manipulating wave propagation. Specifically, both heterogeneity and hierarchy result in broad and multiple band gaps due to the coexisting of Bragg scattering and local resonances. This finding not only provides us clues to design broadband and multiband phononic crystals for noise and vibration control, but also shed lights on the shielding behavior of many structural biological materials. It can be envisioned that the proposed bioinspired architected composites have great potential applications in harsh environments where vibration sources are complex and need to be controlled selectively. Importantly, the bioinspired architected composites with optimal band gaps also exhibit considerable mechanical properties such as

stiffness and strength. As a result, they can also be employed in mechanical challenging environments.

(3) Created a new system of lightweight yet stiff hierarchical honeycomb metamaterials. In aerospace engineering, besides the excellent mechanical performance and vibration mitigation capability, lightweight is another criterion that limits the potential use of conventional materials. In this regard, lattice materials such as honeycombs are more efficient and widely deployed in aerospace engineering. Recently, there are growing efforts to use honeycombs to control noise and vibration. Unfortunately, no complete band gaps are observed, no matter how the geometric features are modified. In Chapter 5, a new system of lightweight yet stiff hierarchical honeycomb metamaterials were created. The proposed architected honeycomb metamaterials are inspired by the most famous hierarchical architecture, Eiffel tower. It was numerically demonstrated that by introducing structural hierarchy into regular honeycombs, broad and multiple band gaps emerge in the hierarchical honeycombs. More important, the proposed hierarchical honeycombs exhibit improved mechanical performance. For example, kagome and triangular hierarchical honeycombs can achieve specific stiffness that is 40~60 times higher while having similar band gaps. Therefore, the created hierarchical honeycombs are promising for various applications including underwater wave mitigation in submarines and other structural vibration mitigation in defense, aerospace, and automotive industries. For example, acoustic liners are often designed and placed around the jet engine to absorb the undesired noise and vibration. It is highly possible to employ the proposed hierarchical honeycombs to replace these acoustic liners. Moreover, a compact, lightweight, and mechanical robust design can be readily achieved.

(4) Developed a new group of stretchable lattice metamaterials with mechanically tunable vibration mitigation capability. Conventionally, complete band gaps can be tuned by tailoring

the inherent architectures and materials properties of compositions. However, once the designed structures are fabricated and installed in practice, it is impractical or not economic to tune the band gaps. In Chapter 6 and 7, a new group of stretchable lattice metamaterials were developed by replacing the regular straight beams with beams of sinusoidal shape. Improved stretchability is numerically and experimentally demonstrated due to the pre-existing deformed shape. Interestingly, the proposed lattice metamaterials also exhibit a negative Poisson's ratio, indicating that the metamaterials will expand under uniaxial stretch. The investigation into the interplay between the multiscale (ligament and cell) architecture and wave propagation shows that broad and multiple phononic band gaps can be achieved in these lattice materials. Quite importantly, this significant vibration mitigation capability can be dynamically tuned by an external mechanical stimulus, i.e., a uniaxial stretching. Intrinsically, these novel mechanical behavior and vibration mitigation capability are attributed to the deformation pattern switching from bending-dominated to stretching-dominated behavior. The findings presented here provide new insights into the development of architected metamaterials with unusual physical properties and a broad range of potential applications, such as tunable particle filters and adjustable acoustic metamaterials for vibration control.

8.2 Broad impacts

The outcome of this research will generate crucial insights into the mechanisms governing the prominent vibration mitigation capability and mechanical robustness of architected metamaterials, thus providing scientific knowledge for the design and control of the multifunctional properties of this class of materials. It will provide fundamental knowledge of mechanics and physics to develop unified frameworks for integrated modeling, simulation, analytics, design, and validation of architected metamaterials for various applications. The seamless integration of finite element

analysis and advanced additive manufacturing technology enables systematic design and efficient realization of high-quality and high-throughput architected metamaterials. The combination of numerical and experimental studies in this work will provide a better scientific understanding of the interactions among multi-physics fields. The metamaterial design concepts and techniques for accurate modeling and testing reported here will not only be vital to the discovery and innovation of next-generation multifunctional metamaterials but also be beneficial to the computational science-based design activities that intersect multiple technical disciplines.

8.3 Future work

Architected metamaterial design concept is a powerful tool to explore novel and unusual physical properties. The designed architected metamaterials therefore have a wide range of promising applications, especially when design is combined with the modern manufacturing technologies like 3D printing. Some future works could be toward, but are not limited to, the following directions.

(1) Advanced fabricating techniques for hierarchical metamaterials. Conventional composites and lattice materials with feature size from centimeters to micrometers can be readily fabricated using additive manufacturing, such as 3D printing. However, for hierarchical structures, due to the multilevel of structure hierarchy, the overall size will be very large (~ meters) due to the resolution limitation at the lowest hierarchical level. Therefore, there is a great need for developing novel fabricating techniques that can fabricate prototypes over a wide range of length scale.

(2) Efficient modeling and optimization of architected metamaterials. The metamaterials reported here are designed based on previous experience, which could limit the current material design space. It has been shown that topology optimization is a powerful tool to design

metamaterials with multifunctionality. For example, recent study has shown that topology optimization can be used to optimize photonic/ phononic crystals with broad phononic band gaps. However, optimized hierarchical structures with multiple and broad band gaps have not been reported yet. In addition, material nonlinearity, geometric nonlinearity, and multifunctionalities are also a great challenge. Therefore, developing an integrated computational framework to optimize and model the noise and vibration control in hierarchical structures is still an open research area.

(3) Rational design of reconfigurable metamaterials. The architected lattice metamaterials studied in Chapter 6 & 7 have shown improved stretchability under uniaxial stretch. However, when the stretch reaches up 40%, failure of ligament arise due to highly localized stress. This indicates that the overall mechanical response of the architected lattice metamaterials is still material-dependent. It will be of great importance if the designed architected metamaterials have higher stretchability and can be repeatedly reconfigured without scarifying their load-carrying capability. In this regard, Kirigami could be one of the possible solutions. By cutting and folding the materials, one can achieve highly stretchable architected metamaterials in both 2D and 3D cases. Moreover, novel mechanical properties and functionalities can be explored.

(4) Multifunctional design of architected metamaterials. Conventional phononic crystals will redirect wave energy elsewhere, which could cause other undesired vibration or damage. While architected metamaterials exhibiting locally resonant effect will localize the wave energy. This energy could be transformed into other forms of energy, which could be stored for useful purposes. For example, the polymer materials in the architected composites or architected lattice materials can be replaced with a type of piezoelectric polymer, Polyvinylidene fluoride (PVDF). In this case, the localized wave energy could be transformed into electricity, and can be harnessed for other

use. Therefore, there is a great need for the careful design of electric circuit that can harvest the localized wave energy efficiently.

BIBLIOGRAPHY

[1]. T.T. Soong and M.C. Costantinou, *Passive and active structural vibration control in civil engineering*, Springer, 2014.

[2]. L.L. Beranek and I.L. Ver, Noise and vibration control engineering-principles and applications, *Noise and vibration control engineering-Principles and applications John Wiley & Sons, Inc., 814 p.* **1**, (1992).

[3]. C. Hansen, S. Snyder, X. Qiu, L. Brooks, and D. Moreau, *Active control of noise and vibration*, CRC Press, 2012.

[4]. C. Fuller and A. Von Flotow, Active control of sound and vibration, *IEEE Control systems* **15**, 9 (1995).

[5]. K. Williams, G. Chiu, and R. Bernhard, Adaptive-passive absorbers using shape-memory alloys, *Journal of Sound and Vibration* **249**, 835 (2002).

[6]. M. Franchek, M. Ryan, and R. Bernhard, Adaptive passive vibration control, *Journal of Sound and Vibration* **189**, 565 (1996).

[7]. Y. Tanaka, Y. Tomoyasu, and S.-i. Tamura, Band structure of acoustic waves in phononic lattices: Two-dimensional composites with large acoustic mismatch, *Physical Review B* **62**, 7387 (2000).

[8]. M. Kafesaki and E.N. Economou, Multiple-scattering theory for three-dimensional periodic acoustic composites, *Physical review B* **60**, 11993 (1999).

[9]. M.S. Kushwaha, P. Halevi, G. Martinez, L. Dobrzynski, and B. Djafari-Rouhani, Theory of acoustic band structure of periodic elastic composites, *Physical Review B* **49**, 2313 (1994).

[10]. M.S. Kushwaha, P. Halevi, L. Dobrzynski, and B. Djafari-Rouhani, Acoustic band structure of periodic elastic composites, *Physical Review Letters* **71**, 2022 (1993).

[11]. J.W.S.B. Rayleigh, *The theory of sound*, Macmillan, 1896.

[12]. M. Maldovan, Narrow low-frequency spectrum and heat management by thermocrystals, *Physical review letters* **110**, 025902 (2013).

[13]. G. Wang, D. Yu, J. Wen, Y. Liu, and X. Wen, One-dimensional phononic crystals with locally resonant structures, *Physics Letters A* **327**, 512 (2004).

[14]. T. Gorishnyy, C.K. Ullal, M. Maldovan, G. Fytas, and E. Thomas, Hypersonic phononic crystals, *Physical review letters* **94**, 115501 (2005).

[15]. M. Maldovan, Sound and heat revolutions in phononics, *Nature* **503**, 209 (2013).

[16]. M. Sigalas and E. Economou, Band structure of elastic waves in two dimensional systems, *Solid State Communications* **86**, 141 (1993).

[17]. R. Martinezsala, J. Sancho, J. Sánchez, V. Gómez, J. Llinares, and F. Meseguer, Sound-attenuation by sculpture, *nature* **378**, 241 (1995).

[18]. Y. Achaoui, A. Khelif, S. Benchabane, L. Robert, and V. Laude, Experimental observation of locally-resonant and Bragg band gaps for surface guided waves in a phononic crystal of pillars, *Physical Review B* **83**, 104201 (2011).

[19]. L. Liu and M.I. Hussein, Wave motion in periodic flexural beams and characterization of the transition between Bragg scattering and local resonance, *Journal of Applied Mechanics* **79**, 011003 (2012).

[20]. P.A. Deymier, *Acoustic metamaterials and phononic crystals*, Springer Science & Business Media, 2013.

[21]. D. Sutter-Widmer, S. Deloudi, and W. Steurer, Prediction of Bragg-scattering-induced band gaps in phononic quasicrystals, *Physical Review B* **75**, 094304 (2007).
[22]. Z. Liu, X. Zhang, Y. Mao, Y. Zhu, Z. Yang, C. Chan, and P. Sheng, Locally resonant sonic materials, *Science* **289**, 1734 (2000).
[23]. J.-C. Hsu, Local resonances-induced low-frequency band gaps in two-dimensional phononic crystal slabs with periodic stepped resonators, *Journal of Physics D: Applied Physics* **44**, 055401 (2011).
[24]. A. Khelif, Y. Achaoui, S. Benchabane, V. Laude, and B. Aoubiza, Locally resonant surface acoustic wave band gaps in a two-dimensional phononic crystal of pillars on a surface, *Physical Review B* **81**, 214303 (2010).
[25]. Y. Chen and L. Wang, Periodic co-continuous acoustic metamaterials with overlapping locally resonant and Bragg band gaps, *Applied Physics Letters* **105**, 191907 (2014).
[26]. Y. Pennec, B. Djafari-Rouhani, J. Vasseur, A. Khelif, and P. Deymier, Tunable filtering and demultiplexing in phononic crystals with hollow cylinders, *Physical Review E* **69**, 046608 (2004).
[27]. P. Zhang and A.C. To, Broadband wave filtering of bioinspired hierarchical phononic crystal, *Applied Physics Letters* **102**, 121910 (2013).
[28]. C.J. Rupp, M.L. Dunn, and K. Maute, Switchable phononic wave filtering, guiding, harvesting, and actuating in polarization-patterned piezoelectric solids, *Applied Physics Letters* **96**, 111902 (2010).
[29]. H. Chen and C.T. Chan, Acoustic cloaking and transformation acoustics, *Journal of Physics D: Applied Physics* **43**, 113001 (2010).
[30]. S.A. Cummer and D. Schurig, One path to acoustic cloaking, *New Journal of Physics* **9**, 45 (2007).
[31]. H. Chen and C. Chan, Acoustic cloaking in three dimensions using acoustic metamaterials, *Applied physics letters* **91**, 183518 (2007).
[32]. L. Yang, N. Yang, and B. Li, Extreme low thermal conductivity in nanoscale 3D Si phononic crystal with spherical pores, *Nano letters* **14**, 1734 (2014).
[33]. J.-K. Yu, S. Mitrovic, D. Tham, J. Varghese, and J.R. Heath, Reduction of thermal conductivity in phononic nanomesh structures, *Nature nanotechnology* **5**, 718 (2010).
[34]. L.-Y. Wu, L.-W. Chen, and C.-M. Liu, Acoustic energy harvesting using resonant cavity of a sonic crystal, *Applied Physics Letters* **95**, 013506 (2009).
[35]. H. Lv, X. Tian, M.Y. Wang, and D. Li, Vibration energy harvesting using a phononic crystal with point defect states, *Applied Physics Letters* **102**, 034103 (2013).
[36]. S. Gonella, A.C. To, and W.K. Liu, Interplay between phononic bandgaps and piezoelectric microstructures for energy harvesting, *Journal of the Mechanics and Physics of Solids* **57**, 621 (2009).
[37]. Z. Huang, Z. Pan, H. Li, Q. Wei, and X. Li, Hidden energy dissipation mechanism in nacre, *Journal of Materials Research* **29**, 1573 (2014).
[38]. H. Li, Y. Yue, X. Han, and X. Li, Plastic deformation enabled energy dissipation in a bionanowire structured armor, *Nano letters* **14**, 2578 (2014).
[39]. H. Yao, Z. Xie, C. He, and M. Dao, Fracture mode control: a bio-inspired strategy to combat catastrophic damage, *Scientific reports* **5**, (2015).
[40]. U.G. Wegst, H. Bai, E. Saiz, A.P. Tomsia, and R.O. Ritchie, Bioinspired structural materials, *Nature materials* **14**, 23 (2015).

[41]. L. Wang and M.C. Boyce, Bioinspired Structural Material Exhibiting Post-Yield Lateral Expansion and Volumetric Energy Dissipation During Tension, *Advanced Functional Materials* **20**, 3025 (2010).
[42]. M.A. Meyers, P.-Y. Chen, A.Y.-M. Lin, and Y. Seki, Biological materials: structure and mechanical properties, *Progress in Materials Science* **53**, 1 (2008).
[43]. P.-Y. Chen, A. Lin, Y.-S. Lin, Y. Seki, A. Stokes, J. Peyras, E. Olevsky, M. Meyers, and J. McKittrick, Structure and mechanical properties of selected biological materials, *Journal of the Mechanical Behavior of Biomedical Materials* **1**, 208 (2008).
[44]. F. Barthelat and D. Zhu, A novel biomimetic material duplicating the structure and mechanics of natural nacre, *Journal of Materials Research* **26**, 1203 (2011).
[45]. H. Qi, B. Bruet, J. Palmer, C. Ortiz, and M. Boyce (2006) Micromechanics and macromechanics of the tensile deformation of nacre. *Mechanics of Biological Tissue*, (Springer), pp 189.
[46]. R.M. Erb, R. Libanori, N. Rothfuchs, and A.R. Studart, Composites reinforced in three dimensions by using low magnetic fields, *Science* **335**, 199 (2012).
[47]. A.R. Studart, Towards High-Performance Bioinspired Composites, *Advanced Materials* **24**, 5024 (2012).
[48]. A.R. Studart, Biological and bioinspired composites with spatially tunable heterogeneous architectures, *Advanced Functional Materials* **23**, 4423 (2013).
[49]. H. Chai, J.J.-W. Lee, P.J. Constantino, P.W. Lucas, and B.R. Lawn, Remarkable resilience of teeth, *Proceedings of the National Academy of Sciences* **106**, 7289 (2009).
[50]. L. Han, L. Wang, J. Song, M.C. Boyce, and C. Ortiz, Direct quantification of the mechanical anisotropy and fracture of an individual exoskeleton layer via uniaxial compression of micropillars, *Nano letters* **11**, 3868 (2011).
[51]. B.J. Bruet, J. Song, M.C. Boyce, and C. Ortiz, Materials design principles of ancient fish armour, *Nature materials* **7**, 748 (2008).
[52]. L. Wang, J. Song, C. Ortiz, and M.C. Boyce, Anisotropic design of a multilayered biological exoskeleton, *Journal of Materials Research* **24**, 3477 (2009).
[53]. J. Song, C. Ortiz, and M.C. Boyce, Threat-protection mechanics of an armored fish, *Journal of the mechanical behavior of biomedical materials* **4**, 699 (2011).
[54]. L.R. Meza, A.J. Zelhofer, N. Clarke, A.J. Mateos, D.M. Kochmann, and J.R. Greer, Resilient 3D hierarchical architected metamaterials, *Proceedings of the National Academy of Sciences* **112**, 11502 (2015).
[55]. L.R. Meza, S. Das, and J.R. Greer, Strong, lightweight, and recoverable three-dimensional ceramic nanolattices, *Science* **345**, 1322 (2014).
[56]. R. Lakes, Materials with structural hierarchy, *Nature* **361**, 511 (1993).
[57]. N.-K. Kuo and G. Piazza, Fractal phononic crystals in aluminum nitride: An approach to ultra high frequency bandgaps, *Applied Physics Letters* **99**, 163501 (2011).
[58]. R.C. Norris, J.S. Hamel, and P. Nadeau, Phononic band gap crystals with periodic fractal inclusions: Theoretical study using numerical analysis, *Journal of Applied Physics* **103**, 104908 (2008).
[59]. M. Maldovan and E.L. Thomas, *Periodic materials and interference lithography: for photonics, phononics and mechanics*, John Wiley & Sons, 2009.
[60]. J. Achenbach, *Wave propagation in elastic solids*, Elsevier, 2012.
[61]. A. Khelif, B. Aoubiza, S. Mohammadi, A. Adibi, and V. Laude, Complete band gaps in two-dimensional phononic crystal slabs, *Physical Review E* **74**, 046610 (2006).

[62]. W. Chew and Q. Liu, Perfectly matched layers for elastodynamics: a new absorbing boundary condition, *Journal of Computational Acoustics* **4**, 341 (1996).
[63]. S. Babaee, J. Shim, J.C. Weaver, E.R. Chen, N. Patel, and K. Bertoldi, 3D soft metamaterials with negative Poisson's ratio, *Advanced Materials* **25**, 5044 (2013).
[64]. X. Hou, H. Hu, and V. Silberschmidt, A novel concept to develop composite structures with isotropic negative Poisson's ratio: Effects of random inclusions, *Composites Science and Technology* **72**, 1848 (2012).
[65]. J. Bauer, S. Hengsbach, I. Tesari, R. Schwaiger, and O. Kraft, High-strength cellular ceramic composites with 3D microarchitecture, *Proceedings of the National Academy of Sciences* **111**, 2453 (2014).
[66]. X. Zheng, H. Lee, T.H. Weisgraber, M. Shusteff, J. DeOtte, E.B. Duoss, J.D. Kuntz, M.M. Biener, Q. Ge, J.A. Jackson, S.O. Kucheyev, N.X. Fang, and C.M. Spadaccini, Ultralight, ultrastiff mechanical metamaterials, *Science* **344**, 1373 (2014).
[67]. T. Schaedler, A. Jacobsen, A. Torrents, A. Sorensen, J. Lian, J. Greer, L. Valdevit, and W. Carter, Ultralight metallic microlattices, *Science* **334**, 962 (2011).
[68]. D. Jang, L.R. Meza, F. Greer, and J.R. Greer, Fabrication and deformation of three-dimensional hollow ceramic nanostructures, *Nature materials* **12**, 893 (2013).
[69]. J.-H. Lee, L. Wang, S. Kooi, M.C. Boyce, and E.L. Thomas, Enhanced energy dissipation in periodic epoxy nanoframes, *Nano letters* **10**, 2592 (2010).
[70]. J.-H. Lee, L. Wang, M.C. Boyce, and E.L. Thomas, Periodic bicontinuous composites for high specific energy absorption, *Nano letters* **12**, 4392 (2012).
[71]. L. Wang, J. Lau, E.L. Thomas, and M.C. Boyce, Co-Continuous composite materials for stiffness, strength, and energy dissipation, *Advanced Materials* **23**, 1524 (2011).
[72]. Y. Ding, Z. Liu, C. Qiu, and J. Shi, Metamaterial with simultaneously negative bulk modulus and mass density, *Physical review letters* **99**, 093904 (2007).
[73]. J. Li and C. Chan, Double-negative acoustic metamaterial, *Physical Review E* **70**, 055602 (2004).
[74]. Y. Cheng, J. Xu, and X. Liu, One-dimensional structured ultrasonic metamaterials with simultaneously negative dynamic density and modulus, *Physical Review B* **77**, 045134 (2008).
[75]. X. Liu, G. Hu, G. Huang, and C. Sun, An elastic metamaterial with simultaneously negative mass density and bulk modulus, *Applied Physics Letters* **98**, 251907 (2011).
[76]. N. Fang, D. Xi, J. Xu, M. Ambati, W. Srituravanich, C. Sun, and X. Zhang, Ultrasonic metamaterials with negative modulus, *Nature materials* **5**, 452 (2006).
[77]. K.M. Ho, C.K. Cheng, Z. Yang, X. Zhang, and P. Sheng, Broadband locally resonant sonic shields, *Applied physics letters* **83**, 5566 (2003).
[78]. C. Goffaux and J. Sánchez-Dehesa, Two-dimensional phononic crystals studied using a variational method: Application to lattices of locally resonant materials, *Physical review B* **67**, 144301 (2003).
[79]. S. Zhang, C. Xia, and N. Fang, Broadband acoustic cloak for ultrasound waves, *Physical Review Letters* **106**, 024301 (2011).
[80]. H. Jiang and Y. Wang, Phononic glass: A robust acoustic-absorption material, *The Journal of the Acoustical Society of America* **132**, 694 (2012).
[81]. E. Baravelli and M. Ruzzene, Internally resonating lattices for bandgap generation and low-frequency vibration control, *Journal of Sound and Vibration* **332**, 6562 (2013).

[82]. D.R. Clarke, Interpenetrating phase composites, *Journal of the American Ceramic Society* **75**, 739 (1992).
[83]. M. Maldovan, C.K. Ullal, J.H. Jang, and E.L. Thomas, Sub-Micrometer Scale Periodic Porous Cellular Structures: Microframes Prepared by Holographic Interference Lithography, *Advanced Materials* **19**, 3809 (2007).
[84]. S. Torquato and A. Donev, Minimal surfaces and multifunctionality, *Proceedings of the Royal Society of London. Series A: Mathematical, Physical and Engineering Sciences* **460**, 1849 (2004).
[85]. C. Croënne, E. Lee, H. Hu, and J. Page, Band gaps in phononic crystals: Generation mechanisms and interaction effects, *AIP Adv* **1**, 041401 (2011).
[86]. Y. Chen and L. Wang, Tunable band gaps in bio-inspired periodic composites with nacre-like microstructure, *Journal of Applied Physics* **116**, 063506 (2014).
[87]. N. Kaina, M. Fink, and G. Lerosey, Composite media mixing Bragg and local resonances for highly attenuating and broad bandgaps, *Scientific reports* **3**, (2013).
[88]. O. Sigmund and J.S. Jensen, Systematic design of phononic band–gap materials and structures by topology optimization, *Philosophical Transactions of the Royal Society of London. Series A: Mathematical, Physical and Engineering Sciences* **361**, 1001 (2003).
[89]. L. Wang and K. Bertoldi, Mechanically tunable phononic band gaps in three-dimensional periodic elastomeric structures, *International Journal of Solids and Structures* **49**, 2881 (2012).
[90]. S. Bechtle, S.F. Ang, and G.A. Schneider, On the mechanical properties of hierarchically structured biological materials, *Biomaterials* **31**, 6378 (2010).
[91]. J. Sun and B. Bhushan, Hierarchical structure and mechanical properties of nacre: a review, *Rsc Advances* **2**, 7617 (2012).
[92]. Y. Oaki and H. Imai, The hierarchical architecture of nacre and its mimetic material, *Angewandte Chemie International Edition* **44**, 6571 (2005).
[93]. I.A. Aksay, M. Trau, S. Manne, I. Honma, N. Yao, L. Zhou, P. Fenter, P.M. Eisenberger, and S.M. Gruner, Biomimetic pathways for assembling inorganic thin films, *Science* **273**, 892 (1996).
[94]. F.D. Fleischli, M. Dietiker, C. Borgia, and R. Spolenak, The influence of internal length scales on mechanical properties in natural nanocomposites: a comparative study on inner layers of seashells, *Acta biomaterialia* **4**, 1694 (2008).
[95]. H.D. Espinosa, A.L. Juster, F.J. Latourte, O.Y. Loh, D. Gregoire, and P.D. Zavattieri, Tablet-level origin of toughening in abalone shells and translation to synthetic composite materials, *Nature communications* **2**, 173 (2011).
[96]. M. Kafesaki, M.M. Sigalas, and E.N. Economou, Elastic-Wave Band-Gaps in 3-D Periodic Polymer Matrix Composites, *Solid State Communications* **96**, 285 (1995).
[97]. E.N. Economou and M. Sigalas, Stop Bands for Elastic-Waves in Periodic Composite-Materials, *Journal of the Acoustical Society of America* **95**, 1734 (1994).
[98]. M.M. Sigalas and E.N. Economou, Elastic-Waves in Plates with Periodically Placed Inclusions, *Journal of Applied Physics* **75**, 2845 (1994).
[99]. P.F. Hsieh, T.T. Wu, and J.H. Sun, Three-dimensional phononic band gap calculations using the FDTD method and a PC cluster system, *Ieee Transactions on Ultrasonics Ferroelectrics and Frequency Control* **53**, 148 (2006).
[100]. P. Fratzl and R. Weinkamer, Nature's hierarchical materials, *Progress in Materials Science* **52**, 1263 (2007).

[101]. P. Zhang and A.C. To, Broadband wave filtering of bioinspired hierarchical phononic crystal, *Applied Physics Letters* **102**, 121910 (2013).
[102]. B. Ji and H. Gao, Mechanical properties of nanostructure of biological materials, *Journal of the Mechanics and Physics of Solids* **52**, 1963 (2004).
[103]. K. Bertoldi, D. Bigoni, and W. Drugan, Nacre: an orthotropic and bimodular elastic material, *Composites Science and Technology* **68**, 1363 (2008).
[104]. S. Dashkovskiy, B. Suhr, K. Tushtev, and G. Grathwohl, Nacre properties in the elastic range: Influence of matrix incompressibility, *Computational Materials Science* **41**, 96 (2007).
[105]. R. Wang, Z. Suo, A. Evans, N. Yao, and I. Aksay, Deformation mechanisms in nacre, *Journal of Materials Research* **16**, 2485 (2001).
[106]. F. Barthelat, C.-M. Li, C. Comi, and H.D. Espinosa, Mechanical properties of nacre constituents and their impact on mechanical performance, *Journal of Materials Research* **21**, 1977 (2006).
[107]. H. Yao and H. Gao, Reprint of "Multi-scale cohesive laws in hierarchical materials"[In. J. Solids Struct. 44 (2007) 8177–8193], *International Journal of Solids and Structures* **45**, 3627 (2008).
[108]. D. Sen and M.J. Buehler, Structural hierarchies define toughness and defect-tolerance despite simple and mechanically inferior brittle building blocks, *Scientific reports* **1**, (2011).
[109]. I. Aksay, M. Trau, S. Manne, and I. Honma, Biomimetic pathways for assembling inorganic thin films, *Science* **273**, 892 (1996).
[110]. P. Wang, F. Casadei, S. Shan, J.C. Weaver, and K. Bertoldi, Harnessing buckling to design tunable locally resonant acoustic metamaterials, *Physical review letters* **113**, 014301 (2014).
[111]. C. Ortiz and M.C. Boyce, Bioinspired structural materials, *Science* **319**, 1053 (2008).
[112]. H. Qi, B. Bruet, J. Palmer, C. Ortiz, and M. Boyce, *Micromechanics and macromechanics of the tensile deformation of nacre*, Springer, 2006.
[113]. P. Fratzl and R. Weinkamer, Nature's hierarchical materials, *Progress in Materials Science* **52**, 1263 (2007).
[114]. S. Castineira-Ibánez, V. Romero-García, J. Sánchez-Pérez, and L. Garcia-Raffi, Overlapping of acoustic bandgaps using fractal geometries, *EPL (Europhysics Letters)* **92**, 24007 (2010).
[115]. K. Bertoldi and M. Boyce, Mechanically triggered transformations of phononic band gaps in periodic elastomeric structures, *Physical Review B* **77**, 052105 (2008).
[116]. B. Davies, A. King, P. Newman, A. Minett, C.R. Dunstan, and H. Zreiqat, Hypothesis: Bones toughness arises from the suppression of elastic waves, *Scientific reports* **4**, (2014).
[117]. R.M. Erb, J.S. Sander, R. Grisch, and A.R. Studart, Self-shaping composites with programmable bioinspired microstructures, *Nature communications* **4**, 1712 (2013).
[118]. R. Libanori, R.M. Erb, A. Reiser, H. Le Ferrand, M.J. Süess, R. Spolenak, and A.R. Studart, Stretchable heterogeneous composites with extreme mechanical gradients, *Nature communications* **3**, 1265 (2012).
[119]. Y. Chen and L. Wang, Multiband wave filtering and waveguiding in bio-inspired hierarchical composites, *Extreme Mechanics Letters* **5**, 18 (2015).
[120]. C.J. Rupp, A. Evgrafov, K. Maute, and M.L. Dunn, Design of phononic materials/structures for surface wave devices using topology optimization, *Structural and Multidisciplinary Optimization* **34**, 111 (2007).

[121]. O. Sigmund and J.S. Jensen, Systematic design of phononic band–gap materials and structures by topology optimization, *Philosophical Transactions of the Royal Society of London A: Mathematical, Physical and Engineering Sciences* **361**, 1001 (2003).
[122]. Q. Chen and N.M. Pugno, In-plane elastic buckling of hierarchical honeycomb materials, *J. Mec. Theor. Appl.* **34**, 120 (2012).
[123]. F. CÃ, B. Russell, V. Deshpande, and N. Fleck, The through-thickness compressive strength of a composite sandwich panel with a hierarchical square honeycomb sandwich core, *J. Appl. Mech.* **76**, 061004 (2009).
[124]. A. Ajdari, B.H. Jahromi, J. Papadopoulos, H. Nayeb-Hashemi, and A. Vaziri, Hierarchical honeycombs with tailorable properties, *Int. J. Solids. Struct.* **49**, 1413 (2012).
[125]. Y. Sun and N.M. Pugno, In plane stiffness of multifunctional hierarchical honeycombs with negative Poisson's ratio sub-structures, *Compos. Struct.* **106**, 681 (2013).
[126]. L. Zhao, Q. Zheng, H. Fan, and F. Jin, Hierarchical composite honeycombs, *Mater. Design.* **40**, 124 (2012).
[127]. C. Taylor, C. Smith, W. Miller, and K. Evans, The effects of hierarchy on the in-plane elastic properties of honeycombs, *Int. J. Solids. Struct.* **48**, 1330 (2011).
[128]. L. Wang, M.C. Boyce, C.Y. Wen, and E.L. Thomas, Plastic Dissipation Mechanisms in Periodic Microframe-Structured Polymers, *Advanced Functional Materials* **19**, 1343 (2009).
[129]. M. Danielsson, D. Parks, and M. Boyce, Three-dimensional micromechanical modeling of voided polymeric materials, *Journal of the Mechanics and Physics of Solids* **50**, 351 (2002).
[130]. M. Danielsson, D.M. Parks, and M.C. Boyce, Micromechanics, macromechanics and constitutive modeling of the elasto-viscoplastic deformation of rubber-toughened glassy polymers, *Journal of the Mechanics and Physics of Solids* **55**, 533 (2007).
[131]. M.I. Hussein and M.J. Frazier, Band structure of phononic crystals with general damping, *Journal of Applied Physics* **108**, 093506 (2010).
[132]. S. Shan, S.H. Kang, P. Wang, C. Qu, S. Shian, E.R. Chen, and K. Bertoldi, Harnessing multiple folding mechanisms in soft periodic structures for tunable control of elastic waves, *Advanced Functional Materials* **24**, 4935 (2014).
[133]. A.S. Phani, J. Woodhouse, and N. Fleck, Wave propagation in two-dimensional periodic lattices, *The Journal of the Acoustical Society of America* **119**, 1995 (2006).
[134]. P. Wang, F. Casadei, S.H. Kang, and K. Bertoldi, Locally resonant band gaps in periodic beam lattices by tuning connectivity, *Physical Review B* **91**, 020103 (2015).
[135]. D. Mousanezhad, S. Babaee, R. Ghosh, E. Mahdi, K. Bertoldi, and A. Vaziri, Honeycomb phononic crystals with self-similar hierarchy, *Physical Review B* **92**, 104304 (2015).
[136]. L.J. Gibson and M.F. Ashby, *Cellular solids: structure and properties*, Cambridge university press, 1999.
[137]. H. Tao, L.R. Chieffo, M.A. Brenckle, S.M. Siebert, M. Liu, A.C. Strikwerda, K. Fan, D.L. Kaplan, X. Zhang, and R.D. Averitt, Metamaterials on paper as a sensing platform, *Advanced Materials* **23**, 3197 (2011).
[138]. T. Bückmann, N. Stenger, M. Kadic, J. Kaschke, A. Frölich, T. Kennerknecht, C. Eberl, M. Thiel, and M. Wegener, Tailored 3D mechanical metamaterials made by dip-in direct-laser-writing optical lithography, *Advanced Materials* **24**, 2710 (2012).
[139]. J.H. Lee, J.P. Singer, and E.L. Thomas, Micro-/Nanostructured Mechanical Metamaterials, *Advanced materials* **24**, 4782 (2012).

[140]. Y. Li, S. Luo, M.C. Yang, R. Liang, and C. Zeng, Poisson Ratio and Piezoresistive Sensing: A New Route to High-Performance 3D Flexible and Stretchable Sensors of Multimodal Sensing Capability, *Advanced Functional Materials* **26**, 2900 (2016).
[141]. Q. Zhang, X. Xu, D. Lin, W. Chen, G. Xiong, Y. Yu, T.S. Fisher, and H. Li, Hyperbolically Patterned 3D Graphene Metamaterial with Negative Poisson's Ratio and Superelasticity, *Advanced Materials* **28**, 2229 (2016).
[142]. D.R. Smith, J.B. Pendry, and M.C. Wiltshire, Metamaterials and negative refractive index, *Science* **305**, 788 (2004).
[143]. D.R. Smith and N. Kroll, Negative refractive index in left-handed materials, *Physical Review Letters* **85**, 2933 (2000).
[144]. J. Valentine, S. Zhang, T. Zentgraf, E. Ulin-Avila, D.A. Genov, G. Bartal, and X. Zhang, Three-dimensional optical metamaterial with a negative refractive index, *nature* **455**, 376 (2008).
[145]. Z. Yang, H. Dai, N. Chan, G. Ma, and P. Sheng, Acoustic metamaterial panels for sound attenuation in the 50–1000 Hz regime, *Applied Physics Letters* **96**, 041906 (2010).
[146]. M. Kadic, T. Bückmann, N. Stenger, M. Thiel, and M. Wegener, On the practicability of pentamode mechanical metamaterials, *Applied Physics Letters* **100**, 191901 (2012).
[147]. B. Florijn, C. Coulais, and M. van Hecke, Programmable mechanical metamaterials, *Physical review letters* **113**, 175503 (2014).
[148]. X. Zheng, H. Lee, T.H. Weisgraber, M. Shusteff, J. DeOtte, E.B. Duoss, J.D. Kuntz, M.M. Biener, Q. Ge, and J.A. Jackson, Ultralight, ultrastiff mechanical metamaterials, *Science* **344**, 1373 (2014).
[149]. X. Li and H. Gao, Mechanical metamaterials: Smaller and stronger, *Nature materials* **15**, 373 (2016).
[150]. G. Wu, Y. Cho, I.S. Choi, D. Ge, J. Li, H.N. Han, T. Lubensky, and S. Yang, Directing the deformation paths of soft metamaterials with prescribed asymmetric units, *Advanced Materials* **27**, 2747 (2015).
[151]. S.H. Kang, S. Shan, W.L. Noorduin, M. Khan, J. Aizenberg, and K. Bertoldi, Buckling-Induced Reversible Symmetry Breaking and Amplification of Chirality Using Supported Cellular Structures, *Advanced Materials* **25**, 3380 (2013).
[152]. H. Yasuda and J. Yang, Reentrant Origami-Based Metamaterials with Negative Poisson's Ratio and Bistability, *Physical review letters* **114**, 185502 (2015).
[153]. J.N. Grima, R. Caruana-Gauci, M.R. Dudek, K.W. Wojciechowski, and R. Gatt, Smart metamaterials with tunable auxetic and other properties, *Smart Materials and Structures* **22**, 084016 (2013).
[154]. K. Bertoldi, P.M. Reis, S. Willshaw, and T. Mullin, Negative Poisson's ratio behavior induced by an elastic instability, *Advanced Materials* **22**, 361 (2010).
[155]. X. Ren, J. Shen, A. Ghaedizadeh, H. Tian, and Y.M. Xie, A simple auxetic tubular structure with tuneable mechanical properties, *Smart Materials and Structures* **25**, 065012 (2016).
[156]. A. Ghaedizadeh, J. Shen, X. Ren, and Y.M. Xie, Tuning the performance of metallic auxetic metamaterials by using buckling and plasticity, *Materials* **9**, 54 (2016).
[157]. D.J. Rayneau-Kirkhope and M.A. Dias, Recipes for selecting failure modes in 2-d lattices, *Extreme Mechanics Letters* (2016).
[158]. K.E. Evans and A. Alderson, Auxetic materials: functional materials and structures from lateral thinking!, *Advanced materials* **12**, 617 (2000).

[159]. W. Yang, Z.-M. Li, W. Shi, B.-H. Xie, and M.-B. Yang, Review on auxetic materials, *Journal of materials science* **39**, 3269 (2004).
[160]. J. Grima, A. Alderson, and K. Evans, Auxetic behaviour from rotating rigid units, *Physica status solidi (b)* **242**, 561 (2005).
[161]. R. Lakes, Foam structures with a negative Poisson's ratio, *Science* **235**, 1038 (1987).
[162]. R. Lakes, Advances in negative Poisson's ratio materials, *Advanced Materials* **5**, 293 (1993).
[163]. Y. Tang, G. Lin, L. Han, S. Qiu, S. Yang, and J. Yin, Design of hierarchically cut hinges for highly stretchable and reconfigurable metamaterials with enhanced strength, *Advanced Materials* **27**, 7181 (2015).
[164]. D.Y. Fozdar, P. Soman, J.W. Lee, L.H. Han, and S. Chen, Three-Dimensional Polymer Constructs Exhibiting a Tunable Negative Poisson's Ratio, *Advanced functional materials* **21**, 2712 (2011).
[165]. J.N. Grima, L. Mizzi, K.M. Azzopardi, and R. Gatt, Auxetic perforated mechanical metamaterials with randomly oriented cuts, *Advanced Materials* **28**, 385 (2016).
[166]. H. Mitschke, J. Schwerdtfeger, F. Schury, M. Stingl, C. Körner, R.F. Singer, V. Robins, K. Mecke, and G.E. Schröder-Turk, Finding auxetic frameworks in periodic tessellations, *Advanced Materials* **23**, 2669 (2011).
[167]. R.H. Baughman, J.M. Shacklette, A.A. Zakhidov, and S. Stafström, Negative Poisson's ratios as a common feature of cubic metals, *Nature* **392**, 362 (1998).
[168]. J. Grima, R. Jackson, A. Alderson, and K. Evans, Do zeolites have negative Poisson's ratios?, *Advanced Materials* **12**, 1912 (2000).
[169]. J.N. Grima, R. Gatt, V. Zammit, J.J. Williams, K.E. Evans, A. Alderson, and R.I. Walton, Natrolite: A zeolite with negative Poisson's ratios, *Journal of Applied Physics* **101**, 086102 (2007).
[170]. F. Song, J. Zhou, X. Xu, Y. Xu, and Y. Bai, Effect of a negative Poisson ratio in the tension of ceramics, *Physical review letters* **100**, 245502 (2008).
[171]. A. Yeganeh-Haeri, D.J. Weidner, and J.B. Parise, Elasticity of a-cristobalite: a silicon dioxide with a negative Poisson's ratio, *Science* **257**, 650 (1992).
[172]. J.-W. Jiang and H.S. Park, Negative Poisson's Ratio in Single-Layer Graphene Ribbons, *Nano letters* **16**, 2657 (2016).
[173]. J.N. Grima, S. Winczewski, L. Mizzi, M.C. Grech, R. Cauchi, R. Gatt, D. Attard, K.W. Wojciechowski, and J. Rybicki, Tailoring graphene to achieve negative Poisson's ratio properties, *Advanced Materials* **27**, 1455 (2015).
[174]. Y. Suzuki, G. Cardone, D. Restrepo, P.D. Zavattieri, T.S. Baker, and F.A. Tezcan, Self-assembly of coherently dynamic, auxetic, two-dimensional protein crystals, *Nature* **533**, 369 (2016).
[175]. A. Slann, W. White, F. Scarpa, K. Boba, and I. Farrow, Cellular plates with auxetic rectangular perforations, *physica status solidi (b)* **252**, 1533 (2015).
[176]. F. Javid, E. Smith-Roberge, M.C. Innes, A. Shanian, J.C. Weaver, and K. Bertoldi, Dimpled elastic sheets: a new class of non-porous negative Poisson's ratio materials, *Scientific reports* **5**, (2015).
[177]. C. Lv, D. Krishnaraju, G. Konjevod, H. Yu, and H. Jiang, Origami based mechanical metamaterials, *Scientific reports* **4**, (2014).

[178]. Y. Hou, R. Neville, F. Scarpa, C. Remillat, B. Gu, and M. Ruzzene, Graded conventional-auxetic Kirigami sandwich structures: Flatwise compression and edgewise loading, *Composites Part B: Engineering* **59**, 33 (2014).
[179]. Y. Cho, J.-H. Shin, A. Costa, T.A. Kim, V. Kunin, J. Li, S.Y. Lee, S. Yang, H.N. Han, and I.-S. Choi, Engineering the shape and structure of materials by fractal cut, *Proceedings of the National Academy of Sciences* **111**, 17390 (2014).
[180]. D. Prall and R. Lakes, Properties of a chiral honeycomb with a Poisson's ratio of—1, *International Journal of Mechanical Sciences* **39**, 305 (1997).
[181]. M. Bianchi, F. Scarpa, M. Banse, and C. Smith, Novel generation of auxetic open cell foams for curved and arbitrary shapes, *Acta Materialia* **59**, 686 (2011).
[182]. L. Yang, D. Cormier, H. West, O. Harrysson, and K. Knowlson, Non-stochastic Ti–6Al–4V foam structures with negative Poisson's ratio, *Materials Science and Engineering: A* **558**, 579 (2012).
[183]. D. Li, L. Dong, and R.S. Lakes, The properties of copper foams with negative Poisson's ratio via resonant ultrasound spectroscopy, *physica status solidi (b)* **250**, 1983 (2013).
[184]. Y. Li, S. Luo, M.C. Yang, R. Liang, and C. Zeng, Poisson Ratio and Piezoresistive Sensing: A New Route to High-Performance 3D Flexible and Stretchable Sensors of Multimodal Sensing Capability, *Adv. Funct. Mater.* (2016).
[185]. T. Widlund, S. Yang, Y.-Y. Hsu, and N. Lu, Stretchability and compliance of freestanding serpentine-shaped ribbons, *International Journal of Solids and Structures* **51**, 4026 (2014).
[186]. Q. Ma, H. Cheng, K.-I. Jang, H. Luan, K.-C. Hwang, J.A. Rogers, Y. Huang, and Y. Zhang, A nonlinear mechanics model of bio-inspired hierarchical lattice materials consisting of horseshoe microstructures, *Journal of the Mechanics and Physics of Solids* **90**, 179 (2016).
[187]. K.-I. Jang, H.U. Chung, S. Xu, C.H. Lee, H. Luan, J. Jeong, H. Cheng, G.-T. Kim, S.Y. Han, and J.W. Lee, Soft network composite materials with deterministic and bio-inspired designs, *Nature communications* **6**, (2015).
[188]. K.-I. Jang, S.Y. Han, S. Xu, K.E. Mathewson, Y. Zhang, J.-W. Jeong, G.-T. Kim, R.C. Webb, J.W. Lee, and T.J. Dawidczyk, Rugged and breathable forms of stretchable electronics with adherent composite substrates for transcutaneous monitoring, *Nature communications* **5**, (2014).
[189]. K. Boba, M. Bianchi, G. McCombe, R. Gatt, A.C. Griffin, R.M. Richardson, F. Scarpa, I. Hamerton, and J.N. Grima, Blocked shape memory effect in negative Poisson's ratio polymer metamaterials, *ACS Applied Materials & Interfaces* (2016).
[190]. A.S. Dalaq, D.W. Abueidda, and R.K.A. Al-Rub, Mechanical properties of 3D printed interpenetrating phase composites with novel architectured 3D solid-sheet reinforcements, *Composites Part A: Applied Science and Manufacturing* **84**, 266 (2016).
[191]. P. Zhang and A.C. To, Transversely isotropic hyperelastic-viscoplastic model for glassy polymers with application to additive manufactured photopolymers, *Int. J. Plasticity.* **80**, 56 (2016).
[192]. C. Thurnherr, L. Ruppen, G. Kress, and P. Ermanni, Non-linear stiffness response of corrugated laminates in tensile loading, *Compos. Struct.* **157**, 244 (2016).
[193]. T.F. Smith and M.S. Waterman, Identification of common molecular subsequences, *J. Mol. Biol.* **147**, 195 (1981).
[194]. G. Trainiti, J. Rimoli, and M. Ruzzene, Wave propagation in periodically undulated beams and plates, *Int. J. Solids. Struct.* **75**, 260 (2015).

[195]. S. Rudykh and M.C. Boyce, Transforming Wave Propagation in Layered Media via Instability-Induced Interfacial Wrinkling, *Physical Review Letters* **112**, (2014).
[196]. P. Wang, F. Casadei, S.C. Shan, J.C. Weaver, and K. Bertoldi, Harnessing Buckling to Design Tunable Locally Resonant Acoustic Metamaterials, *Physical Review Letters* **113**, (2014).
[197]. N. Ohno, D. Okumura, and T. Niikawa, Long-wave buckling of elastic square honeycombs subject to in-plane biaxial compression, *International Journal of Mechanical Sciences* **46**, 1697 (2004).
[198]. B. Haghpanah, J. Papadopoulos, D. Mousanezhad, H. Nayeb-Hashemi, and A. Vaziri, Buckling of regular, chiral and hierarchical honeycombs under a general macroscopic stress state, *Proceedings of the Royal Society a-Mathematical Physical and Engineering Sciences* **470**, (2014).
[199]. A. Khelif, B. Aoubiza, S. Mohammadi, A. Adibi, and V. Laude, Complete band gaps in two-dimensional phononic crystal slabs, *Physical Review E* **74**, (2006).
[200]. Y.Y. Chen and L.F. Wang, Periodic co-continuous acoustic metamaterials with overlapping locally resonant and Bragg band gaps, *Applied Physics Letters* **105**, (2014).
[201]. Y. Achaoui, A. Khelif, S. Benchabane, L. Robert, and V. Laude, Experimental observation of locally-resonant and Bragg band gaps for surface guided waves in a phononic crystal of pillars, *Physical Review B* **83**, (2011).
[202]. Z.Y. Liu, C.T. Chan, P. Sheng, A.L. Goertzen, and J.H. Page, Elastic wave scattering by periodic structures of spherical objects: Theory and experiment, *Physical Review B* **62**, 2446 (2000).
[203]. A. Khelif, Y. Achaoui, S. Benchabane, V. Laude, and B. Aoubiza, Locally resonant surface acoustic wave band gaps in a two-dimensional phononic crystal of pillars on a surface, *Physical Review B* **81**, (2010).
[204]. G. Wang, D.L. Yu, J.H. Wen, Y.Z. Liu, and X.S. Wen, One-dimensional phononic crystals with locally resonant structures, *Physics Letters A* **327**, 512 (2004).
[205]. Y. Chen, T. Li, F. Scarpa, and L. Wang, Lattice Metamaterials with Mechanically Tunable Poisson's Ratio for Vibration Control, *Physical Review Applied* **7**, 024012 (2017).
[206]. G. Trainiti, J.J. Rimoli, and M. Ruzzene, Wave propagation in periodically undulated beams and plates, *International Journal of Solids and Structures* **75-76**, 260 (2015).
[207]. P. Zhang, M.A. Heyne, and A.C. To, Biomimetic staggered composites with highly enhanced energy dissipation: Modeling, 3D printing, and testing, *Journal of the Mechanics and Physics of Solids* **83**, 285 (2015).
[208]. L. Gibson and M. Ashby (1997) Cellular solids: structure and properties. (Cambridge University Press).